Imperial College London

Mechanisms of low-frequency variability in an eddy-resolving midlatitude coupled ocean-atmosphere model

Ryosuke Kurashina

Department of Mathematics, Imperial College London

Submitted in part fulfilment of the requirements for the degree of
Doctor of Philosophy in Mathematics at Imperial College London

Declarations

Statement of originality

I declare that this thesis has been composed solely by myself and that it has not been submitted, in whole or in part, in any previous application for a degree. Except where states otherwise by reference or acknowledgement, the work presented is entirely my own.

Copyright declaration

Acknowledgements

I am grateful to my supervisors Pavel Berloff and Igor Shevchenko, for providing their expertise and knowledge on what is (very clearly!) a challenging field of research. I doubt I would have gotten this far without their help and advice. A special thank you to Pavel for our many weekly meetings and his infectious enthusiasm, which has instilled in me a deep appreciation of science, oceanography and the climate.

I would also like to thank the MPE CDT staff, especially Barsha, Sam, Janet and Colin, for solving many of my administration issues and making the cogs of the CDT turn so smoothly. I also send my best wishes to my fellow MPE students- who I am sure have very bright and successful futures ahead of them!

Finally, I would like to thank my family, friends, and partner Anisha for being there during the difficult times and brightening those dark days during the pandemic.

Glossary

- AST: Atmospheric surface temperature
- CMIP: Coupled Model Intercomparison Project
- EOF: Empirical orthogonal function
- GCM: General circulation model
- PV: Potential vorticity
- QG: Quasigeostrophic
- SST: Sea surface temperature
- SVD: Singular value decomposition
- VSL: Viscous sublayer
- WBC: Western boundary current
- WBL: Western boundary layer

Turning and turning in the widening gyre

The falcon cannot hear the falconer;

Things fall apart; the centre cannot hold;

Mere anarchy is loosed upon the world.

W.B. Yeats, 'The Second Coming'

Abstract

The role of the wind-driven ocean gyres in the midlatitude climate variability is investigated using an idealised, eddy-resolving, quasigeostrophic, coupled model. The model consists of a double gyre box ocean and a periodic channel atmosphere which are coupled together by mixed layers that allow for transfers of heat and momentum. The entire model is driven by fixed, latitudinally-varying solar radiation that is redistributed by a linearised radiation scheme. Our findings reveal a coupled interaction that involves a positive feedback between meridional shifts of the ocean eastward jet extension and downstream displacements of the atmospheric westerly jet. The displacement of the atmospheric jet is resolution-dependent and caused by shifts in the latitudinal centre of low-level baroclinicity, while meridional shifts of the ocean eastward jet are likely controlled by the propagation of baroclinic Rossby waves that form in the eastern basin. Effects of mesoscale turbulence and intrinsic variability of the ocean jet disrupts the arrival of Rossby waves at the western boundary and thus reduces its predictability. In addition, the ocean gyre response is shown to be dependent on forcing location, and a dynamically-distinct, inertial recirculation zone response is found for western basin wind-curl anomalies.

Other relevant nonlinear dynamics that maintain the wind-driven ocean gyre circulation are investigated using an adiabatic, fixed-wind, double gyre box ocean model. It is revealed that nonlinear restructuring of the western boundary layer inhibits viscous relative vorticity fluxes, creating an accumulation of enstrophy in the gyres. This enstrophy is advected downstream into the inertial recirculation zones which in turn supports the eastward jet. The growing imbalance in enstrophy is then eventually rectified by inter-gyre potential vorticity fluxes.

Contents

List of Tables

List of Figures

Chapter 1

Introduction

1.1 Motivation

Since Bjerknes (1964) first proposed the role of the ocean circulation in the global meridional heat transport, there has been significant progress in the field to quantify and discern its impact on the Earth's climate. For example, western boundary currents (WBCs), such as the Kuroshio in the North Pacific and Gulf Stream in the North Atlantic, are fast, narrow currents that reside on the western boundary of every major ocean basin[1]. These currents, and their associated eastward jet extension and inertial recirculation zones, are responsible for the poleward transport of warm waters from the tropics, into the midlatitudes, and beyond. Furthermore, the wind-driven ocean gyres, which contain the WBCs, eastward jet and inertial recirculations, show vigorous mesoscale activity through the shedding of coherent eddies by baroclinic instabilities which occur due to sloping of isopycnals. These eddies are crucial in not only mixing and stirring processes but also in shaping the mean circulation itself through intricate eddy dynamics.

In addition, it has now been shown that the wind-driven ocean gyre circulation plays a vital role in the encapsulating midlatitude climate. Persistent wintertime sea surface temperature (SST) anomalies lead to the release of large quantities of heat into the atmosphere through sensible and latent heat

[1] Other examples include the Brazil Current in the South Atlantic, East Australian Current in the South Pacific and the Agulhas Current in the Indian Ocean.

fluxes. This heat flux is particularly prevalent over the WBCs and eastward jet where SST gradients lead to the formation of a 'front'. Storm tracks, which are regions of the atmosphere that show high baroclinic eddy activity and storm formation, are strongly anchored to these SST fronts due to their ability to restore the low-level baroclinicity in the atmosphere. Furthermore, since ocean eastward jet extensions show high variability extending from interannual through to decadal time-scales, this provides a dynamical pathway for the ocean gyres to couple with the overlying atmospheric circulation.

The added recent issues regarding climate change make the study of such climate phenomena relevant as the oceans are warming at a rapid rate due to the anthropogenic emission of greenhouse gases, with the midlatitudes expected to undergo significant changes in the coming decades (Collins et al., 2013). Hence, understanding the anatomy and mechanisms that control key aspects of the natural midlatitude climate variability is a topic of increasing importance and urgency.

Before we move onto the main body of the thesis, we give a background of the main topics covered in this thesis.

1.2 Background

The development of skillful long-range forecasts at midlatitudes, spanning from seasonal to decadal time-scales, would lead to massive benefits for society. These include: improved risk management through better prediction of the frequency and intensity of wintertime storms (Renggli et al., 2011), reduced disruption in transport networks (Palin et al., 2013) and increased productivity of marine fisheries (Tommasi et al., 2017). However, coupled general circulation models (GCMs) consistently exhibit reduced predictability of themselves than they do of nature (e.g. Scaife et al., 2014; Dunstone et al., 2016; Baker et al., 2018; Smith et al., 2019, 2020). This is known as the signal-to-noise paradox and is problematic for long-range forecasting models as it increases the number of ensemble members required to make skillful predictions by roughly an order of magnitude (Smith et al., 2020). This has been suggested to be the result of deficiencies observed in current modelling of the climate such as, amongst others, decreased persistence (Zhang and Kirtman, 2019; Strommen and Palmer, 2019), weak midlatitude air-sea coupling (Scaife and Smith, 2018; Kim et al., 2018) and low atmospheric

resolution (Scaife et al., 2019).

Resolving ocean mesoscales in coupled GCMs has been shown to lead to significant regional differences in precipitation and improvements in forecast skill over eddy-rich regions such as WBCs and the Southern Ocean (He et al., 2018; Infanti and Kirtman, 2019). The decadal predictability of these regions is generally underestimated and is, in part, due to unresolved ocean mesoscales in operational coupled climate models (Zhang et al., 2021). For example, the model resolutions from the latest Coupled Model Intercomparison Project (CMIP) are typically 250 km in the atmosphere and 100 km in the ocean[2]. However, ocean resolutions of 10 km and finer are required for the model to be deemed 'eddy-resolving' and capture the bulk of the kinetic energy spectrum that peaks at the mesoscales (Smith et al., 2000). Multidecadal runs of coupled climate models with an eddy-resolving ocean component have been demonstrated to have warmer global SSTs, increased interannual SST variability at midlatitudes, and consequent increases in air-sea feedbacks compared to a model with a non-eddy-resolving ocean component (Kirtman et al., 2012). Furthermore, Kirtman et al. (2017) found resolving ocean mesoscale activity increases the model predictability of convective rainfall and upper-troposphere circulation. The direct role of mesoscale SST variability has also been shown to influence midlatitude cyclogenesis far away from its point of origin (Ma et al., 2015). However, it is unlikely that resolving ocean mesoscales alone will untangle the problems encountered with the current generation of coupled GCMs. For example, it has been shown that an atmospheric GCM, forced by observed SST anomalies, still exhibits the same problems observed in coupled GCMs (Simpson et al., 2018).

Recent research suggests that models that resolve the atmospheric mesoscale, on the order of $10-100$ km, may also be required, rather than just resolving the Rossby deformation scales which are on the order of 1000 km. It is postulated that as the atmospheric mesoscales are resolved, oceanic forcing of the upper-troposphere will be enhanced (Czaja et al., 2019). Benefits of this include: better representation of midlatitude storms (Jung et al., 2012), improvements in prediction of blocking frequencies (Jung et al., 2012; Schiemann et al., 2017), revealing of the non-Gaussian persistence of important weather regimes and improvements in the simulated ocean eastward jet extension (Ma et al., 2016) and storm track (Ma et al., 2017; Foussard et al., 2019; Zhang et al., 2020). Furthermore,

[2]Note higher resolutions are available under the HighResMIP protocol (Eyring et al., 2016)

resolving atmospheric mesoscales leads to capturing of mesoscale SST perturbations (Sheldon et al., 2017) and the transition of kinetic energy spectra from k^{-3} to $k^{-5/3}$ spectral ranges. Although we must note that the 'effective resolution' of these models, which is the length-scale at which energy is dissipated, is typically much larger than the model resolution (Skamarock, 2004; Skamarock et al., 2014; Klaver et al., 2020). This is due to energy contributions at the grid-scale from the model's implemented dissipation parametrisation. Problematically, the effective model resolution has been shown to scale poorly with model resolution (Klaver et al., 2020).

As atmospheric mesoscales are better resolved, eddy dynamics has been shown to become more prevalent in certain studies. For example, Famooss Paolini et al. (2022) showed that increases in atmospheric resolution lead to a westerly jet response to SST anomalies that is more similar to reanalysis data. This improved response of the downstream westerly jet was to move in the same direction as the SST front displacement. Such a change in circulation is opposite to what is expected from the linear theory (Hoskins and Karoly, 1981), implying that the anomalous diabatic heating associated with the SST front shift is mainly balanced by transient eddy forcing (Peng et al., 1997; Peng and Whitaker, 1999; Smirnov et al., 2015). Atmospheric GCMs run under more realistic SST forcing show larger and more persistent poleward jet shifts during high eddy heat flux transients (Piazza et al., 2016; O'Reilly et al., 2017). Transient eddy heat fluxes in the atmospheric mixed layer also show significant differences when run under more realistic SST forcings (Small et al., 2014). We note here that despite recent improvements in atmospheric GCM resolution, eddy-mean flow feedbacks still show complicated, nonlinear responses to SST anomalies (Seo et al., 2017). Indeed, it still remains unclear whether atmospheric responses to SST anomalies in nature show a stronger dependence on eddy-mean flow feedbacks, or other processes, such as eddy dynamics, that are not well captured by atmospheric GCMs. For example, increasing the atmospheric resolution has been shown to change the time-averaged zonal winds, with larger increases in resolution leading to larger changes in zonal winds. Paradoxically, this does not always translate to changes that are closer to observations (Czaja et al., 2019), indicating that increasing resolution alone is sometimes insufficient and new or improved model parametrisations may also need to be developed.

In the past, attributing drivers of the midlatitude coupled climate variability has proven to be complex in nature with much of the early literature in disagreement about the role played by the midlatitude

ocean circulation, even among those using the same or similar models (see Latif and Barnett, 1994, 1996; Schneider et al., 2002, for the classic example). It is argued that most of the midlatitude oceans act as a 'white-noise integrator' of high-frequency atmospheric forcing through a first-order Markov process (Hasselmann, 1976; Frankignoul and Hasselmann, 1977). Low-frequency SST anomalies damp surface heat fluxes which consequently increase the surface temperature variability of the ocean and atmosphere (Battisti et al., 1995; Barsugli and Battisti, 1998; Saravanan and McWilliams, 1997; Kushnir et al., 2002). For example, the basin-scale tripole SST anomalies observed in the North Atlantic and Pacific are partly attributed to this process (Mantua et al., 1997; Okumura et al., 2001; Alexander et al., 2010; Schneider and Fan, 2012). Indeed, earlier review studies of the midlatitude coupled climate variability did not find evidence for a strong response of the extratropical atmosphere to large-scale SST anomalies (e.g. Kushnir et al., 2002; Kwon et al., 2010). In these studies, it was proposed that SST variability is excited by basin-scale modes of atmospheric variability which then weakly feed back on the atmosphere[3]. In Kushnir et al. (2002), a 'weak' or 'strong' SST feedback is defined as an upper-tropospheric geopotential height disturbance to a typical SST anomaly that is less than or greater than typical disturbances due to internal dynamics at some time-scale, respectively. For example, the value quoted for this threshold in Kushnir et al. (2002) is $50-100\,\mathrm{m}$ at $500\,\mathrm{hPa}$ for monthly to interannual time-scales.

In recent times it has become more clear that the white-noise integrator hypothesis is insufficient in explaining climate variability over regions of the ocean such as the WBCs and their eastward jet extensions (Smirnov et al., 2014). For starters, these regions of the ocean show persistent winter-time SST anomalies which increase surface heat flux variability and drive shifts in the overlying jet stream and storm track (Tanimoto, 2003; Feliks et al., 2004; Taguchi et al., 2012). Most importantly, recent reanalysis data shows the influence of SST variability on the atmosphere is now significantly stronger than previous estimates and on the scale which would class as a 'strong' SST feedback (Frankignoul et al., 2011; Taguchi et al., 2012; Révelard et al., 2018). The variability of WBCs and eastward jet extensions have been suggested to be controlled by: 1) large-scale atmospheric forcings that trigger decadal responses in the ocean gyres, either through advective effects (Dewar, 2003) or westward-propagating baroclinic Rossby waves (Taguchi et al., 2007; Sasaki et al., 2013); 2) intrinsic

[3]The atmospheric GCMs used in these studies are now considered to be relatively low resolution compared to modern-day GCMs.

interannual variability due to chaotic, turbulent behaviour of eastward jet extensions (Nonaka et al., 2016). These changes in strength and position of eastward jet extensions then impact on local coupling with the overlying jet and storm track through shifts in the low-level baroclinicity (Nakamura et al., 2004; Brayshaw et al., 2008; Sampe et al., 2010; O'Reilly and Czaja, 2015). Eastward jet variability has also been shown to have an influence on downstream atmospheric blocking through SST-induced modifications in atmospheric eddy heat fluxes (O'Reilly and Czaja, 2015).

Within the context of climate change, the location of midlatitude jet streams and storm tracks is set to shift poleward (e.g. Barnes and Polvani, 2013; Yin, 2005), with different response time-scales of the atmospheric circulation controlled by the SST evolution (Ceppi et al., 2018). Most studies that have investigated the role of the midlatitude oceans only look at the atmospheric response to large-scale changes in the circulation such as the upwelling of cold waters in the Southern Ocean (Held and Hoskins, 1985; Marshall et al., 2014) and the weakening of the meridional heat transport in the North Atlantic (Woollings et al., 2012). Reconstructions of SST observations over the past century show a more rapid warming of WBCs compared to the global average (Wu et al., 2012; Yang et al., 2016). Warming and poleward shifts of the WBCs are associated with the shift and intensification of near-surface winds due to changes in the midlatitude jet stream, with the exception of the Gulf Stream which is expected to weaken with the Atlantic Meridional Overturning Circulation (AMOC) (Yang et al., 2016). Recent studies using high-resolution coupled GCMs speculate that significant differences in the SST response to climate change are expected in comparison to what is currently projected by CMIP models. These differences include faster warming of the North Atlantic Shelf (Saba et al., 2016) and midlatitude air-sea heat fluxes being predominantly driven by the intrinsic ocean variability, rather than the atmospheric variability (Small et al., 2019). However, more observational evidence is required to verify the claims made in these studies. It is still very uncertain to what extent SST responses to anthropogenic CO_2 emissions may affect, for example, the meridional temperature gradients in the upper-troposphere. Such investigations are important as meridional temperature gradients at both high and low levels in the atmosphere strongly influence future climate projections (Held and Hoskins, 1985; Shaw et al., 2016). Czaja et al. (2019) has postulated that this is possible by making comparisons between two separate, yet consistent, avenues of study which show reductions of SST biases in the North Atlantic may lead to increased influence of the Gulf Stream on

the upper-troposphere (e.g. Lee et al., 2018; Siqueira and Kirtman, 2016).

Although coupled GCMs are vital in studying observed climate phenomena and in the development of future forecasting and climate projection systems, they are computationally expensive to run and often difficult to analyse. On the other hand, idealised coupled models offer a computationally cheaper and more dynamically-transparent alternative with highly resolved dynamics. For example, Dewar (2001) showed that mesoscale eddies remained crucial in controlling the variability of inertial recirculation zones. This variability feeds back strongly on ocean Ekman pumping, peaking at decadal time-scales, and thus controls the SST response and atmospheric variability. This time-scale control of atmospheric variability has also been shown to be important by Hogg et al. (2006), with preferred decadal time-scales selected by nonlinear adjustment of the ocean gyres (Dewar, 2003). This has been shown to be able to consequently set the time-scale of decadal coupled oscillations through transitions between pairs of preferred atmospheric states (Kravtsov et al., 2007). For example, Kravtsov et al. (2007) found that as the westerly atmospheric jet switches from a poleward to equatorward state, nonlinear adjustments of the ocean eastward jet extension to anomalous forcing lead to a persistent SST anomaly forming. This SST anomaly anchors the atmosphere to remain in its equatorward latitude state through strong surface heat fluxes until the anomaly dissipates. After the SST anomaly dissipates, the atmosphere returns to its more preferred poleward state which also consequently forces the eastward jet back poleward. Suppressing ocean mesoscale eddies had a weakening effect on the coupled variability, further supporting the view that ocean mesoscale eddies are vital in not only in controlling ocean variability but also the overlying atmosphere. Indeed, to ensure the influences of ocean gyre dynamics on the midlatitude climate variability are modelled, it is necessary to either 'brute force' resolve the eddies or parameterise them in a dynamically consistent manner (Berloff et al., 2007a). Other mechanisms of coupling include a westward-propagating coupled Rossby wave which act on interannual time-scales associated with the wave's basin crossing time (Kravtsov et al., 2006; Farneti, 2007). This coupled interaction was shown to not require the atmosphere to transition between two preferred states (Kravtsov et al., 2006) and was akin to the positive feedback mechanism proposed by Goodman and Marshall (1999).

Within the framework of adiabatic, eddy-resolving, idealised ocean models driven by fixed winds, the role of mesoscale eddies in ocean gyre variability is well studied through detailed analyses of the

underlying potential vorticity (PV) dynamics (e.g. Berloff and McWilliams, 1999a; Hogg et al., 2005; Berloff et al., 2007a; Shevchenko et al., 2016). These models show intrinsic low-frequency behaviour at decadal time-scales such as meridional shifts, changes in axis tilt and strength of eastward jet extensions and inertial recirculation zones. Within the recirculation zones, processes controlled by mesoscale dynamics such as eddy backscatter and inter-gyre PV exchange occur. Eddy backscatter is a nonlinear, turbulent process that occurs largely in the inertial recirculation zones. Eddies are shed off due to jet instabilities, which then propagate westwards along the inertial recirculation zones. Up-gradient meridional eddy advection in these regions then re-sharpen PV gradients and consequently leads to fortification of the eastward jet extension (Berloff, 2005, e.g.). The competition between these two processes, with eddy backscatter fortifying the eastward jet (Berloff, 2005, 2016; Shevchenko and Berloff, 2016) and inter-gyre PV exchange weakening it (Berloff et al., 2007b), have been shown to be crucial in driving the decadal ocean gyre variability. These processes are usually triggered by anomalous wind-forcings that arise through mislalignments of the zero vorticity flux line and inter-gyre boundary (Berloff et al., 2007b), or through modes of large-scale atmospheric variability such as meridional shifts of atmospheric jets that lead to formations of the 'intergyre gyre' (Czaja and Marshall, 2001). Crucially, it is the strong advective effects within the inertial recirculation zones that are shown to be important in driving this decadal ocean gyre variability.

The PV that maintains the circulation in these inertial recirculation zones is fuelled by the upstream western boundary layer (WBL) (Cessi et al., 1987). Multiple studies have shown that the loss of relative vorticity within the viscous sublayer (VSL) of the WBCs is less than the planetary vorticity gained (Cessi et al., 1987; Lozier and Riser, 1989; Kiss, 2002, 2010; Ypma et al., 2016). This is due to the cutting down of high velocities in the VSL by nonlinear dynamics (Veronis, 1966a,b) which consequently leads to reductions in viscous boundary fluxes (Spall, 2014). This creates an accumulation of PV in the WBL and downstream inertial recirculations. Indeed, some of this PV drives eddy backscatter mechanism in the inertial recirculations (Berloff, 2005, 2016; Shevchenko and Berloff, 2016) but the rest must be removed through inter-gyre PV exchanges to satisfy PV conservation Kurashina et al. (2021). More recently, advection-induced circulation features known as counter-rotating gyre anomalies (CGAs) have been found, which consist of nonlinear circulation anomalies embedded in the WBL and ocean interior (Shevchenko and Berloff, 2016). These anomalies are of opposite sign in PV to

that of the gyre implying that they act to weaken the ocean gyre circulation. A key aforementioned mechanism in the ocean gyres that weakens the circulation is inter-gyre PV exchange across the jet. However, eddy backscatter is largely contained within the inertial recirculations, while the CGAs appear to be largely embedded within the ocean interior and WBL. A clear dynamical link between these two phenomena has yet to be made but has been hypothesised by Shevchenko and Berloff (2016).

Another proposed mechanism of decadal ocean gyre variability is through baroclinic Rossby wave adjustments (Sasaki and Schneider, 2011; Sasaki et al., 2013). This mechanism occurs due to the formation of a basin-scale, baroclinic Rossby wave in the eastern ocean basin. This Rossby wave then propagates westwards along the eastward jet, narrowing in meridional scale as it does so in order to conserve PV along the wave trajectory. Since the eastward jet extension is located along the region where PV changes in sign, this propagating PV anomaly then causes the meridional position of the jet to shift. For example, an anti-cyclonic wind-stress curl in the eastern North Pacific has been linked to a poleward meridional shift in the Kuroshio extension (Seager et al., 2001; Sasaki et al., 2013; Wills et al., 2019). A strengthening of the eastward jet extension was found to occur very shortly afterwards with an eastward propagating signal indicating the importance of advective effects by the WBCs. Such an acceleration of the eastward jet has been suggested to be triggered by the arrival of the Rossby wave signal near the jet separation region which leads to local restructuring of the WBL (Taguchi et al., 2005). In these studies, it is implied that advection effects are secondary to the Rossby wave propagation and that effects of advection may only be triggered by the arrival of the wave at the western boundary.

We take this moment now to highlight the difference between eastward jet reorganisations that occur due to Rossby wave arrival at ocean basin western boundaries (e.g. Taguchi et al., 2005, 2007) and an advective response of the inertial recirculation zones to anomalous wind-forcing (e.g. Dewar, 2003). Although these two mechanisms may have similar effects on the eastward jet and recirculation zones, one is dependent on propagating waves (e.g. Taguchi et al., 2005) while the other is governed by advective processes in the inertial recirculation zones where the response time-scale has been shown to be independent of parameters that affect wave propagation such as basin-scale width (Dewar, 2003).

There are many more specific examples of how the inertial recirculation zones respond to wind-

forcing asymmetries. For example, asymmetric wind-forcings have been shown to induce deviations from straight west-to-east ocean jets due to differences in strength between the inertial recirculation zones (Moro, 1988; Hogg et al., 2005). This is because the vorticity flux imbalance creates a stronger recirculation zone which leads the jet to 'wind-up' around itself (Moro, 1988). Other effects of asymmetric wind-forcing include WBC overshooting (Harrison and Stalos, 1982) and decreases in eastward jet penetration as wind-curl asymmetry is increased (Rhines and Schopp, 1991). Ekman pumping anomalies near the eastward jet separation region have also been shown to destabilise the jet and weaken the ocean gyre circulation (Hogg et al., 2009).

1.3 Objectives

There are, largely speaking, two main objectives of this thesis which will now be outlined. The first is in understanding the role of the wind-driven ocean gyre dynamics in the midlatitude climate variability. As outlined earlier, there still remains significant uncertainty on the gyres' role with their importance often underestimated until relatively recently. Our approach to this problem involves the use of an idealised, eddy-resolving, quasigeostrophic coupled model. These models are under-studied in comparison to those that involve the use of coupled GCMs, high-resolution satellite or reanalysis data. Hence, the use of such frameworks offers a wealth of potential to discover novel, modelled behaviours that are relevant to the natural midlatitude climate variability.

The second objective is in understanding the intricate and complex nonlinear dynamics that controls the wind-driven ocean circulation. This involves the modelling of the wind-driven circulation over long simulation periods using an idealised, adiabatic, eddy-resolving, quasigeostrophic, double gyre ocean model driven by fixed winds. These models offer similar benefits to the coupled model described above and remain a powerful tool in the investigation of the wind-driven ocean gyres.

1.4 Thesis structure

Our investigations into the wind-driven ocean gyre circulation and their role in the midlatitude climate will be studied in the following manner. Firstly, a description of the main models, methods and tools used in the thesis is given in Chapter 2. This is followed by an investigation into the anatomy and mechanisms of ocean gyre coupling with jet streams in Chapters 3 and 4. Other important mechanisms relating to intricate nonlinear dynamics in WBCs that control the ocean gyre circulation are studied in Chapter 5. Finally, a consolidation of the main findings and potential future works are given in Chapter 6.

Parts of this chapter have been taken from Kurashina et al. (2021); Kurashina and Berloff (2022a,b), all of which is original work that has been conducted by the author.

Chapter 2

Models, methods and tools

2.1 The Quasi-Geostrophic Coupled Model (Q-GCM)

The main model we will be using in this thesis is version 1.5.0 of the Quasi-Geostrophic Coupled Model (Q-GCM) which was described and implemented in Hogg et al. (2003). The documentation of this model is available to read in Hogg et al. (2014). The model is designed to mimic aspects of the midlatitude climate system and consists[1] of a wind-driven, double gyre box ocean coupled to a periodic, channel atmosphere through mixed layers that allow for transfers of heat and momentum. The model is similar to that used in Kravtsov and Robertson (2002) and Kravtsov et al. (2007) but also includes a dynamically-active atmospheric mixed layer.

Notation

Before we move onto describing the model, we will introduce the notation used in this paper which is identical to the one used in Hogg et al. (2003). Left-superscript, given by 'o' or 'a', indicates ocean or atmosphere variables and right-subscript, given by 'm' or integer i, indicates the mixed layer or i-th isopycnal layer, respectively. Layers are counted away from the ocean-atmosphere interface.

[1] The model also allows for many other configurations such as a periodic, channel ocean which may be used to mimic the Antarctic Circumpolar Current (ACC).

Model Geometry

The box ocean model consists of 3 isopycnal layers with depths ${}^oH_1 = 350\,\mathrm{m}, {}^oH_2 = 750\,\mathrm{m}$ and ${}^oH_3 = 2900\,\mathrm{m}$. The benchmark solution has a nominal ocean resolution of 5 km for a basin with lateral dimensions $4800\,\mathrm{km} \times 4800\,\mathrm{km}$. This gives a discretised grid of size 961×961 points representing cell vertices in the longitudinal and latitudinal directions, respectively. Within the upper-isopycnal ocean, there is a mixed layer of fixed depth ${}^oH_m = 100\,\mathrm{m}$. The channel atmosphere also consists of 3 isopycnal layers with depths ${}^aH_1 = 2000\,\mathrm{m}, {}^aH_2 = 3000\,\mathrm{m}$ and ${}^aH_3 = 4000\,\mathrm{m}$. The benchmark solution has a nominal atmosphere resolution of 20 km for a channel with lateral dimensions $30\,720\,\mathrm{km} \times 7680\,\mathrm{km}$. This gives a discretised grid of size 1537×385 points representing cell vertices in the longitudinal and latitudinal directions, respectively. Within the lower-isopycnal atmosphere, there is also another mixed layer of variable depth with an unperturbed thickness of ${}^aH_m = 1000\,\mathrm{m}$.

The quasigeostrophic (QG) layers

The QG equations for the ocean and atmosphere may be written in terms of PV anomalies and dynamic pressure anomalies. For example in the ocean, they are denoted in vector form as ${}^o\mathbf{q} = ({}^oq_1, {}^oq_2, {}^oq_3)^T$ and ${}^o\mathbf{p} = ({}^op_1, {}^op_2, {}^op_3)^T$, respectively. Ocean PV anomalies are defined as

$$ {}^o\mathbf{q} = \frac{1}{f_0}\nabla^2 {}^o\mathbf{p} - f_0 A\, {}^o\mathbf{p} \tag{2.1} $$

where $f_0 = 9.37 \times 10^{-5}\ \mathrm{s}^{-1}$ is the Coriolis parameter and A is a matrix which defines interactions between layers through dynamic pressure anomalies or buoyancies

$$ A = \begin{bmatrix} \frac{1}{H_1 g_1'} & -\frac{1}{H_1 g_1'} & 0 \\ -\frac{1}{H_2 g_1'} & \frac{1}{H_2}\left(\frac{1}{g_2'} + \frac{1}{g_1'}\right) & -\frac{1}{H_2 g_2'} \\ 0 & -\frac{1}{H_3 g_2'} & \frac{1}{H_3 g_2'} \end{bmatrix} \tag{2.2} $$

with g_i' as the reduced gravities. In the ocean, $g_1' = 0.0222\,\mathrm{ms}^{-2}, g_2' = 0.0169\,\mathrm{ms}^{-2}$ which correspond to Rossby deformation radii of 40.0 km and 20.6 km, respectively. The definition of PV anomaly in the atmosphere is the same as the ocean apart from the addition of land orography which is given in

Subsubsection 2.1.

Full PV is obtained by adding the term $\beta y \cdot \mathbf{1}$ onto (2.1) where $\beta = 1.75 \times 10^{-11}$ m^{-1}s^{-1} is the planetary vorticity gradient and $\mathbf{1} = (1,1,1)^T$. We use (x,y) as our zonal and meridional coordinates where x is always measured increasing eastwards from the western boundary of the model domain; y is measured increasing polewards from the central latitude y_0.

Dynamic pressures in the i-th isopycnal ocean may be converted to the transport streamfunction through the relation

$$ {}^{o}\Psi_i = \frac{{}^{o}H_i}{f_0} {}^{o}p_i \tag{2.3} $$

Zonal and meridional velocities are computed through taking derivatives of ${}^{o}p_i$

$$ {}^{o}u_i = -\frac{\partial {}^{o}p_i}{\partial y}, \; {}^{o}v_i = \frac{\partial {}^{o}p_i}{\partial x} \tag{2.4} $$

Atmosphere velocities may be computed in an identical manner.

We may now write the quasigeostrophic equations for the ocean as

$$ {}^{o}\mathbf{q}_t + \frac{1}{f_0} J({}^{o}\mathbf{p}, {}^{o}\mathbf{q}) + \frac{\beta}{f_0} {}^{o}\mathbf{p}_x = {}^{o}B\,{}^{o}\mathbf{e} + \frac{{}^{o}A_2}{f_0} \nabla_H^4 {}^{o}\mathbf{p} - \frac{{}^{o}A_4}{f_0} \nabla_H^6 {}^{o}\mathbf{p} \tag{2.5} $$

where ${}^{o}A_2 = 50\,\mathrm{m^2 s^{-1}}$ and ${}^{o}A_4 = 2.0 \times 10^9\,\mathrm{m^4 s^{-1}}$ are the Laplacian and biharmonic diffusion coefficients, respectively. The Jacobian operator is given by $J(\mathbf{f},\mathbf{g}) = \mathbf{f}_x\mathbf{g}_y - \mathbf{f}_y\mathbf{g}_x$ and the horizontal Laplacian and biharmonic operators are given by ∇_H^4 and ∇_H^6, respectively. The forcing in the QG layers is defined by the 3×4 matrix ${}^{o}B$ and the 4×1 entrainment vector ${}^{o}\mathbf{e}$. The QG equations for the atmosphere are similar except that there is no Laplacian viscosity term and the aforementioned entrainment vector, or forcing terms, are different. These will now be described in the following paragraphs.

Table 2.1: Q-GCM parameters for the double gyre ocean model in benchmark modelled climate

Parameter	Value	Description
${}^oX \times {}^oY$	4800 km × 4800 km	Domain size
$\Delta^o x$	5 km	Horizontal grid spacing
$\Delta^o t$	540 s	Time step
${}^oH_k$	(350, 750, 2900) m	Layer thickness
${}^oH_m$	100 m	Mixed layer thickness
${}^o\rho$	1000 $\mathrm{kg\,m^{-3}}$	Density
${}^oC_p$	4000 $\mathrm{J\,kg^{-1}\,K^{-1}}$	Specific heat capacity
${}^og'_k$	(0.0222, 0.0169) $\mathrm{m\,s^{-2}}$	Reduced gravity
${}^oA_2$	(50, 50, 50) $\mathrm{m^2\,s^{-1}}$	Laplacian viscosity coefficient
${}^oA_4$	2.0×10^9 $\mathrm{m^4\,s^{-1}}$	Biharmonic viscosity coefficient
${}^o\alpha_{bc}$	0.0417	Partial-slip BC coefficient
${}^oK_2$	50 $\mathrm{m^2\,s^{-1}}$	Laplacian diffusion coefficient
${}^oK_4$	2.0×10^9 $\mathrm{m^4\,s^{-1}}$	Biharmonic diffusion coefficient
${}^or_{dk}$	(40.0, 20.6) km	Baroclinic Rossby radii

Entrainment vectors

In the ocean, the matrix B is given by

$$ {}^oB = f_0 \begin{bmatrix} \frac{1}{H_1} & -\frac{1}{H_1} & 0 & 0 \\ 0 & \frac{1}{H_2} & -\frac{1}{H_2} & 0 \\ 0 & 0 & \frac{1}{H_3} & -\frac{1}{H_3} \end{bmatrix} \tag{2.6} $$

In the atmosphere, we simply have ${}^aB = -{}^oB$ and different layer thicknesses ${}^aH_i$ (see Table 2.2). The entrainment vectors ${}^o\mathbf{e}$ and ${}^a\mathbf{e}$ for the ocean and atmosphere, respectively, are given by

$$ {}^o\mathbf{e} = \begin{bmatrix} {}^ow_{\mathrm{ek}} \\ -\frac{\Delta^o_m T_o}{2\Delta^o_1 T}\,{}^ow_{\mathrm{ek}} \\ 0 \\ \frac{\delta_{\mathrm{ek}}}{2f_0}\nabla^2_H\,{}^op_3 \end{bmatrix}, \quad {}^a\mathbf{e} = \begin{bmatrix} {}^aw_{\mathrm{ek}} \\ \frac{F^{\uparrow}_m + F^{\downarrow}_k - F^{\uparrow}_N}{{}^a\rho} \\ 0 \\ 0 \end{bmatrix} \tag{2.7} $$

These forcing vectors correspond to vertical velocities into each QG layer. For example, In the i-th isopycnal ocean layer, ${}^oe_{i-1}$ is the entrainment velocity out of the top of the layer and ${}^oe_i$ is the entrainment velocity out of the bottom of the layer. These terms are derived either as a consequence

of mixed and Ekman layer dynamics, or through double-sided entrainment heat fluxes (McDougall and Dewar, 1998), where vertical velocities are induced by heat transfers between layers (Hogg et al., 2014). Within the upper-isopycnal ocean layer, we combine the adiabatic and diabatic forcing as a single term to simplify our subsequent analysis. We call this term the *upper-ocean total entrainment*[2]

$$ {}^{o}e_{\text{total}} = {}^{o}e_0 - {}^{o}e_1 = {}^{o}w_{\text{ek}} + \frac{\Delta^o_m T}{\Delta^o_1 T} {}^{o}w_{\text{ek}} \tag{2.8} $$

Ekman pumpings in the ocean and atmosphere are computed as the curl of surface stress (dropping left-superscripts)

$$ w_{\text{ek}} = \frac{1}{f_0}(\tau^y_x - \tau^x_y) \tag{2.9} $$

The atmosphere surface-stress, or wind-stress, field is computed as a linear combination of lower-isopycnal atmosphere velocities:

$$ {}^{a}\tau^x = C_D M \frac{{}^{a}u_1 - (a+b)M{}^{a}v_1}{1+(a+b)^2M^2},\ {}^{a}\tau^y = C_D M \frac{{}^{a}v_1 + (a+b)M{}^{a}u_1}{1+(a+b)^2M^2} \tag{2.10} $$

where $a = C_D/({}^{a}H_m f_0), b = {}^{a}\rho C_D/({}^{o}\rho {}^{o}H_m f_0)$ with $C_D = 1.3 \times 10^{-3}$ as the dimensionless air-sea drag coefficient and $M = |{}^{a}u_m - {}^{o}u_m|$. Ocean surface-stresses are computed as a density ratio of atmosphere surface-stress, i.e.

$$ {}^{o}\tau = \frac{{}^{a}\rho}{{}^{o}\rho} {}^{a}\tau \tag{2.11} $$

This means that ocean Ekman pumping depends only on the atmospheric flow and does not explicitly depend on the ocean flow[3]. Since the atmosphere and ocean surface-stress fields are proportional and determined by the atmospheric circulation, we will refer to both of the fields interchangeably as wind-stresses.

[2]The combining of the adiabatic and diabatic forcings is justified because, as it turns out in Subsection 3.3.4, the leading modes of variability of both components are controlled by the same modes of atmospheric variability.

[3]Q-GCM does allow for ocean velocities to be included into the computation of surface stresses but we have chosen not to do so in order to simplify mechanical atmosphere-ocean interactions

The atmosphere diabatic entrainment may be expanded as

$$ {}^{a}e_1 = \frac{1}{{}^{a}\rho\,{}^{a}C_p\Delta_1{}^{a}T}\left[\sum_{k=1}^{N-1}(A_{1,k}-A_{N,k})^{a}\eta_1\right]+(Bm^{\uparrow}+B_1^{\downarrow}-B_N^{\uparrow})^{a}\eta_m+(C_m^{\uparrow}+C_1^{\downarrow}-C_N^{\uparrow})^{a}D+(D_m^{\uparrow}-D_N^{\uparrow})^{a}T'_m \tag{2.12} $$

which contains vertical velocities induced by linearised radiative flux perturbations due to changes in the underlying atmospheric mixed layer (see Section 2.1). The above constants A,B,C,D are derived from linearisation of equations that govern radiative fluxes in the atmosphere (see Hogg et al., 2014, for details).

When an unstable stratification occurs, the mixed layer and lower-isopycnal atmosphere exchange heat and entrainment ${}^{a}e_1$ is adjusted by

$$ \delta^{a}e_1 = \frac{{}^{a}h_m({}^{a}T_1-{}^{a}T_m)}{2\Delta{}^{a}t\Delta_1^{a}T} \tag{2.13} $$

and set ${}^{a}T_m = {}^{a}T_1$. The lower-isopycnal atmosphere temperature ${}^{a}T_1$ is fixed, $\Delta^{a}t$ is the atmospheric time-step and $\Delta_1^{a}T = {}^{a}T_1 - {}^{a}T_2$.

Boundary conditions

Partial-slip boundary conditions are applied on the lateral boundaries (Haidvogel et al., 1992) by

$$ {}^{o}p_{i_{nn}} = -\frac{{}^{o}\alpha_{\mathrm{bc}}}{\Delta^{o}x}{}^{o}p_{i_n} \tag{2.14} $$

$$ {}^{o}p_{i_{4n}} = -\frac{{}^{o}\alpha_{\mathrm{bc}}}{\Delta^{o}x}{}^{o}p_{i_{3n}} \tag{2.15} $$

where α_{bc} is the non-dimensional partial-slip boundary condition parameter (see Tables 2.1, 2.2) and $\Delta^{o}x$ is the horizontal grid spacing. The subscript n denotes outward normal partial derivatives. We choose a partial-slip boundary condition parameter that is close to free-slip as this gives a more realistic representation of the nonlinear dynamics in the WBCs, see Deremble et al. (2011) for details. Note that the meridional boundaries on the atmosphere are periodic so partial-slip boundary conditions are not applied there.

There are also conservation constraints applied to the lateral boundaries (McWilliams, 1977). In the box ocean case, this is given by

$$ {}^{o}p_k = f_k(t) \tag{2.16} $$

which is constant pressure along the boundaries but varying in time and determined by mass conservation. In the channel atmosphere case, a more complicated mixed boundary condition which combines both mass and momentum conservation is applied. This means that the values of pressure on the north and south boundaries may differ from each other (Hogg et al., 2014).

Table 2.2: Q-GCM parameters for the channel atmosphere model in benchmark modelled climate

Parameter	Value	Description
${}^{a}X \times {}^{a}Y$	30 720 km × 7680 km	Domain size
$\Delta^{a}x$	20 km	Horizontal grid spacing
$\Delta^{a}t$	30 s	Time step
${}^{a}H_k$	(2000, 3000, 4000) m	Layer thickness
${}^{a}H_m$	1000 m	Mean BL thickness
${}^{a}\rho$	$1\ \mathrm{kg\,m^{-3}}$	Density
${}^{a}C_p$	$1000\ \mathrm{J\,kg^{-1}\,K^{-1}}$	Specific heat capacity
${}^{a}g'_k$	$(1.2, 0.4)\ \mathrm{m\,s^{-2}}$	Reduced gravity
${}^{a}A_4$	$1.6 \times 10^{12}\ \mathrm{m^4\ s^{-1}}$	Biharmonic viscosity coefficient
${}^{a}\alpha_{bc}$	1	Partial-slip BC coefficient
${}^{a}K_2$	$6.25 \times 10^{3}\ \mathrm{m^2\,s^{-1}}$	Laplacian diffusion coefficient
${}^{a}K_4$	$1.6 \times 10^{12}\ \mathrm{m^4\,s^{-1}}$	Biharmonic diffusion coefficient
K_η	$5.0 \times 10^{4}\ \mathrm{m^2\ s^{-1}}$	Diffusion coefficient for ${}^{a}\eta_m$
${}^{a}r_{dk}$	(496, 259) km	Baroclinic Rossby radii

Radiative heat fluxes

The entire model is driven by solar radiation which is fixed in time and depends on latitude

$$ F_s(y) = \overline{F_s} + \frac{F'_s}{2} \sin\left(\frac{\pi(y - y_0)}{{}^{a}Y}\right) \tag{2.17} $$

Solar radiation is transparent to the atmosphere but opaque to the land and ocean surface. The radiation is then re-emitted in the form of blackbody radiation. The re-emitted blackbody radiation is redistributed by a linearised radiation scheme. Radiative fluxes are denoted with arrow superscripts $\uparrow$

and $\downarrow$ which indicate whether the radiative flux is moving up or down into the layer in question. For more details we forward the reader to Hogg et al. (2014) where the radiation scheme is discussed in depth.

Sensible and latent heat fluxes

Sensible and latent heat fluxes are parametrised by a single term

$$ {}^{a}F_{\lambda} = \lambda({}^{o}T_m - {}^{a}T_m) \tag{2.18} $$

where $\lambda = 35\,\mathrm{Wm}^{-2}\mathrm{K}^{-1}$ is the sensible and latent heat flux coefficient.

The ocean surface mixed layer

The SST evolution in the ocean surface mixed layer, denoted by ${}^{o}T_m$, is given by

$$ {}^{o}T_{mt} + ({}^{o}u_m\,{}^{o}T_m)_x + ({}^{o}v_m\,{}^{o}T_m)_y = {}^{o}K_2\nabla_H^2\,{}^{o}T_m - {}^{o}K_4\nabla_4^2\,{}^{o}T_m - \frac{{}^{o}w_{\mathrm{ek}}({}^{o}T_1 + {}^{o}T_m)}{2^{o}H_m} + \frac{{}^{o}F_0 + {}^{o}F_m^{e+}}{{}^{o}\rho\,{}^{o}C_p\,{}^{o}H_m} \tag{2.19} $$

where ${}^{o}T_m$ denotes SST and $({}^{o}u_m, {}^{o}v_m)$ are the mixed layer velocities. These are computed through the Ekman balance integrated over the mixed layer depth, which gives

$$ {}^{o}u_m = {}^{o}u_1 + \frac{{}^{o}\tau^{y}}{{}^{o}H_m f0}, {}^{o}v_m = {}^{o}v_1 - \frac{{}^{o}\tau^{x}}{{}^{o}H_m f_0} \tag{2.20} $$

We also have ${}^{o}T_1$ which is a fixed, constant temperature of the upper-isopycnal ocean. Note that the other isopycnal layers also have constant temperatures of ${}^{o}T_2$ and ${}^{o}T_3$. We will present ${}^{o}T_m$ as a deviation from a temperature constant which is obtained through radiative balance (see Hogg et al., 2014, for details). For our model parameters, this constant temperature for the ocean mixed layer is 27.0°C. Note that (2.19) also contains Laplacian and biharmonic diffusivities given by ${}^{o}K_2$ and ${}^{o}K_4$, respectively (see Table 2.1).

The forcing terms in (2.19) are given by: ${}^{o}F_0 = -F_{\lambda} - F_0^{\uparrow} - F_m^{\uparrow} - F_m^{\downarrow} - F_s$ which is the thermal forcing

at the ocean surface containing sensible and latent heat fluxes F_λ (2.18), radiative fluxes $F_m^\uparrow$, $F_m^\downarrow$, solar forcing F_s (2.17) and ${}^oF_m^{e+}$ which is the entrainment heat flux out of the bottom of the ocean mixed layer. This heat flux corresponds to the heat exchange that takes place due to Ekman pumping out of the bottom of the ocean mixed layer.

The atmosphere surface mixed layer

Unlike the ocean surface mixed layer, the thickness of the atmosphere surface mixed layer, denoted by ${}^ah_m$, varies through the equation

$$ {}^ah_{mt} + ({}^au_m{}^ah_m)_x + ({}^av_m{}^ah_m)_y = -{}^ae_m \tag{2.21}$$

where ${}^ae_m$ is entrainment out of the mixed layer. The temperature evolution of the atmospheric mixed layer is given by

$$ {}^aT_{mt} + ({}^au_m{}^aT_m)_x + ({}^av_m{}^aT_m)_y = {}^aK_2\nabla_H^2{}^aT_m - {}^aK_4\nabla_4^{2a}T_m - \frac{{}^aw_{\text{ek}}{}^aT_m}{{}^aH_m} + \frac{-{}^aF_m + {}^oF_0}{{}^a\rho{}^aC_p{}^ah_m} \tag{2.22}$$

This equation is similar to (2.19) except the forcing terms are slightly different with heat flux at the top of the atmospheric mixed layer given by ${}^aF_m = F_m^\uparrow + F_1^\downarrow + F_m^{e-}$ and surface forcing given by

$$ {}^aF_0 = \begin{cases} F_m^\uparrow + F_\lambda + F_0^\uparrow & \text{, over ocean} \\ -F_s' & \text{, over land} \end{cases} \tag{2.23}$$

where F_s' is the perturbation of solar forcing that depends on latitude.

Breaking artificial symmetries in ocean forcing

It has been shown that QG ocean models with anti-symmetric wind-forcing show artificially suppressed low-frequency behaviour (Berloff and McWilliams, 1999a). In order to further reduce artificial symmetries in the ocean model forcing we made two adjustments to the model. Firstly, we shifted the ocean basin south by 480 km, which corresponds to 10% of the basin width. This creates a smaller

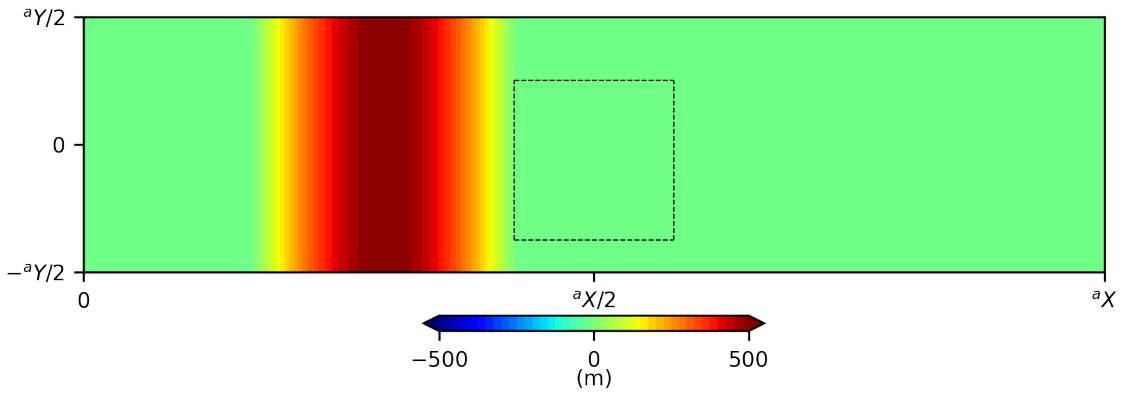

Figure 2.1: Land orography ${}^{a}D(x,y)$ (2.24). Profile mimics a continental land mass such as the North American continent which lies to the west of the North Atlantic basin. Black dashed line indicates the position of the shifted ocean basin which lies to the east of the land mass.

region of forcing over the subpolar gyre. Secondly, we added land orography located to the west of the ocean basin which is added to mimic a continental land mass, e.g. the North American land mass, and deflect the axis-tilt of the atmospheric jet polewards over the ocean basin. The addition of land orography is denoted ${}^{a}D(x,y)$ and is prescribed as a cosine hat

$$ {}^{a}D(x,y) = \begin{cases} 500\cos\left(\frac{\pi(x-x_c)}{2r_0}\right) \text{ m} & \text{, if } \|x-x_c\| < r_0 \\ 0, & \text{, elsewhere} \end{cases} \tag{2.24} $$

where $x_c = 9060$ km is the central longitude of the land mass and $r_0 = 3900$ km determines its width.

2.1.1 Partially-coupled experiments

In order to attribute features of the modelled climate and pinpoint sources of variability to ocean-induced or coupled effects, we run a partially-coupled modelled climate alongside our fully-coupled climate simulation. This is done by changing a parameter X_C which controls the coupling between the atmospheric mixed layer and the lower-isopycnal atmosphere. More specifically, X_C adjusts the layer-1 entrainment through the the following term:

$$ {}^{a}e_1 = \frac{X_C F^{\uparrow} + (1-X_C)\overline{F^{\uparrow}}}{{}^{a}\rho\, {}^{a}C_p \Delta_1^a T} \tag{2.25} $$

where $F^{\uparrow}$ is instantaneous diabatic heating and $\overline{F^{\uparrow}}$ is the time-averaged diabatic heating obtained from a fully-coupled simulation. When $X_C = 1$, we have a fully coupled system and when $X_C = 0$, the atmosphere is decoupled from atmospheric surface mixed layer variability. This coupling parameter is useful as any SST-induced phenomena will be suppressed while purely atmosphere-driven phenomena will remain. In our case, we will set $X_C = 0$. Note that mechanical interactions between the ocean and atmosphere are implemented identically to the fully coupled case.

2.1.2 Ocean-only configuration

Along with the ability to model partially-coupled climates, Q-GCM offers the option to run the model under ocean-only, and atmosphere-only (omitted), configurations (Hogg et al., 2014). In an ocean-only configuration, the atmosphere model is simply switched off and only the ocean QG and mixed layer evolution is modelled. Since the atmospheric evolution is now ignored, forcings in the ocean-only configurations must be given by prescribed, fixed mechanical and thermal forcings that consist of: 1) wind-stresses τ and 2) diabatic heating F_0. These forcings are obtained by time-averaging a fully coupled climate simulation and may be modified as necessary, e.g. adding some fixed wind-stress perturbation.

Within the model described above, these forcings may be implemented by making the following modifications:

1. Compute the fixed Ekman pumping field using (2.9) to define the ocean entrainment vector (2.7). Note the evolution of $\Delta_m^o T$ is still modelled since the ocean mixed layer is active.
2. Use the fixed diabatic heating term to act as the thermal forcing term ${}^oF_0$ in (2.19).

This fully defines the forcings in the ocean-only configuration.

Switching off convection

Given an unstable temperature stratification of the ocean, i.e. when ${}^oT_m$ falls below ${}^oT_1$, a convective event is modelled by adding a correction term $\delta^o e_1$. However within the ocean-only configuration

of this model, we found that this led to unrealistically large levels of modelled convection of nearly two orders of magnitude greater than expected around the eastward jet separation region (see Fig. A.1 in Appendix A.2). In order to manage this undesirable effect, we switched off convection in our modelled double gyre circulations by setting the entrainment correction term to zero (see Appendix A.2 for full details).

2.2 Statistical methods

We now describe the main post-processing tools and statistical methods used in Chapters 3 and 4 of this thesis.

2.2.1 Low-pass filtering

Before any statistical techniques are applied to the data, a simple 2-year brick wall low-pass filter is applied to remove high frequency oscillations. This allows for any low-frequency signals associated with ocean gyre dynamics to be picked up more easily while high-frequency noise due to atmospheric fluctuations are filtered out.

2.2.2 Empirical orthogonal functions (EOFs)

An empirical orthogonal function (EOF) decomposition consists of computing an eigendecomposition of a covariance matrix obtained from the oceanic/atmospheric state variables (von Storch and Zwiers, 1999). The EOF decomposition of a $m \times m$ symmetric positive definite matrix M is given by

$$M = V\Sigma V^T \tag{2.26}$$

where Σ is a $m \times m$ square diagonal matrix and V is a $m \times m$ orthogonal matrix. The columns of V are known as the EOFs and diagonal entries of Σ are known as the singular values which may be interpreted as the explained variance of the corresponding EOF.

This decomposition gives from most to least important, the patterns of variability (EOFs) that explain the most variance in the data. We will present the explained variance fraction of each EOF as a percentage of the total variance. The filtered data set is then projected onto the EOFs to obtain the principal components (PCs) which gives information about the temporal evolution of the EOFs. Analysing the power spectra will also give indications about the most important time-scales at play.

2.2.3 Lagged singular value decompositions (SVDs)

Although EOFs are useful in decomposing single field variability, they lack information regarding modes of covariability in the modelled climate, e.g. ocean-atmosphere interactions. In order to pick out these modes of covariability, a SVD is performed on a lagged cross-covariance matrix constructed using two state variables (Bretherton et al., 1992). The SVD of a $m \times n$ matrix M is given by

$$M = U\Sigma V^T \tag{2.27}$$

where U is a $m \times m$ orthogonal matrix, V is a $n \times n$ orthogonal matrix and Σ is a $m \times n$ rectangular diagonal matrix. The existence of a SVD for a matrix M may be shown by taking the EOF decompositions of MM^T and M^TM, respectively (e.g. see Bretherton et al. (1992)). Interpretation of the columns of U and V is analogous to the EOF decomposition and are known as the singular vectors. The diagonal entries of Σ may similarly be interpreted as the singular values or occupied cross-covariances by the corresponding singular vector.

Similar to the EOF decomposition, the data is first 2-yr low-pass filtered and both fields are subsampled onto an 80 km grid. This is to save on memory cost as cross-covariance matrices require considerably larger storage than covariance matrices. By maximising squared covariance fraction with respect to time-lag, the likely time-scale for any delayed response may also be obtained, if one exists. Analogous to the EOF decomposition, a SVD produces patterns that maximise the cross-covariance in the data. Note that as we are concerned with pairs of fields, two sets of patterns are produced in the decomposition- one for each field. These are called the singular vectors or SVD modes. Again, by projecting the original data sets onto these modes, we obtain two sets of temporal coefficients. These

may be correlated to obtain a measure of the strength of the coupling between the pair of singular vectors. A description of the required SVDs will be given in Section 3.4.

2.3 Diagnostic tools

Other diagnostic tools have been used throughout this thesis which we will now describe.

2.3.1 The inter-gyre boundary

An inter-gyre boundary that partitions the ocean basin is computed by following the time-averaged pressure contour emanating from the western boundary. This approximates the position of the eastward jet extension as it separates from the western boundary and extends into the open ocean. The inter-gyre boundary will also be necessary in the computation of PV budgets which are described in the next subsection. Note that complicated geometries of the jet, such as the jet stacking on itself in an 'S' shape are in practice not found and thus do not need to be considered any further.

2.3.2 PV budgets

In subsequent chapters, we will need to fully quantify PV sources and sinks in the ocean gyres to discern what physical processes are governing any changes in observed circulation. For example, if a poleward shift in the eastward jet extension is observed, how do the viscous boundary fluxes change? How do the inter-gyre PV fluxes change? Which is more important? The computation of PV budgets allows us to measure relative importances of physical processes that govern changes in the ocean gyre circulation in a way that is both accurate and informative.

The PV budgets for the purpose of this thesis will be time-averaged over a given time period and integrated over each gyre for the modelled double gyre circulation in statistical equilibrium. The inter-gyre boundary will be computed using the aforementioned method in Subsection 2.3.1.

Source and sink terms

As we are interested in wind-induced phenomena, our focus will lie in the upper- and middle-isopycnal layers which are driven directly by the atmosphere. The governing PV equation in the upper-isopycnal layer is given by

$$\frac{\partial q_1}{\partial t} + \frac{1}{f_0} J(p_1, q_1 + \beta(y - y_0)) = \frac{f_0}{H_1}\left(w_{\text{ek}} + \frac{\Delta_m T}{2\Delta_1 T} w_{\text{ek}}\right) + \frac{A_2}{f_0}\nabla^4 p_1 - \frac{A_4}{f_0}\nabla^6 p_1 \tag{2.28}$$

A similar equation may be written for the middle-isopycnal layer. Note that the advection of full PV $q + \beta y$ is considered here.

We will now break down the source and sink terms in (2.28). Similar terms may be obtained for the middle-isopycnal layer. The two source terms in our equation are given by Ekman pumping w_{ek} and entrainment $e_1 = -\frac{\Delta_m T}{2\Delta_1 T} w_{\text{ek}}$. For a given inter-gyre boundary Γ, the gyre-integrated PV fluxes, denoted G, are computed by integrating the source terms within the region encapsulated by the ocean boundaries and the inter-gyre boundary.

$$G_{\text{EP}} = \frac{f_0}{H_1}\overline{\iint_{\text{gyre}} w_{\text{ek}}\,\mathrm{d}x\,\mathrm{d}y}\,, \quad G_{\text{ENT}} = \frac{f_0}{H_1}\overline{\iint_{\text{gyre}} e_1\,\mathrm{d}x\,\mathrm{d}y} \tag{2.29}$$

These two terms are combined into a single wind-induced PV flux source term to give

$$G_{\text{W}} = G_{\text{EP}} + G_{\text{ENT}} \tag{2.30}$$

In the middle isopycnal layer, there is no adiabatic Ekman pumping term present and the sign of the diabatic entrainment flux is flipped (2.7).

Moving onto the sink terms, the viscous boundary fluxes are computed by first integrating the last two terms in (2.28). Integrating the Laplacian viscosity term over the gyre gives:

$$\frac{A_2}{f_0}\overline{\iint_{\text{gyre}} \nabla^4 p_1\,\mathrm{d}x\,\mathrm{d}y} = \frac{A_2}{f_0}\overline{\int_{C\setminus\Gamma} \nabla(\nabla^2 p_1)\cdot\mathbf{n}\,\mathrm{d}s} + \frac{A_2}{f_0}\overline{\int_{\Gamma} \nabla(\nabla^2 p_1)\cdot\mathbf{n}\,\mathrm{d}s} = G_{\text{VB2}} + G_{\text{IV2}} \tag{2.31}$$

Similarly, integrating the biharmonic viscosity term gives:

$$\frac{A_4}{f_0}\overline{\iint_{\text{gyre}} \nabla^6 p_1 \,\mathrm{d}x\,\mathrm{d}y} = \frac{A_4}{f_0}\overline{\int_{C\setminus\Gamma} \nabla\left(\nabla^4 p_1\right)\cdot\mathbf{n}\,\mathrm{d}s} + \frac{A_4}{f_0}\overline{\int_{\Gamma} \nabla\left(\nabla^4 p_1\right)\cdot\mathbf{n}\,\mathrm{d}s} = G_{\text{VB4}} + G_{\text{IV4}} \tag{2.32}$$

where first and second terms in (2.31) and (2.32) represent the viscous boundary and inter-gyre viscous fluxes for the Laplacian and biharmonic viscosity terms, respectively. The inter-gyre viscous fluxes were found to be negligible and not considered any further. The viscous boundary fluxes are combined into a single term

$$G_{\text{VB}} = G_{\text{VB2}} + G_{\text{VB4}} \tag{2.33}$$

The inter-gyre flux of full PV $q+\beta y$ is computed by integrating the Jacobian term in (2.28)

$$G_{\text{IF}} = -\frac{1}{f_0}\overline{\iint_{\text{gyre}} J(p_1, q_1 + \beta(y-y_0))\,\mathrm{d}x\,\mathrm{d}y} \tag{2.34}$$

Finally, the tendency term is computed by either integrating $\frac{\partial q_1}{\partial t}$ over the gyre or equivalently, and more simply, by summing the above PV fluxes

$$G_{\text{T}} = G_{\text{W}} + G_{\text{VB}} + G_{\text{IF}} \tag{2.35}$$

This completes the source and sink terms in the PV budget. Multiple PV budgets will be computed in this study which each correspond to different Ekman pumping forcing regimes due to the atmospheric variability. Combining PV flux sources in (2.30, 2.33) allows for a simpler PV budget and a more transparent analysis in subsequent sections.

2.3.3 Lagrangian particles

The tracking of Lagrangian particles is a powerful tool in understanding complex, nonlinear dynamics taking place in the double gyre circulation. Such techniques are useful due to their ability to capture ensemble behaviour of fluid parcels and long-range material transports. For example, through the Lagrangian framework, we are able to study the long-range transport of PV which the Eulerian

framework is not well suited to.

The ensemble behaviour of fluid parcels in the double gyre circulation may be measured by releasing N particles into the i-th isopycnal layer and solving

$$\frac{\mathrm{d}^o\mathbf{x}_i^j(t)}{\mathrm{d}t} = {}^o\mathbf{u}_i(t,\mathbf{x}_i^j(t))\,, \quad \text{for } j = 1,...,N\,, \tag{2.36}$$

where ${}^o\mathbf{x}_i^j(t)$ is the position of particle j in layer i at time t and ${}^o\mathbf{u}_i(t,\mathbf{x}) = ({}^ou_i(t,\mathbf{x}),{}^ov_i(t,\mathbf{x}))$ is the velocity of the flow at position $\mathbf{x}$ and time t. This system of equations (2.36) is solved offline using the 4th order Runga-Kutta scheme with a 2D cubic spatial interpolation and a 1D cubic temporal interpolation. Total PV $(q+\beta y)$ is estimated along the trajectories by using a 2-D cubic interpolation[4].

In our experiments in later chapters, these Lagrangian particles will be released in batches at different points in time to ensure a representative sample of the modelled ocean circulation.

Parts of this chapter have been taken from Kurashina et al. (2021) and Kurashina and Berloff (2022a,b), all of which is original work that has been conducted by the author.

[4]Total PV is used for Lagrangian particle analysis rather than PV anomalies because it is a materially-conserved quantity.

Chapter 3

Coupling of the wind-driven ocean gyres to jet streams: Anatomy

3.1 Introduction

We begin our analysis by decomposing the anatomy of the low-frequency variability in our benchmark modelled climate. Section 3.2 will show the reference solutions to the benchmark modelled climate and Section 3.3 will decompose its variability. The lagged covariability and ocean-atmosphere interactions are investigated in Section 3.4 with a final discussion of results given in Section 3.5.

3.2 Reference solutions for benchmark modelled climate

Reference solutions for the benchmark fully-coupled and partially-coupled climates are computed for a 120-yr simulation period with a 20-yr spinup period and data saved every 5 days. Full list of parameters are presented in Tables 2.2 and 2.1, see Section 2.1 for detail of the model. The simulation was started from rest and in radiative balance. Note that barred variables denote time-averages over the last 100-yrs in the data.

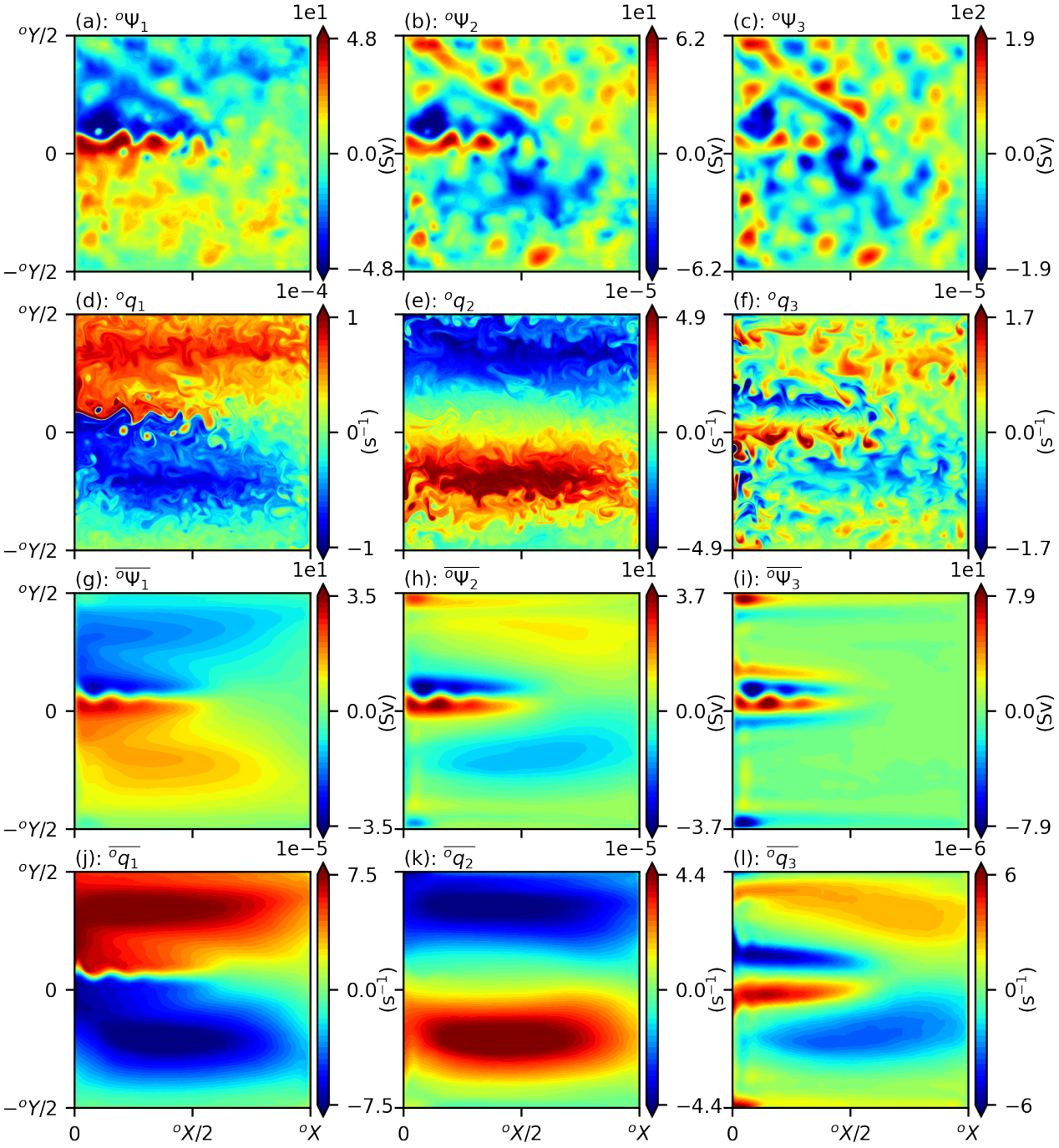

Figure 3.1: Instantaneous ocean PV anomalies and velocity streamfunction for the benchmark modelled double gyre circulation in statistical equilibrium. Panels from left to right show upper- to lower-isopycnal layers, respectively. Panels in the top-half of the figure show instantaneous fields and panels in bottom-half show time-averaged fields. (a - c): Instantaneous ocean transport streamfunction. (d - f): Instantaneous ocean PV anomaly. (g - i): Time-averaged ocean transport streamfunction fields. (j - l): Time-averaged ocean PV anomaly fields.

3.2.1 Ocean circulation

The modelled wind-driven, double gyre ocean circulation is presented in Fig. 3.1. The upper-isopycnal ocean is spun up by both adiabatic Ekman pumping and diabatic entrainment which creates the subpolar and subtropical gyres (see Fig. 3.3). Western intensification leads to the formation of powerful WBCs and downstream inertial recirculation zones and eastward jet extension. The basin shift and addition of land orography has created a larger subtropical gyre and has deflected the jet-axis tilt slightly polewards. The change in jet-axis tilt is less than expected, despite the relatively large land orography (2.24), because the natural tilt jet, i.e. with no increased land-sea contrast, is equatorward due to stronger diabatic forcing in the subtropical gyre (Hogg et al., 2005). The jet-axis tilt is determined by the relative strengths of the recirculation zones with the stronger recirculation zone tending to pull the jet towards itself (Moro, 1988). The middle-isopycnal ocean is forced only by the diabatic entrainment term (2.7) and eddy form drags. The sign change of PV in the middle-isopycnal layer is due to both the dominant circulation in the upper-isopycnal layer and sign-flip in diabatic entrainment. The PV homogenisation in the middle-isopycnal layer is the the classic eddy effect described in Rhines and Young (1982). Note that the eastward jet penetrates into the lower layers (see Figs. 3.1h,i) through the downwards transfer of eddy momentum via form drags (Holland, 1978).

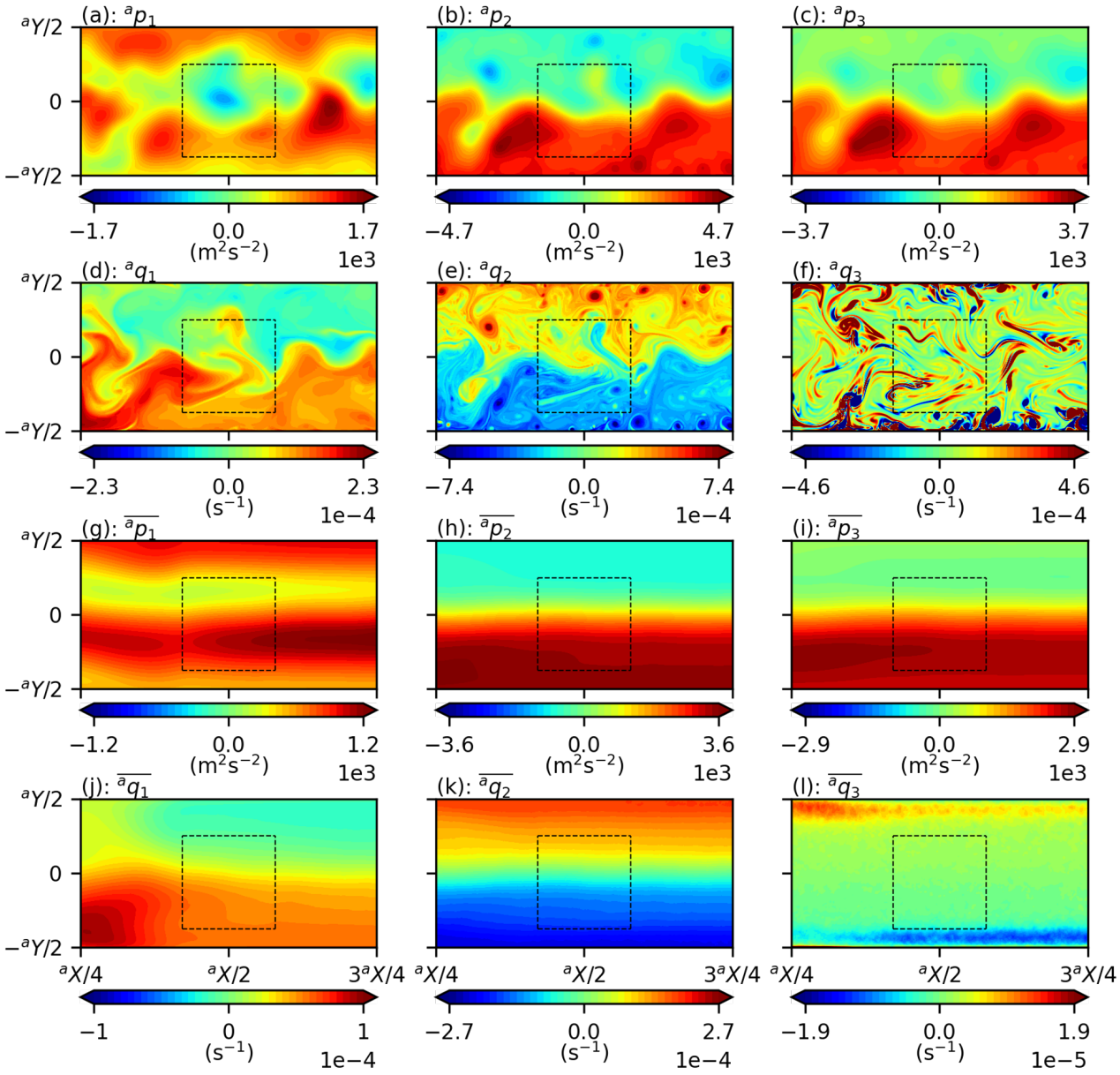

Figure 3.2: Instantaneous atmospheric PV anomalies and dynamic pressure anomalies for benchmark modelled channel atmosphere in statistical equilibrium. Panels from left to right show upper- to lower-isopycnal layers, respectively. Panels in the top-half of the figure show instantaneous fields and panels in bottom-half show time-averaged fields. Square box outlined by black dashed line represents the position of the ocean basin. Regions $0 \leq x \leq {}^{a}X/4$ and $3{}^{a}X/4 \leq x \leq {}^{a}X$ are omitted where ocean-atmosphere interactions are assumed to be weak. This is repeated for subsequent figures unless stated otherwise. (a - c): Instantaneous atmosphere dynamic pressure. (d - f): Instantaneous atmosphere PV anomaly. (g - i): Time-averaged atmosphere dynamic pressure. (j - l): Time-averaged atmosphere PV anomaly.

3.2.2 Atmosphere circulation

The modelled channel atmosphere circulation may be seen by looking at Fig. 3.2. Latitudinally varying solar radiation generates a PV gradient in the lower and middle-isopycnal atmosphere layers which leads to the formation of a zonally inhomogeneous westerly jet. The zonal inhomogeneity of the jet is created by the ocean basin shift and addition of land orography. This jet is dominated by large-scale, synoptic eddies and shows highly turbulent behaviour governed by intricate nonlinear dynamics. The westerly jet formed in the middle-isopycnal atmosphere dominates the circulation with its momentum supporting the lower-isopycnal layer via baroclinic instabilities (Hogg et al., 2003). This momentum pathway is also the main process by which the atmosphere drives the ocean through the consequent wind-stress anomalies generated by the atmosphere variability. The upper-isopycnal atmosphere is not forced directly by diabatic entrainments, and is only driven by eddies, so we will neglect its dynamics for the purposes of this chapter. Average speeds in the middle-isopycnal atmosphere are around $20\,\mathrm{ms}^{-1}$ while they are around $6\,\mathrm{ms}^{-1}$ in the lower-isopycnal atmosphere, roughly smaller by a factor of 3. This difference in circulation strengths is responsible for the sign change in PV in the lower-isopycnal layer. The circulation in the middle-isopycnal atmosphere dominates despite receiving weaker forcing than the lower-isopycnal atmosphere because it is not spun down by frictional wind-stresses, and the effect of considerably lower reduced gravities at the layer-2,3 interface allows for enhanced PV generation via the corresponding interface displacements that occur. A similar phenomenon with the change in PV sign occurs in the ocean QG layers (see Fig. 3.1) where the upper-isopycnal ocean dominates over the middle-isopycnal ocean circulation.

3.2.3 Ocean mixed layer

Instantaneous and time-averaged fields of SST anomalies, wind-induced ocean forcing and surface stresses are shown in Figs. 3.3 and 3.4. The subtropical and subpolar gyres in the ocean mixed layer are clearly visible and separated by a sharp SST front across the eastward jet (Figs. 3.3a,e). The eastward jet extension acts as a partial inter-gyre barrier, separating warmer waters in the subtropical gyre from the cooler waters in the subpolar gyre. Inter-gyre exchanges of warm and cool waters by mesoscale activity is also visible.

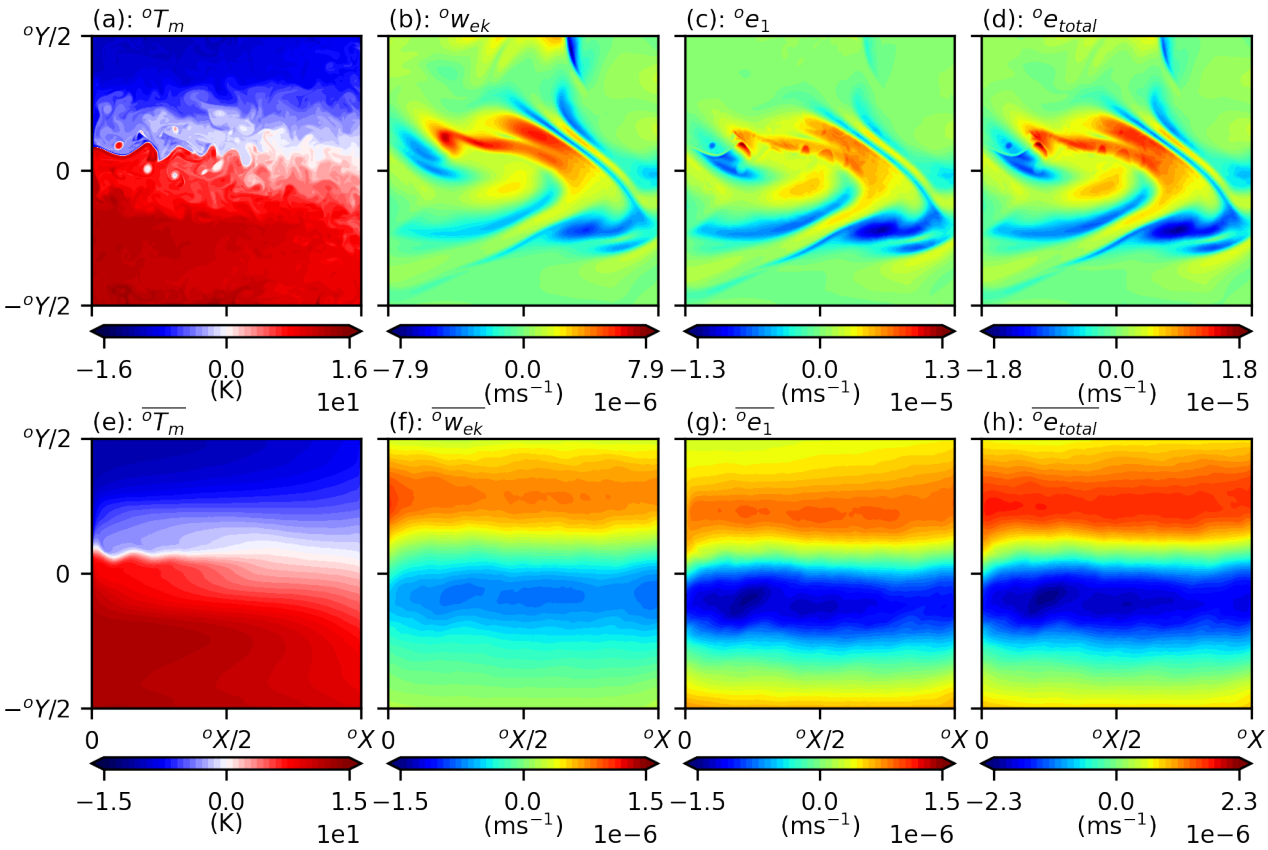

Figure 3.3: Instantaneous ocean SST and wind-induced forcing reference solutions for benchmark modelled climate in statistical equilibrium. Top and bottom panel rows correspond to instantaneous and time-averaged fields, respectively. (a, e): Ocean SST. (b, f): Ocean Ekman pumping. (c, g): Ocean diabatic entrainment. (d, h): Upper ocean total entrainment.

The time-averaged wind-stress is largely zonal with strong eastward wind-stresses focused in a fairly narrow band that sits predominantly over the subpolar gyre (Fig. 3.4c). The meridional wind-stress has time-averaged stresses of just over a quarter in magnitude of the zonal wind-stress with an average forcing in the poleward direction. This is associated with the addition of land orography west of the ocean basin which creates a mean flow that has a poleward wind-stress component. As these surface stresses are determined purely by the lower-isopycnal atmosphere velocities, they show both high spatial and temporal variability. These surface stresses then generate wind-curls that drive the ocean gyres in the form of both adiabatic Ekman pumping and diabatic entrainments. Although the sum of these forcings, i.e. the upper ocean total entrainment $^oe_{\text{total}}$, has roughly equal vorticity flux into each gyre, the adiabatic Ekman pumping component is stronger in the subpolar gyre (see Figs. 3.3f,h). This is due to the aforementioned location of the zonal surface stresses. The main effect of SSTs on the diabatic ocean entrainment is to push the zero vorticity flux line equatorward where $\Delta_1 T = {}^oT_m - {}^oT_1$

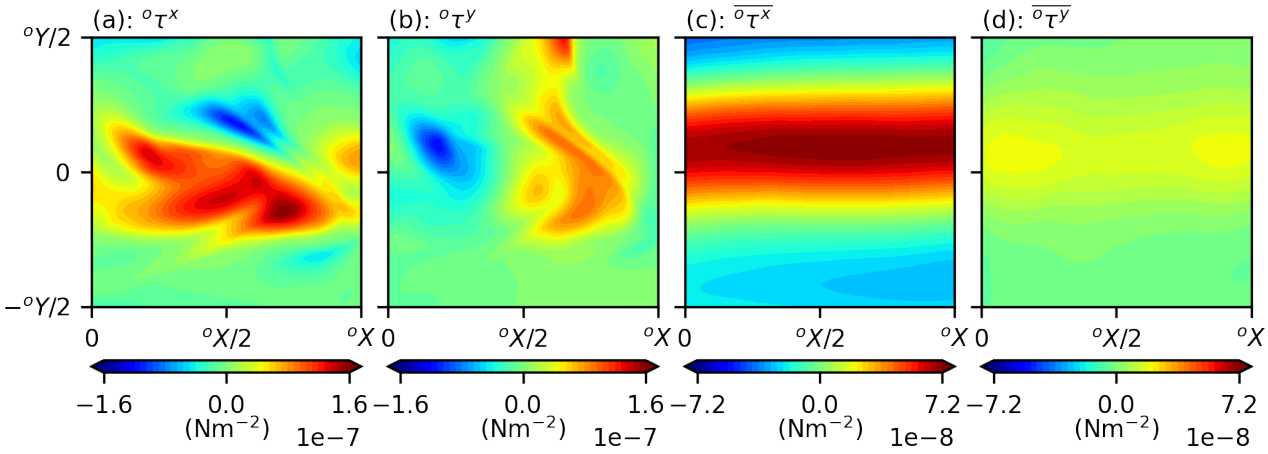

Figure 3.4: Instantaneous ocean surface stresses for benchmark modelled climate in statistical equilibrium. Left and right panels correspond to instantaneous and time-averaged fields, respectively. (a, b): Zonal ocean surface stress. (c, d): Meridional ocean surface stress.

is largest (2.7). These positive and negative vorticity fluxes over the subpolar and subtropical gyres, respectively, are fuelled by the atmosphere through frictional wind-stresses. However, the sign of PV anomalies in the atmospheric lower-isopycnal layer is inconsistent with the sign of Ekman pumping since negative PV anomalies sit at lower latitudes and increase as they move poleward[1] (see Fig. 3.2j). Hence, the PV driving the ocean gyres must originate from the middle-isopycnal layer which is consistent with our findings so far (and by Hogg et al., 2003) that the lower-isopycnal atmosphere is driven from above through momentum transfers that take place via baroclinic instabilities.

3.2.4 Atmosphere mixed layer

Fig. 3.5 shows atmospheric surface temperatures (ASTs), atmosphere diabatic entrainments and sensible and latent heat fluxes. The ASTs appear to be mostly controlled by the atmospheric circulation except over the ocean basin where the WBCs and double gyre circulation leave an imprint through the surface heat fluxes. Upward transfers of heat are given by positive heat fluxes, i.e. ocean warming atmosphere, and downward transfers of heat are given by negative heat fluxes, i.e. atmosphere warming ocean. We confirm that the sensible and latent heat fluxes give realistic patterns (Shaman et al., 2010; Kwon et al., 2010) which are strongest near the WBC separation point and the eastward

[1]The increase in PV with latitude through the planetary vorticity gradient β is not large enough to counteract the sign difference.

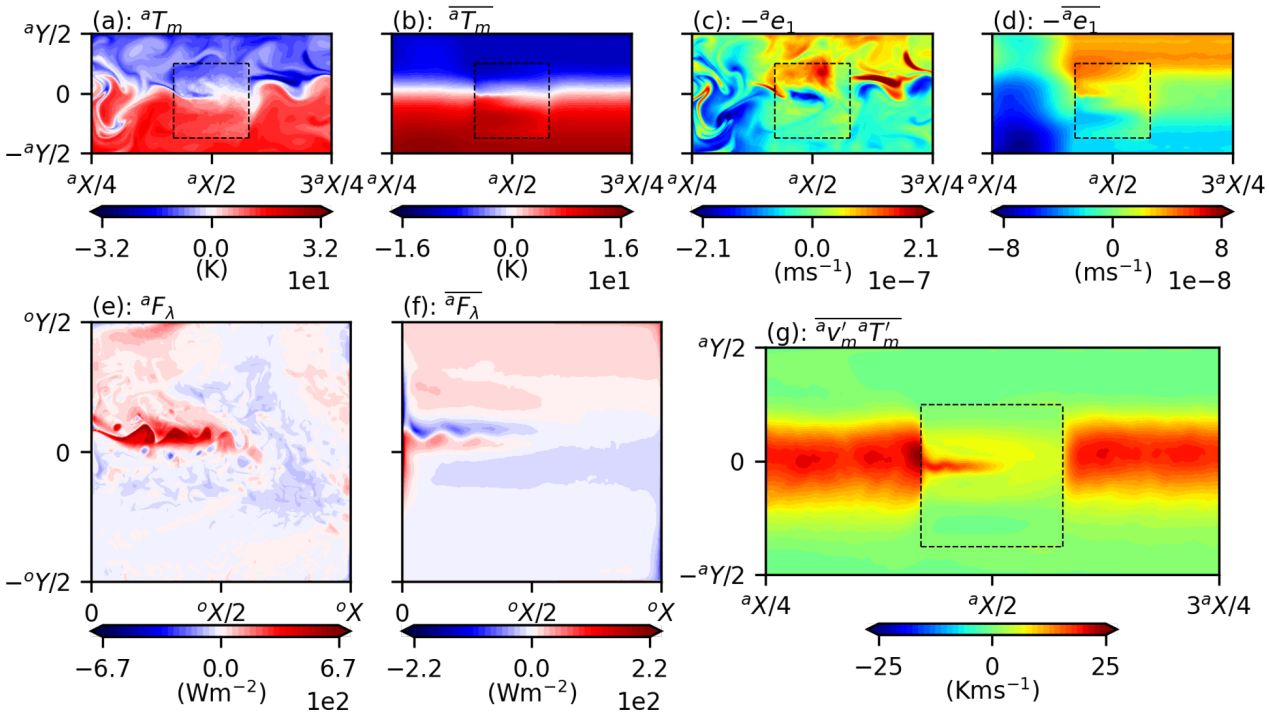

Figure 3.5: Instantaneous atmospheric mixed layer reference solutions for benchmark modelled climate in statistical equilibrium. (a, b): Instantaneous and time-averaged ASTs. (c, d): Instantaneous and time-averaged diabatic entrainments in the middle-isopycnal atmosphere. (e, f): Instantaneous and time-averaged sensible and latent heat fluxes into the atmosphere. Positive heat flux indicates heat gained by the atmosphere. (g): Time-averaged meridional eddy heat flux. (e, f) show heat fluxes over ocean basin region.

jet extension, and hence, strongly controlled by the ocean gyre circulation. The time-average effect of these heat fluxes is the warming and cooling of ASTs over the subtropical and subpolar WBCs, respectively. This consequently leads to a sharpening in meridional AST gradients over the ocean basin through the convergence of warm and cold waters by WBCs. Similar patterns of surface heat fluxes are obtained in Kravtsov et al. (2007) but ours show higher variability and time-averaged fluxes that extend well into the ocean interior due to the powerful eastward jet extension. The position of these strong sensible and latent heat fluxes over the WBCs and eastward jet extension coincides with the narrowing of meridional eddy heat fluxes in Fig. 3.5g. This eddy heat flux implies the convergence of ASTs due to eddies in the atmosphere mixed layer. Meridional eddy heat fluxes are active over the entire westerly atmospheric jet but they act over a larger latitudinal band outside ocean basin regions where synoptic scale turbulence destroys the low-level baroclinicity. The narrowing of this eddy heat flux latitudinal band by sharp SST gradients due to the WBCs is important in anchoring the westerly jet and increasing the low-level baroclinicity of the atmosphere (Nakamura et al., 2004, 2008). En-

hancement of time-averaged atmosphere diabatic entrainment due to increased land-sea contrast and the addition of land orography to the west of the ocean basin is clearly visible in Fig. 3.5d.

Our modelled climate is qualitatively very similar to those modelled by Hogg et al. (2006) and Kravtsov et al. (2007). However, some differences such as increased turbulent activity in both the ocean and atmosphere are important to note. In the ocean, this leads to a strengthened eastward jet extension via enhanced eddy backscatter in the inertial recirculation zones. This allows for greater amounts of heat transport by the jet as it is able to penetrate further into the ocean interior. This gives a greater longitudinal region for the ocean to thermally feed back onto the atmosphere, where previously only regions close to the western boundary were able to supply large enough sensible and latent heat fluxes to the atmosphere such as to measurably impact upon its dynamics. Furthermore, the effects of eddies in the lower-isopycnal behaviour must also not be ignored. The convergence of heat by meridional heat fluxes over the WBCs and eastward jet extension plays an important role in restoring the low-level baroclinicity. Now that we have shown reference solutions of the benchmark modelled climate we move onto describing the climate variability.

3.3 Low-frequency variability of modelled climate

We will now decompose the variability of the low-pass filtered ocean and atmosphere data. Furthermore, we must look at the variability of mixed layer variables that are responsible for mediating ocean-atmosphere interactions. These include forcings such as wind-induced Ekman pumping, ocean and atmosphere diabatic entrainments, as well as transfers of heat and momentum through wind-stresses and surface heat fluxes.

3.3.1 Upper-isopycnal ocean variability

The leading EOFs for the filtered upper-isopycnal ocean PV anomaly from the benchmark modelled climate are given in Fig. 3.6. EOFs 1 and 2 (Figs. 3.6a,b) explain 24.5% and 18.1% of the total variance in the data, respectively, with strong power at low frequencies (see Figs. 3.6c,d). EOF

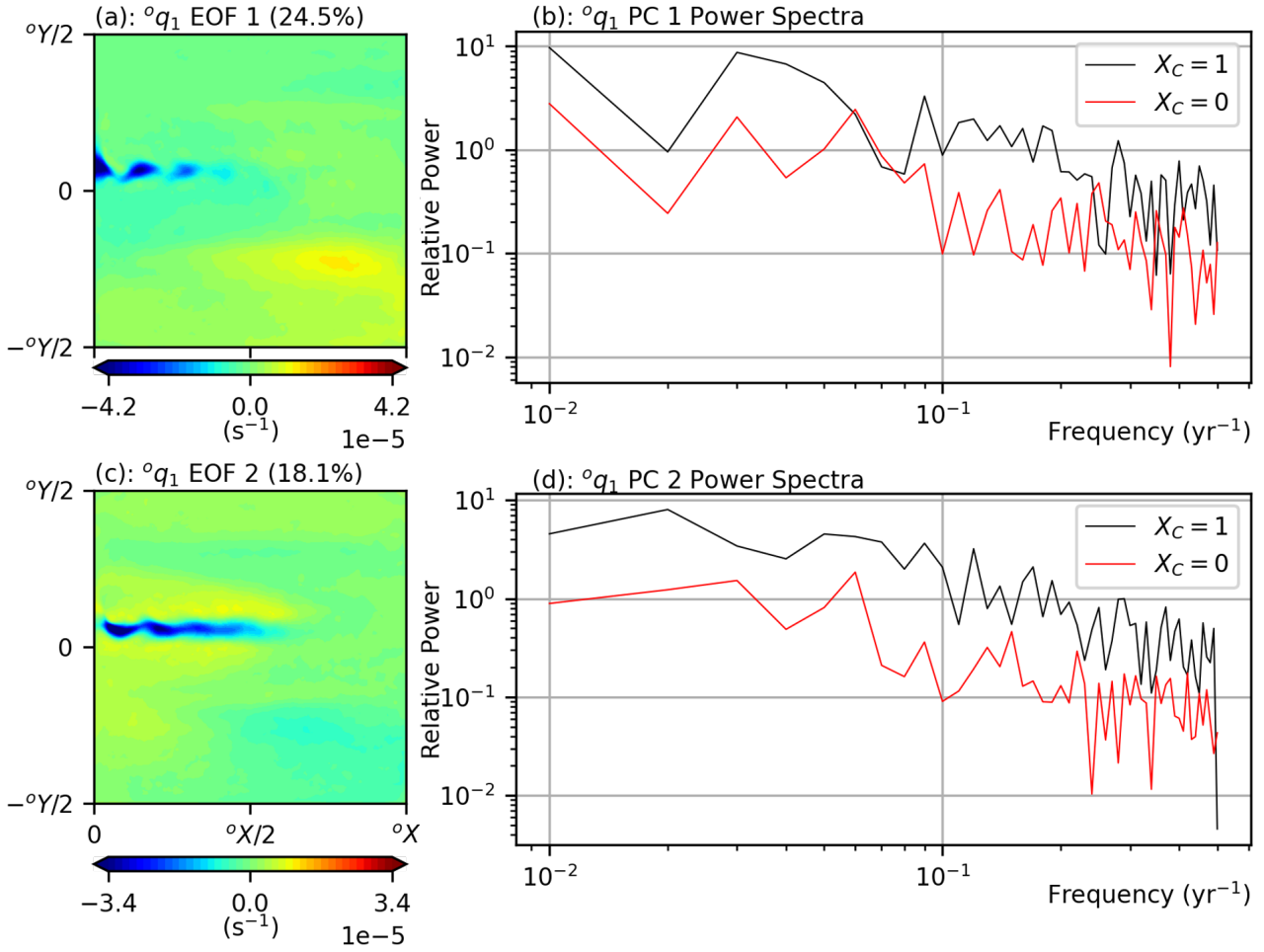

Figure 3.6: Leading EOFs of filtered upper-isopycnal ocean PV. (a): $^oq_1$ EOF 1. (b): Power spectra of PC 1 for coupled $(X_C = 1)$ and decoupled $(X_C = 0)$ simulation. (c): $^oq_1$ EOF 2. (d): Power spectra of PC 2 for coupled $(X_C = 1)$ and decoupled $(X_C = 0)$ simulation.

1 consists of strong negative PV anomalies situated along the meandering eastward jet extension. EOF 2 consists of similar, but more zonally symmetric, negative PV anomalies along the eastward jet extension. EOF 1 also appears to show a change in strength of the subtropical gyre but these are secondary to the strong variability of the ocean eastward jet extension. Comparing the power spectra of the corresponding PCs from the decoupled simulation shows that coupling of the atmosphere to its mixed layer has a strong effect on the ocean gyre variability (see Figs. 3.6c,d). Both EOFs have increased variability across almost all low frequencies through coupling. Such changes in variability are likely a consequence of thermal feedback of the ocean with the atmosphere but it is unclear why this is so without further analysis of the lagged cross-covariability of the data (see Section 3.4).

Although it evident that these EOFs control eastward jet extension variability, it is less clear how they

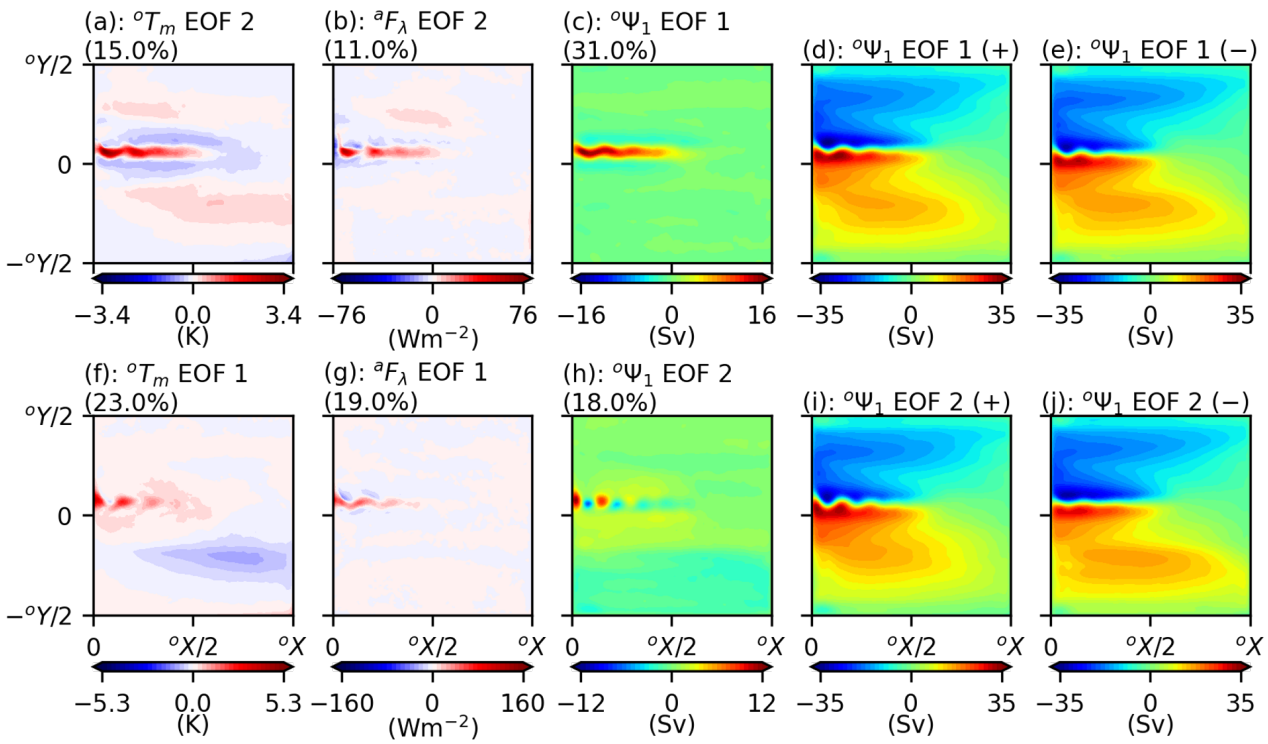

Figure 3.7: Leading EOFs of filtered upper-isopycnal ocean transport streamfunction and their phases of oscillation defined as $\pm 1\sigma$ over the mean circulation for the fully-coupled, reference modelled climate $(X_C = 1)$. Top panels represent modes associated with meridional shifts of the eastward jet extension; Bottom panels represent modes associated with changes in strength of the subtropical recirculation zone. The standard deviations σ is computed using the corresponding PC of the EOF. (a, f): $^{o}T_m$ EOFs 2 and 1, respectively. (b, g): $^{a}F_\lambda$ EOFs 2 and 1, respectively. (c, h): $^{o}\Psi_1$ EOFs 1 and 2. (d, i): Positive phases $(+1\,\sigma)$ of $^{o}\Psi_1$ EOFs 1 and 2, respectively. (e, j): Negative phases $(-1\,\sigma)$ of $^{o}\Psi_1$ EOFs 1 and 2, respectively.

affect the gyres by looking at the EOF patterns alone. In such situations it is better to overlay the EOFs onto the mean flow to show positive and negative phases of an oscillation generated by each EOF. However, we found that this was also not very insightful since the yielded PV anomaly fields still looked very similar. This is largely due to the fact that the PV anomaly fields are more homogenised throughout the ocean basin in comparison to streamfunction fields which are considerably stronger around the eastward jet extension and recirculation zones. Thus, it is more useful to look at the leading EOFs of filtered upper-isopycnal transport streamfunction which gave EOFs that were highly correlated to the EOFs obtained from the filtered upper-isopycnal PV anomaly data. Positive and negative phases are defined by a $\pm 1\sigma$ oscillation on top of the time-averaged circulation where σ represents 1 s.d. of the corresponding PC.

We found that $^{o}q_1$ EOF 1 (Fig. 3.6a) was correlated to $^{o}\Psi_1$ EOF 2 (Fig. 3.7h) with correlation

coefficient 0.85 and ${}^{o}q_1$ EOF 2 was correlated to ${}^{o}\Psi_1$ EOF 1 with correlation coefficient of also 0.85. The positive and negative phases of the upper-isopycnal ocean transport streamfunction EOFs are presented in Fig. 3.7 along with the original EOFs and explained variance fractions. From this figure, it is now apparent that ${}^{o}q_1$ EOF 1 affects the strength of the subtropical recirculation zone which coincides with a change in size of the subtropical gyre. Changes in the subpolar gyre and recirculation zone appear very small or negligible. In the positive phase, the subtropical recirculation zone strengthens, leading to an increase in jet meandering as the jet is consequently deflected more strongly equatorward as it separates from the western boundary, and the size of the subtropical gyre shrinks. In the negative phase, the opposite happens. The subtropical recirculation zone weakens, the jet is deflected less as it separates from the western boundary and the size of the subtropical gyre increases. The maximum volume transports achieved by the positive and negative phases for ${}^{o}\Psi$ EOF 1 are 70 Sv and 65 Sv, respectively, for phases at $\pm 1\,\sigma$.

On the other hand, ${}^{o}q_1$ EOF 2 (Fig. 3.6c) (or ${}^{o}\Psi_1$ EOF 1 in Fig. 3.7c) affects the meridional displacement of the eastward jet extension, with the entire jet shifting poleward in its positive phase and equatorward in its negative phase (see Figs. 3.7d,e). The magnitude of this meridional displacement appears to be ~ 100 km from its mean position and is similar to observed values (Sasaki et al., 2013). There is also a smaller but measurable change in the strength of the subtropical gyre, recirculation zones and eastward jet extension in the different phases of ${}^{o}q_1$ EOF 2 than what is observed in ${}^{o}q_1$ EOF 1. The maximum volume transports achieved by the positive and negative phases for ${}^{o}\Psi$ EOF 2 are slightly less than EOF 1 with values of 67 Sv and 63 Sv, respectively, for phases at $\pm 1\,\sigma$. Sasaki et al. (2013) also found this increase in jet-strength as the eastward jet moved poleward. These modes of variability are similar to those found in Hogg et al. (2005, 2006) and Berloff et al. (2007a) and arise due to the intrinsic variability of the ocean gyres. Our interests in subsequent sections lie in understanding how these modes of variability may couple with the overlying atmosphere through lagged responses and coupling.

3.3.2 Ocean mixed layer variability

Analysis of SST and sensible and latent heat flux variability found similar EOFs to those seen in Fig. 3.6 and are presented in Figs. 3.7a,b,f,g. These EOFs are highly correlated to the EOFs in Fig. 3.6 and are similar, but not identical, in structure to each other. The main difference being that ${}^{a}F_{\lambda}$ EOF 2 does not have the corresponding negative heat flux due to cooling of the subtropical gyre in ${}^{o}T_{m}$ EOF 2 (see Figs. 3.7f,g). This is likely an effect of damped surface heat fluxes in the ocean interior due to the white-noise integrator effect (Hasselmann, 1976; Frankignoul and Hasselmann, 1977). The top row of panels in Fig. 3.7, ${}^{o}T_{m}$ EOF 2, ${}^{a}F_{\lambda}$ EOF 2 and ${}^{o}\Psi_{1}$ EOF 1, are correlated to ${}^{o}q_{1}$ EOF 2; the bottom row of panels in Fig. 3.7, ${}^{o}T_{m}$ EOF 1, ${}^{a}F_{\lambda}$ EOF 1 and ${}^{o}\Psi_{1}$ EOF 2, are correlated to ${}^{o}q_{1}$ EOF 1. All of the respective correlation coefficients are greater than 0.8 indicating that all the EOFs correspond to the same changes in the underlying ocean gyre circulation. Similar patterns due to ${}^{o}\Psi_{1}$ EOF phase changes were found for ${}^{a}F_{\lambda}$ phase changes. It appears that in the positive phases of ${}^{a}F_{\lambda}$ EOFs 1 and 2, the total sensible and latent heat flux due to the subtropical WBCs increase by 4% and 2%, respectively. In the negative phase, the sign of the anomaly flips and the total sensible and latent heat fluxes decrease by the same amount.

3.3.3 Atmosphere and diabatic entrainment variability

The leading EOFs of the filtered atmosphere variability, namely lower- and middle-isopycnal atmosphere PV and dynamic pressures, as well as their associated diabatic entrainments are presented in Fig. 3.8. These EOFs, which are all highly correlated to each other[2], consist of a wavenumber-6[3] mode that affects the meander and zonal symmetry of the atmospheric jet with an east-west dipole anomaly sitting over the ocean basin. This mode is a synoptic scale Rossby wave that forms in the atmosphere through growing instabilities in the westerly jet. Similar modes of variability were found in Hogg et al. (2006) with a pair of EOFs identified as a travelling-wave mode pair. We also found similar modes shifted out of phase in the longitudinal direction but these were omitted since they appeared mostly unaffected by coupling of the atmosphere to its mixed layer and had significantly

[2] All correlation coefficients of corresponding PCs are > 0.75 and modes in the middle-isopycnal atmosphere have correlation coefficients > 0.9.

[3] Note that the figure trims off half of the atmosphere so the wavenumber is in fact 6.

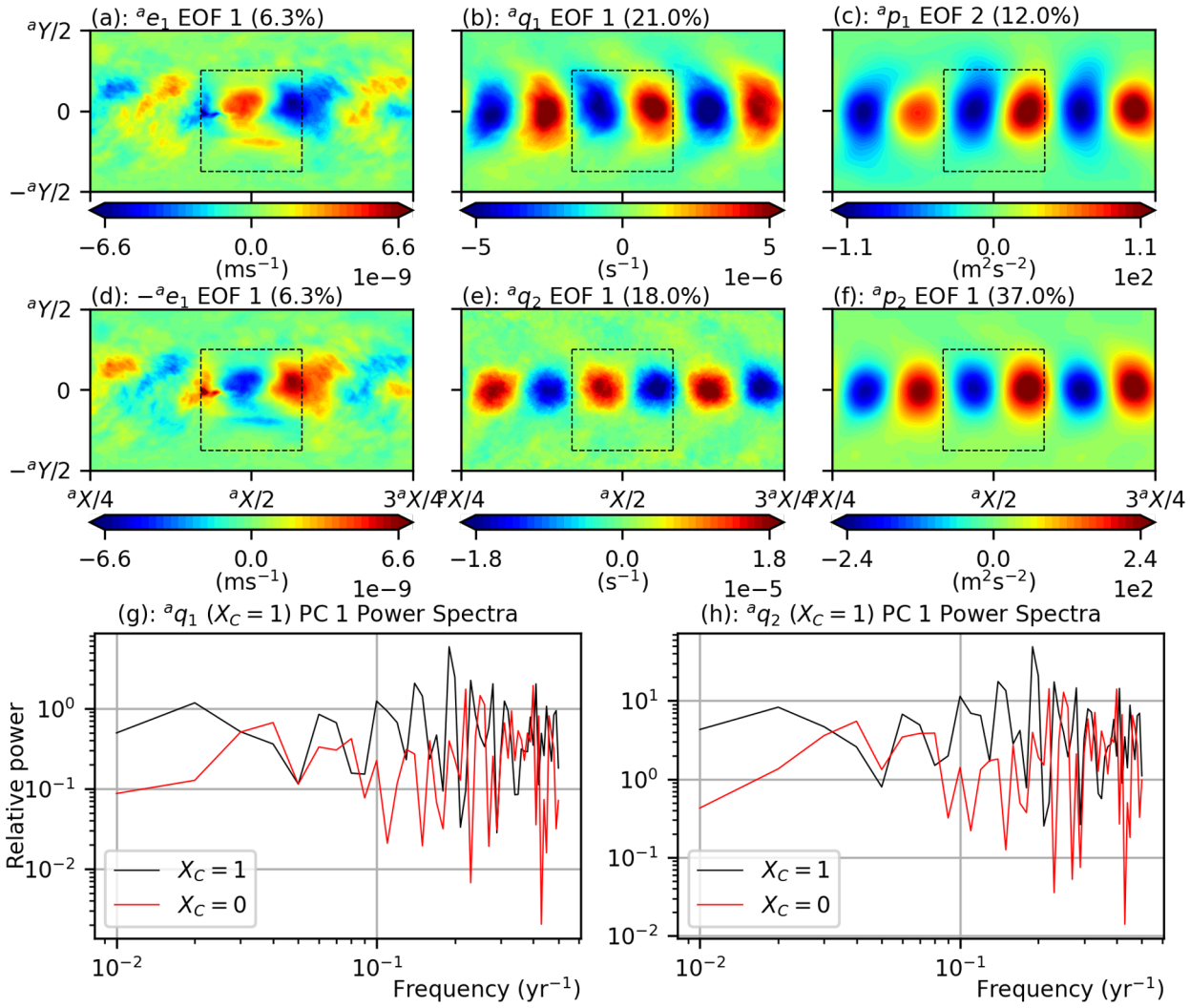

Figure 3.8: Leading EOFs of atmosphere diabatic entrainment ${}^{a}e_1$ and filtered lower- and middle-isopycnal atmosphere PV. (a): ${}^{a}e_1$ EOF 1. (b): ${}^{a}q_1$ EOF 1. (c): ${}^{a}p_1$ EOF 2. (d): $-{}^{a}e_1$ EOF 1. (e): ${}^{a}q_2$ EOF 1. (f): ${}^{a}p_2$ EOF 1. (g): Corresponding power spectra of EOF in panel (b) for coupled ($X_C = 1$) and decoupled ($X_C = 0$) simulations. (h): Corresponding power spectra of EOF in panel (e) for coupled ($X_C = 1$) and decoupled ($X_C = 0$) simulations.

lower explained variance fractions. For example, ${}^{a}q_1$ EOF 1 (Fig. 3.8b) has an explained variance fraction of 21.0% in the fully-coupled modelled climate ($X_C = 1$), but only has an explained variance fraction of 10.8% in the equivalent EOF from the partially-coupled modelled climate ($X_C = 0$). This doubling of the explained variance fraction is apparent in the power spectra of the respective PCs in Fig. 3.8g with increases in variability seen over the $5 - 16$-yr band range (increased variability over longer time-scales $>$ 20-yrs is less certain). The increase in variability of this frequency band indicates the most dominant time-scales that are likely associated with ocean-atmosphere interactions. Similar changes in explained variance fraction and power spectra were found for the corresponding

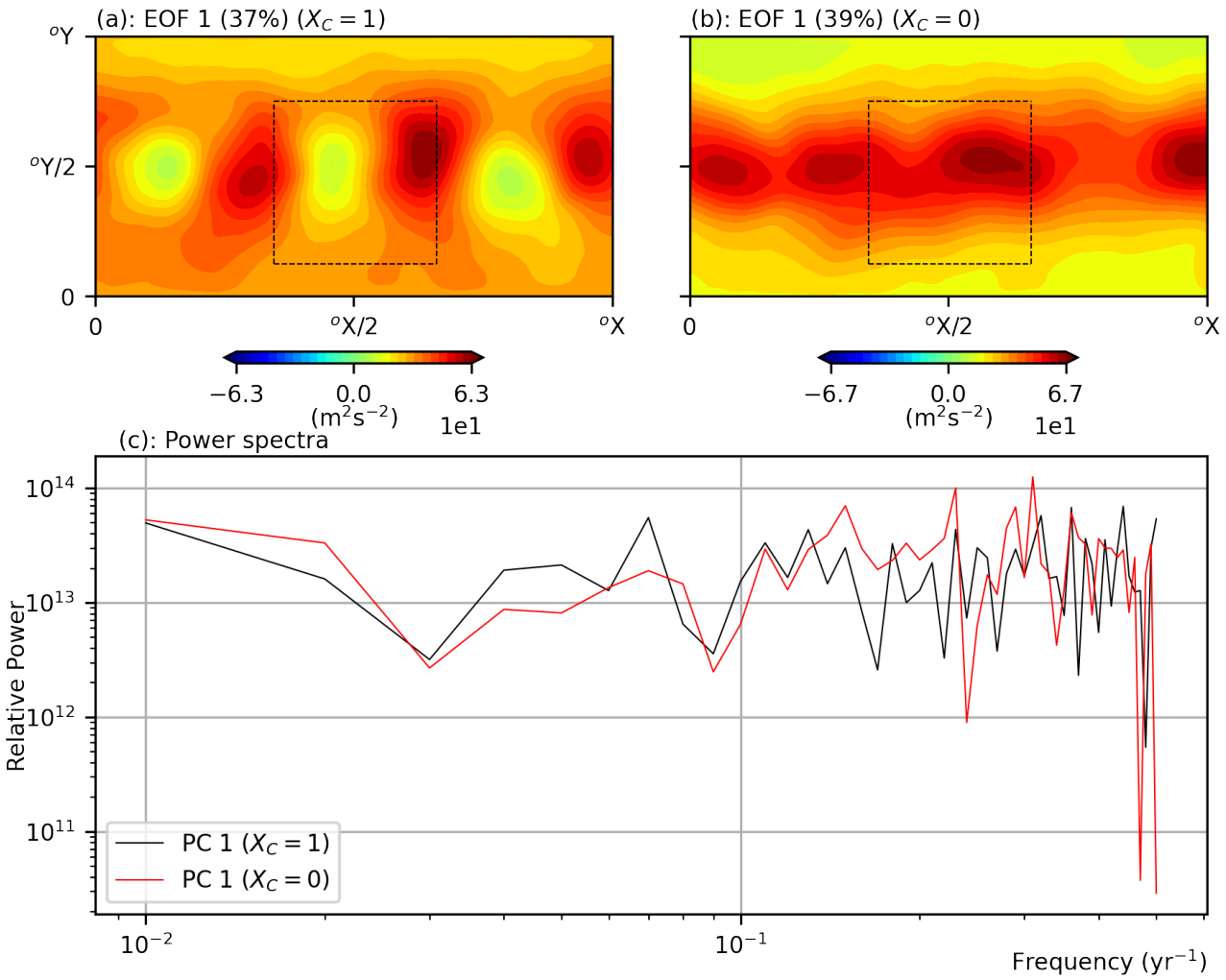

Figure 3.9: Leading EOF of filtered lower-isopycnal atmospheric dynamic pressure. (a): ${}^a p_1$ EOF 1 for benchmark modelled climate. (b): ${}^a p_1$ EOF 1 for partially-coupled modelled climate. (c): Relative power spectra of the respective PCs.

EOFs in the middle-isopycnal layer (see Fig. 3.8h) when comparing the coupled and partially-coupled modelled climates. Yet, no such change in explained variance fraction was observed for the omitted phase-shifted EOFs. The question now arises why the variability of one EOF is amplified while the other is not. It is natural to expect that the time-varying diabatic entrainment would increase the atmospheric variability of these two leading EOFs with roughly equal measure as their structures are very similar. The fact that the EOFs in Figs. 3.8b,c,e,f alone appear affected is indicative of the influence of ocean gyre dynamics on this particular mode of variability. Due to these reasons, we will treat the EOFs in Fig. 3.8 as separate EOFs from their phase-shifted counterparts.

The corresponding diabatic entrainment mode, or atmospheric forcing, that generates these modes of atmospheric variability is presented in Figs. 3.8a,d. In fact, they are the same EOF but sign-

flipped since the lower- and middle-isopycnal layers receive proportional but opposite-signed forcings (2.7). These diabatic entrainments generate the strongest circulation response in the middle-isopycnal layer, with the PV response pattern advected eastwards of the diabatic entrainment forcing by the jet before reaching maximum strength. The corresponding dynamic pressure anomalies in the middle-isopycnal layer are of the correct sign with cyclonic circulations for positive PV anomalies and anti-cyclonic circulations for negative PV anomalies. Momentum transfers into the lower-isopycnal layer via baroclinic instabilities flip the sign of the circulation anomalies in the lower-isopycnal, despite receiving forcing of the opposite sign, such that the flow becomes more barotropic. The atmosphere diabatic entrainment EOF 1 is strengthened and more coherent over the ocean basin with enhanced forcing first appearing over the western boundary near the eastward jet separation region. These then reach a maximum strength over the eastern boundary before they quickly decay. We interpret this as the generation and growth of baroclinic instabilities over the ocean basin due to land-sea contrast and strong sensible and latent heat fluxes generated by the presence of WBCs and SST front (see Figs. 3.5f,g). The decay of this mode to the east of the ocean basin is associated with strong eddy mixing of heat by turbulence of the jet that destroys the increased baroclinicity created by the land-sea contrast. This tendency of the atmosphere to reduce meridional temperature gradients and low-level baroclinicity has been posed by Hoskins and Valdes (1990). Although it is clear that the atmospheric westerly jet is interacting with the SST front and WBCs, it is unclear through this analysis alone what role the SST variability plays. In summary, the strongest mode of atmospheric variability is controlled by the growth of Rossby wave modes through baroclinic instabilities that are enhanced by the presence of the SST front.

When the low-pass filtered, lower-isopycnal atmosphere pressure variability ${}^{a}p_1$ was decomposed in our model, the leading EOF was a standing wave, meridional jet shift mode (see Fig. 3.9a) explaining a large 37.3% of the total variability. This mode is similar to the jet-shift mode found in Kravtsov and Robertson (2002); Kravtsov et al. (2003) but with weak circulation anomalies sitting in-between strong circulation anomalies. These weaker circulation anomalies are regions that are largely unaffected by the anti-cyclonic circulations and increase the zonal asymmetry of the mode. Over the ocean basin, this mode corresponds to a strong anti-cyclonic circulation anomaly over the eastern basin and a much weaker, almost stagnant, anti-cyclonic anomaly over the western basin. The differences in

structure with the equivalent EOF obtained from the partially-coupled modelled climate are notable with a more zonal structure and no such weak circulation anomalies, i.e. more similar to modes found by Kravtsov and Robertson (2002) and Kravtsov et al. (2003). Indeed the EOF in Fig. 3.9a appears similar in structure to ${}^{a}q_1$ EOF 1 in Fig. 3.8b as it is of the same wavenumber. Since ocean gyre dynamics has already been posed as the likely culprit in increasing the variability of this particular EOF, it is also likely that it is responsible for the changes in structure between Figs. 3.9a,b. Such a change in the zonal structure of an atmospheric mode of variability through coupling has yet to be seen in such models with Hogg et al. (2006); Kravtsov et al. (2007) only being able to find a modification of the preferred time-scales, rather than a change in structure of the EOF itself. In this situation, the two presented EOFs appear largely indistinguishable from each other in terms of their variability (see Fig. 3.9c).

3.3.4 Oceanic forcing variability

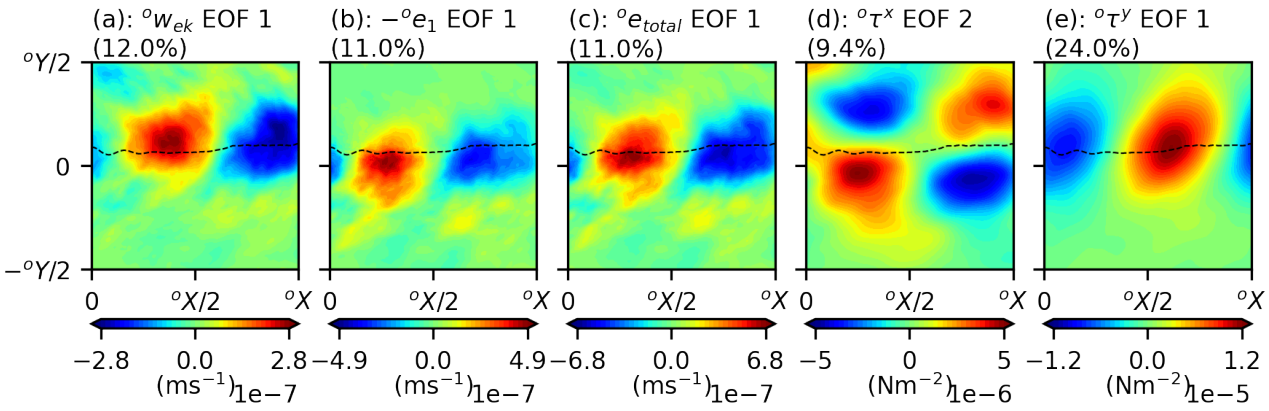

Figure 3.10: Leading EOFs of filtered ocean forcing and associated ocean surface stresses. (a): ${}^{o}w_{\mathrm{ek}}$ EOF 1. (b): ${}^{o}e_1$ EOF 1. (c): ${}^{o}e_{\mathrm{total}}$ EOF 1. (d): ${}^{o}\tau^{x}$ EOF 2. (e): ${}^{o}\tau^{y}$ EOF 1. Black dashed line indicates time-averaged position of the inter-gyre boundary. All EOFs that are plotted in this figure are highly correlated to each other.

Finally, we decompose the variability of the wind-induced ocean forcing. Namely we look at ocean Ekman pumping ${}^{o}w_{\mathrm{ek}}$, ocean diabatic entrainment ${}^{o}e_1$, and in the case of the upper-isopycnal ocean, the upper ocean total entrainment ${}^{o}e_{\mathrm{total}}$. This is left until after the atmosphere variability is decomposed as it turns out that ocean forcing variability is controlled by the atmosphere at lag-zero. The leading EOFs and their associated ocean surface stresses are presented in Fig. 3.10. Unlike the

variability of the diabatic atmosphere entrainment, which is correlated at lag-zero to the modes of lower atmosphere PV variability, ocean forcing does not correlate at lag-zero to modes of ocean gyre variability due to its large inertia. The leading EOF of the filtered ocean Ekman pumping, ocean diabatic entrainment and upper ocean total entrainment explain $11-12\%$ of the total variance (see Figs. 3.10a-c). These modes look similar and are correlated (correlation coefficients > 0.7) to the leading EOF of ${}^{a}q_1, {}^{a}q_2$ in Figs. 3.8b,e. These EOFs consist of an east-west positive-negative dipole vorticity flux over the ocean basin. The positive anomaly is situated over the eastward jet extension and the negative anomaly is situated over the eastern basin. The centroid of both anomalies shift north and south of the inter-gyre boundary depending on whether we are looking at Ekman pumping (Fig. 3.10a) or diabatic entrainment (see Fig. 3.10b)[4]. The shifting of these anomalies is due to the aforementioned misalignment of the SST front and the zero wind-curl line (see Subsection 3.2.3). The ${}^{o}e_{\text{total}}$ EOFs are advected slightly further downstream of the atmospheric westerly jet compared to the ${}^{a}q_1$ EOFs which is due to Ekman layer effects when computing surface stresses in the mixed layers (2.10). The signs of the anomalies are such that losses of PV in the lower-isopycnal atmosphere correspond to gains of PV in the ocean. However, the responsible PV flux must be generated by the middle-isopycnal atmosphere where the signs are correct, i.e. positive vorticity fluxes in the ocean must be due to positive PV anomalies that arise in the atmosphere otherwise enstrophy is not conserved. This pathway where circulation anomalies in the middle-isopycnal layer transfer momentum to the lower-isopycnal atmosphere and into the ocean is again consistent with our earlier findings (see Subsection 3.2.2). The responsible surface stress patterns (Figs. 3.10d,e) are EOF 2 of zonal surface stress ${}^{o}\tau^{x}$ and EOF 1 of meridional surface stress ${}^{o}\tau^{y}$. The wind-stress anomalies give cyclonic surface stresses for positive vorticity fluxes and anti-cyclonic surface stresses for negative vorticity flux as expected. The leading EOF of zonal wind-stress, ${}^{o}\tau^{x}$ EOF 1, consists of a zonal shear pattern (omitted). The zonal shear appears strongest over the eastern basin with the sign of the shear corresponding to a cyclonic wind-stress pattern.

Analysis of ocean forcing variability has yet to be looked at in detail using this model. This is likely because ocean gyre variability has been, so far, only explained as intrinsic modes of variability (e.g. Hogg et al., 2006) or within ocean-only simulations where the atmosphere model is switched

[4]Note that the surface stresses appear stronger in the subpolar gyre but the entrainments are pushed equatorward of the inter-gyre boundary due to the stronger subtropical WBC and recirculation zone

off (Hogg et al., 2005). However, in order to be able to understand the role of the ocean gyres within any coupled interaction, modes of atmospheric and ocean forcing variability must be related to delayed modes of ocean gyre variability[5]. Indeed, Kravtsov et al. (2007) identified monopolar Ekman pumping forcing anomalies over the ocean basin to be part of a coupled mode associated with meridional shifts of the atmosphere westerly jet preceding shifts in the ocean eastward jet extension through nonlinear adjustments of the recirculation zones (Dewar, 2003). The structures of the ocean forcing EOFs in this chapter are different since there are zonal asymmetries present which make it more difficult to diagnose the effects of these modes of atmospheric variability on the gyres. The zonal structure of these forcing modes is more similar to those discussed in Jin (1997). However, the ocean model used in their study consisted of a linear Rossby wave model which does not take into account the complex nonlinear dynamics present in the ocean gyres.

3.4 Disentangling causes of climate variability

Although we have made some progress in understanding the modelled climate variability, we still have some work to do in understanding how certain aspects of it interact. Namely, we are most interested in the ocean gyre response to forcing as well as how the associated sensible and latent heat flux anomaly affects the atmosphere diabatic entrainment. The ocean gyre response to forcing will be looked at by computing SVDs of the relevant data fields under different time-lags, with forcing leading response variables. The SVDs we need to compute are as follows:

1. Lagged SVDs of upper ocean total entrainment ${}^{o}e_{\text{total}}$ leading upper-isopycnal ocean PV anomaly ${}^{o}q_1$; diabatic ocean entrainment $+{}^{o}e_1$ leading middle-isopycnal ocean PV anomaly ${}^{o}q_2$. Lags of up to 16 yrs are looked at. Longer time-lags were found to decorrelate with known EOFs and became too noisy to interpret.

2. Lag-zero SVDs of sensible and latent heat flux ${}^{a}F_{\lambda}$ and diabatic atmosphere entrainment ${}^{a}e_1$. Time-lags are unnecessary since the atmosphere response is fast in comparison to the ocean.

[5]Conversely, modes of ocean gyre and atmospheric forcing variability may be related to modes of atmosphere variability

3. Lag-zero SVDs of diabatic atmosphere entrainment ${}^{a}e_1$ with lower- and middle-isopycnal atmosphere PV ${}^{a}q_1, {}^{a}q_2$ and dynamic pressure ${}^{a}p_1, {}^{a}p_2$. Only data over the ocean basin region was used rather than the entire channel atmosphere as is the case in Subsection 3.3.3. This is to better capture SST-induced effects on the atmosphere.

The data was also 2-yr low-pass filtered to better isolate low-frequency signals. Any extra required SVDs will be computed in-situ at the end.

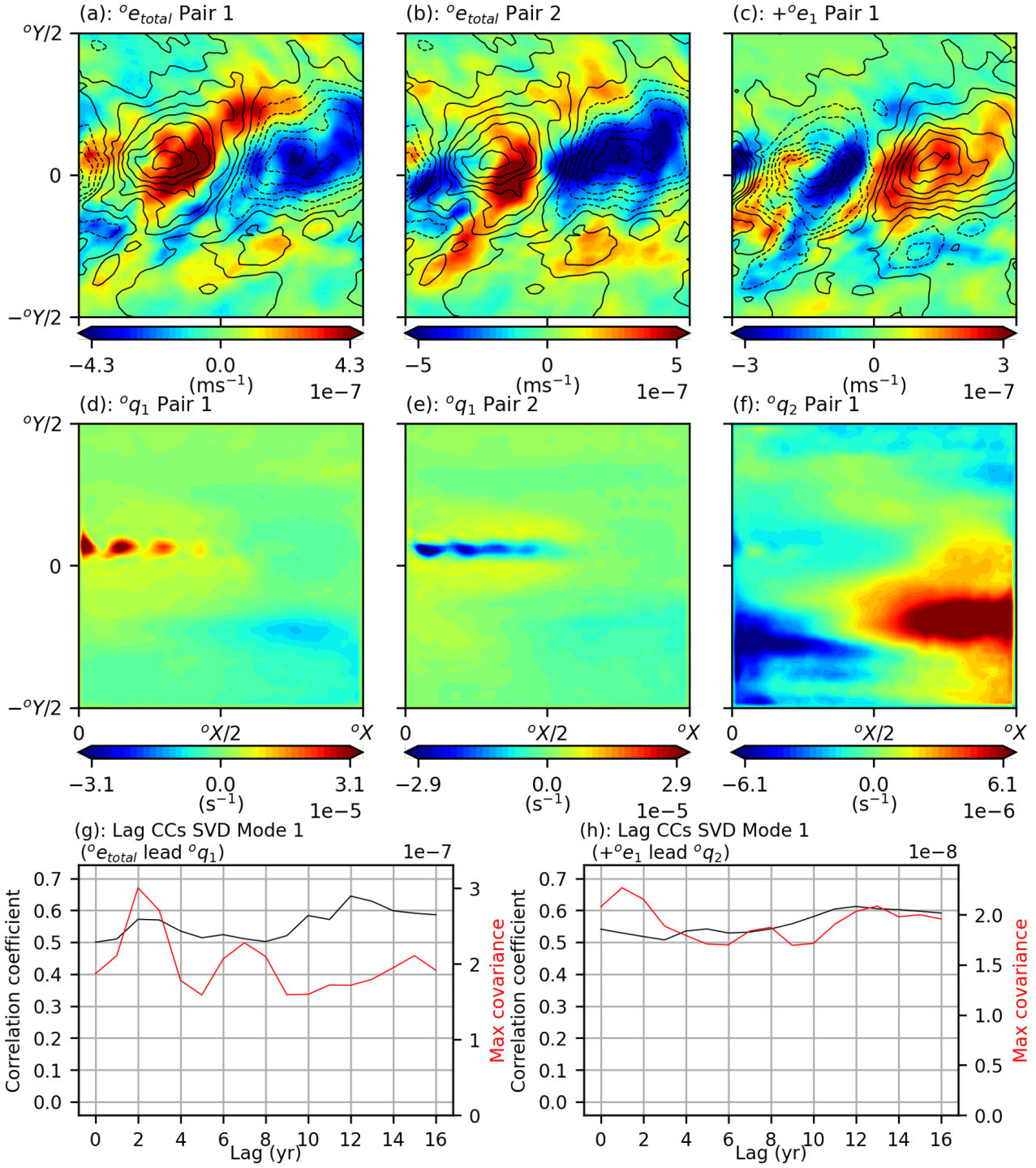

Figure 3.11: Leading SVD modes when ocean entrainment ($^oe_{\text{total}}$) leads upper-isopycnal ocean PV anomaly ($^oq_1$); diabatic ocean entrainment $+^ae_1$ leads middle-isopycnal ocean PV anomaly $^oq_2$. The two sets of SVD modes were aggregated for different time-lags by averaging over them with equal weights, i.e. computing their ensemble average. (a, d): SVD Mode Pair 1 ($^oe_{\text{total}}$ leading $^oq_1$). (b. e): SVD Mode Pair 2 ($^oe_{\text{total}}$ leading $^oq_1$). (c, f): SVD Mode Pair 1 ($^oe_{\text{total}}$ leading $^oq_2$). (g): Lag correlations and scaled covariance of leading SVD mode temporal coefficients for $^oe_{\text{total}}$ leading $^oq_1$. (h): Lag correlations and normalised covariance of leading SVD mode temporal coefficients for $+^oe_1$ leading $^oq_2$.

3.4.1 Ocean gyre response to wind-induced forcing

When the leading SVD modes were computed for upper ocean total entrainment leading upper-isopycnal ocean PV anomaly, two different leading SVD modes were found for a wide band of time-lags ranging from 0 to 16-yrs (see Figs. 3.11a,b,d,e). The two sets of SVD modes were aggregated for different time-lags by averaging over them with equal weights, i.e. computing their ensemble average. The ${}^{o}e_{\text{total}}$ components of both of these SVD modes (Figs. 3.11a,b) were found to have average correlation coefficients of 0.72 and 0.78 with ${}^{o}e_{\text{total}}$ EOF 1, respectively. Indeed both of these patterns are spatially correlated with the corresponding EOF (positive anomaly in the western basin and negative anomaly in the eastern basin) but the SVD mode appears both noisy and sheared in the anti-cyclonic direction. This shearing of the forcing pattern is either part of the noise or an important feature of the signal such as an effect of coupling[6]. Although the responsible entrainment EOF is the same for the pair of presented SVD modes, where they differ is in the upper-isopycnal PV anomaly response. In fact, the upper-isopycnal ocean gyre response of every computed leading SVD mode, except the 12-yr lag, was found to be either one of the following two responses. The first mode, shown in Fig. 3.11d, is anti-correlated to ${}^{o}q_1$ EOF 1 with a correlation coefficient of -0.96 while the second mode, shown in Fig. 3.11e, is correlated to ${}^{o}q_1$ EOF 2 with a correlation coefficient of 0.85. Both of these ocean gyre responses were found to have very low correlations with each other of < 0.25 (for any time-lags up to 16-yr lags in both directions) indicating that the responses are likely governed by distinct mechanisms.

The maximum lagged covariance explained of the computed SVD modes peaks at a $2-3$-yr lag (Fig. 3.11g) with the upper-isoypcnal ocean PV response found to be correlated to the meridional jet shift mode in Fig. 3.11. The zero-lag and 1-yr lag upper-isopycnal ocean PV response was found to be correlated to Fig. 3.11d indicating the response of the subtropical inertial recirculation zone and gyre acts at a faster time-scale. There is some uncertainty in predicting this dominant time-scale response which is likely due to high levels of ocean mesoscale turbulence. Despite a peak in maximum covariance at 2-yrs, we notice that both the lagged covariances and correlations of the temporal SVD coefficients persist for up to 16 yrs, much longer than the expected upper-isopycnal

[6]Subsection 3.4.3 will reveal that this part of the signal is likely an effect of coupling with the overlying atmospheric westerly jet.

ocean gyre response time-scale (typically less than 5-yrs, see Hogg et al., 2005; Berloff et al., 2007b; Kravtsov et al., 2007). We attribute this to likely repeated feedbacks of the ocean gyres with the atmosphere. In addition, the sign of the response always remains consistent, with either a weakening or a poleward shift of the eastward jet detected for this particular forcing pattern implying a positive feedback signal.

For the middle-isopycnal ocean, the PV anomaly response largely consists of ${}^{o}q_2$ EOF 1 activated by the diabatic component of the upper-isopycnal ocean forcing which is given by $+{}^{o}e_1$ EOF 1. The PV response is contained within the subtropical gyre as this is where diabatic entrainment dominates (see Figs. 3.3g, 3.10b,g). The average correlations are 0.64 for ${}^{o}e_1$ EOF 1 and 0.99 for ${}^{o}q_2$ EOF 1. Note the sign change in vorticity fluxes is consistent with the forcing in the upper-isopycnal layer. The middle-isopycnal ocean PV response shows a negative PV anomaly protruding out from the western boundary extending out into the ocean basin and a similar positive PV anomaly extending out from the eastern boundary. This pattern was found to be correlated to the upper-isopycnal subtropical recirculation zone weakening in the upper-isopycnal layer (Fig. 3.11d). By checking the streamfunction response in the middle-isopycnal layer, the western and eastern circulation anomalies correspond to cyclonic and anti-cyclonic anomalies, respectively. Such a circulation response in the middle-isopycnal layer hence implies that these circulation anomalies do not arise as a result of diabatic entrainment forcing in the middle-isopycnal layer, but must be due to momentum transfers from the upper-isopycnal layer due to changes in the subtropical gyre circulation. The middle-isopycnal layer response to meridional shifts of the eastward jet were not detected when looking at PV anomalies but were detected for transport streamfunction responses. The pattern of the response was similar to Fig. 3.11e and also occur due to momentum transfers from the upper-isopycnal layer. The time-scale of the middle-isopycnal ocean PV response is less clear than the upper-isopycnal (see Fig. 3.11). There appears to be a small peak in maximum covariance at the 1-yr lag, perhaps associated with a fast barotropic response along the eastward jet extension (e.g. Dewar, 2003), but this peak is not much greater than the other values of computed maximum covariances and unlikely to be statistically significant (see Fig. 3.11).

In summary, the east-west positive-negative upper ocean total entrainment mode induces a weakening of the subtropical recirculation zone and/or a poleward shift of the eastward jet extension in the upper-

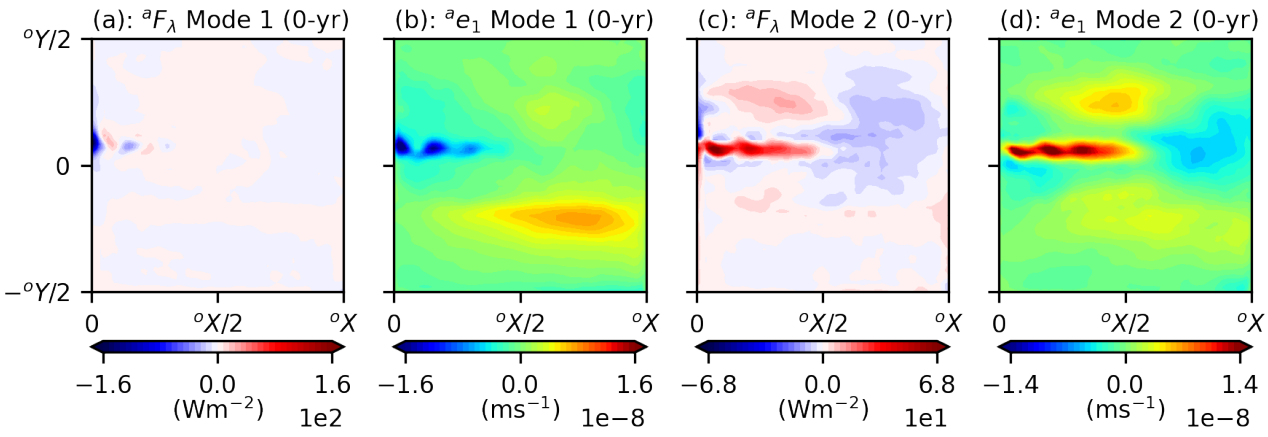

Figure 3.12: Leading lag-zero SVD modes of sensible and latent heat flux and diabatic atmosphere entrainment at lag-zero in the lower-isopycnal atmosphere. (a, b): SVD mode 1 with ${}^{a}F_{\lambda}$ mode presented in (a) and ${}^{a}e_{1}$ mode presented in (b). (c, d): SVD mode 2 with ${}^{a}F_{\lambda}$ mode presented in (c) and ${}^{a}e_{1}$ mode presented in (d).

isopycnal layer. The middle-isopycnal layer response seems largely to be controlled by momentum transfers that occur due to baroclinic instabilities through the much stronger upper-isopycnal circulation response. Furthermore, the ocean does not appear to respond at any preferred time-scale and instead acts over a wider interannual through to decadal band time-scale. This is likely due to reduced predictability of the model induced by high levels of ocean mesoscale turbulence (Nonaka et al., 2016). The east-west dipole forcing mode is difficult to compare to most studies of wind-induced ocean gyre variability which mostly focus on monopole forcings (e.g. Dewar, 2003; Kravtsov et al., 2007). Both the ocean forcing and response modes are complex in nature and further analysis of the processes involved is required. Since the forcing mode may be split into two separate anomalies, one in the western and the other in the eastern basin, we hypothesise that the two uncorrelated ocean gyre responses are a result of two distinct mechanisms responding independently to the two ocean forcing anomalies. Further dynamical interpretation of this ocean gyre response is outside the scope of this chapter and we leave this to Chapter 4. Instead, we focus our attention on the associated SST response and how this affects the atmospheric circulation.

3.4.2 SST-induced atmosphere diabatic entrainment

As the ocean gyre responses in the previous subsection induce changes in the shape and location of the ocean eastward jet, it is natural to check how the associated SST front changes affect the

atmospheric circulation. Since we know the associated sensible and latent heat flux response to the discussed modes of ocean gyre variability (see Fig. 3.7), we would now like to see what atmosphere diabatic entrainments are associated with them. Fig. 3.12 shows the sensible and latent heat fluxes and the consequently generated atmosphere diabatic entrainments over the ocean basin. The polarities of these SVD modes correspond to the aforementioned, wind-induced changes in the ocean gyre circulation. We have only computed these SVDs using atmosphere diabatic entrainment data over the ocean basin region where the effect of sensible and latent heat fluxes is strongest. Only the positive atmosphere diabatic entrainment situated over the eastern subtropical gyre is unaccounted for by the sensible and latent heat fluxes, but it is present in the associated SST EOF (see Fig. 3.7f). Since the associated SST anomaly is weak in comparison to the anomaly near the SST front, the SVD analysis may have lacked the sensitivity to pick up this part of the signal. The ${}^{a}F_{\lambda}$ modes in Figs. 3.12a,c are highly correlated to ${}^{a}F_{\lambda}$ EOFs 1 and 2 with correlation coefficients 0.9 and 0.73, respectively. The ${}^{a}e_{1}$ modes in Figs. 3.12b,d are correlated to ${}^{a}e_{1}$ EOFs 3 and 1 with correlation coefficients of 0.87 and 0.64, respectively. The temporal coefficients of the SVD mode 1 and 2 themselves are also correlated highly with coefficients of 0.85 and 0.85, respectively.

The leading SVD mode pair of ${}^{a}F_{\lambda}$ and ${}^{a}e_{1}$ (Figs. 3.12a,b) is associated with the weakening of the subtropical recirculation zone and the expansion of the same gyre. The negative sensible and latent heat flux anomaly is associated with a deformation of the recirculation zone and a change in the shape of the eastward jet extension and SST fronts, while the positive heat flux anomaly is associated with a warming of the eastern subtropical gyre as it expands. On the other hand, the second SVD mode pair (Figs. 3.12c,d) is dominated by strong, positive sensible and latent heat fluxes over the SST front as the eastward jet shifts poleward of its average position. This heat flux generates a strong diabatic entrainment anomaly over the same region with a strong diabatic entrainment response of similar meridional scale in the form of an anomalous line source of vorticity (the sign of this depends on whether we are looking at the lower- or middle-isopycnal layer). Although there does appear to be some mixing of this temperature anomaly in the atmospheric mixed layer, the narrow meridional scale of diabatic entrainment is maintained well. This is likely due to the influence of meridional eddy heat fluxes that are anchored to the location of the SST front (Fig. 3.5g). In Fig. 3.12c, the surface heat flux forcing is such that there is a very weak, east-west positive-negative sensible and latent heat flux

dipole over the ocean basin. This is then advected eastwards roughly across quarter of an ocean basin width to produce the entrainment pattern in Fig. 3.12d. This eastward advection by the atmosphere westerly jet is similar to what we observed with the same observed atmosphere diabatic entrainment patterns driving the atmosphere (see Fig. 3.8).

3.4.3 Inertial response of westerly jet to diabatic entrainment forcing over SST front

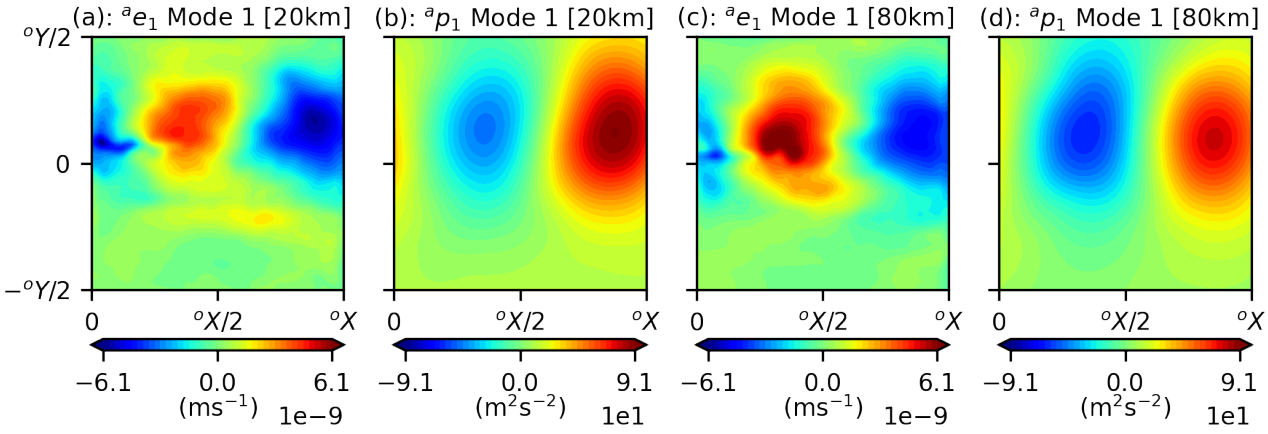

Figure 3.13: Leading lag-zero SVD modes of atmosphere diabatic entrainment and lower-isopycnal atmosphere dynamic pressure anomaly at lag-zero. Left-hand side panels show the SVD modes for 20 km atmosphere while right-hand side panels show the SVD modes for 80 km atmosphere.

Next, we look at the response of the atmosphere to diabatic entrainments. Although we have already correlated EOFs of these fields to each other in Subsection 3.3.3, we now isolate impacts of SST variability on the atmosphere by spatially subsampling over the ocean basin. This will allow us to better determine the atmospheric response to the line source of vorticity identified in the previous paragraph. To do this, we computed lag-zero SVDs of atmosphere diabatic entrainment ${}^{a}e_1$ and atmosphere PV ${}^{a}q_1, {}^{a}q_2$. Similar SVDs with entrainment and dynamic pressure anomalies ${}^{a}p_1, {}^{a}p_2$ are also computed to see the inertial effects on the atmospheric jet. In the case that influence of SST variability on the atmosphere is small or negligible, we would expect to see the computed SVDs will be similar or identical to the EOFs shown in Fig. 3.8, i.e. no difference in atmosphere response when subsampling data over the ocean basin. In addition, to ascertain any impact of atmospheric eddies on the response to diabatic entrainments, we also computed a supplementary coupled climate with

a moderately reduced atmospheric resolution of 80 km (see Table A.1 in Appendix A.1). The ocean model parameters are identical to the benchmark modelled climate. The same sets of analysis was performed using data obtained from this supplementary modelled climate.

The leading SVD modes for the 20 km and 80 km lower-isopycnal atmosphere dynamic pressure responses to diabatic entrainments correlated to ${}^{a}e_1$ EOF 1 are presented in Fig. 3.13. Firstly, the atmosphere diabatic entrainment modes (Figs. 3.13a,c) are highly correlated to equivalent EOFs to the one shown in Fig. 3.8a with correlation coefficients > 0.9. The positive anomaly in Fig. 3.13c appears strengthened by the line source of vorticity in Fig. 3.12d. We already know that this mode of diabatic entrainment, in the benchmark modelled climate, is well correlated to meridional shifts of the SST front and eastward jet extension (e.g. Figs. 3.12c,d). We found that the structures of the modes for the corresponding PV responses in both atmospheric resolutions were similar to those already shown in Fig. 3.8, so they are omitted, i.e. the SST variability does not significantly alter the structure of the PV response in the atmosphere, although it affects its variability (see Figs. 3.8g,h). However, we found that the dynamic pressure or inertial response of the 20 km atmosphere to this diabatic entrainment was significantly different in structure to the EOFs shown in Fig. 3.8. In particular, the lower-isopycnal pressure response shows an asymmetry in the strength of the anomalous response over the western and eastern basins[7]. Over the western basin, there is a weaker cyclonic anomaly, while over the western basin, there is a stronger anti-cyclonic anomaly. This is in contrast to the EOFs in Figs. 3.8c,f which are computed over the entire atmosphere. The EOFs computed in Fig. 3.8 do not show this asymmetry in response of the westerly jet to diabatic entrainments because ocean-atmosphere interactions are given less importance, in a statistical sense, as the variability of the entire atmosphere is being considered.

Reduction of the atmosphere model resolution, and a consequent damping in eddy-induced behaviours, leads to a reduction in this asymmetric response (Fig. 3.13d), with the lower-isopycnal pressure response correlated to EOFs of the same structure as those in Fig. 3.8. On the other hand, the asymmetric inertial response of the 20 km westerly jet (Fig. 3.13b) appears to be occur as a result of SST variability on the atmospheric westerly jet with the inertial response now correlated to both ${}^{a}p_1$ EOF

[7]There was also a similar, but weaker, inertial asymmetry in the middle-isopycnal atmosphere but since this westerly jet in this atmosphere has much a much larger momentum it is deflected less than the lower-isopycnal westerly jet.

1 and 2 with correlation coefficients 0.70 and 0.62, respectively. Note that the correlation to ${}^{a}p_1$ EOF 1 was undetectable in the EOF analysis in Subsection 3.3.3. This atmospheric response is akin to those seen in Famooss Paolini et al. (2022) with the atmospheric jet deflected homo-directional to the front immediately downstream. Furthermore, for poleward shifts of the eastward jet extension, the atmospheric westerly jet experiences acceleration at higher latitudes and deceleration at lower latitudes which may have influences on atmospheric blocking (Famooss Paolini et al., 2022). The opposite may be seen for equatorward shifts of the eastward jet. Indeed, this ocean feedback is so strong that it likely leads to the reduced zonal structure of the atmospheric westerly jet meridional shift mode seen in Figs. 3.9 which has a similar spatial structure to Fig. 3.13b. The structure of the pressure response may also explain the zonally sheared ocean forcing patterns observed in Figs. 3.11a-c. Although the inertial response of the jet shows significant differences to Fig. 3.8, the PV response was found to be largely the same. In short, the SST anomaly associated with meridional shifts of the eastward jet extension creates positive feedbacks with downstream anchoring of the westerly jet (Figs. 3.11b,e).

We found that ${}^{a}e_1$ EOF 3 (Fig. 3.12d), or changes in strength of the subtropical recirculation zone, did not appear to strongly invoke modes of atmosphere variability despite spatial subsampling over the ocean basin region. We found some evidence of coupling to the westerly jet meridional shift modes in Fig. 3.9 but correlation of any computed SVD modes to this EOF was low (~ 0.4) so these modes were omitted. This does not necessarily mean that this SST anomaly has no measured effect on the atmospheric circulation, but rather, the response of the atmosphere to this particular anomaly is likely more strongly controlled by eddy-mean flow feedbacks, i.e., the response of the atmosphere to this SST anomaly is likely more dependent on the background flow state and is hence nonlinearly related to the strength and sign of the SST anomaly.

Finally, to better understand why improved resolution of atmospheric eddies increases the asymmetry in the strength of the lower-isopycnal atmospheric pressure response, we compare the meridional eddy heat fluxes of the 20 km and 80 km atmospheres that are conditionally time-averaged over years where the eastward jet extension is in its poleward and equatorward states, i.e. greater than or less than $\pm 1\sigma$ of their measured mode variabilities. These meridional eddy heat fluxes, and their difference between the poleward and equatorward ocean eastward jet states are shown in Fig. 3.14. Reduction of the atmospheric resolution to 80 km severely inhibits the atmosphere's ability to resolve the underlying

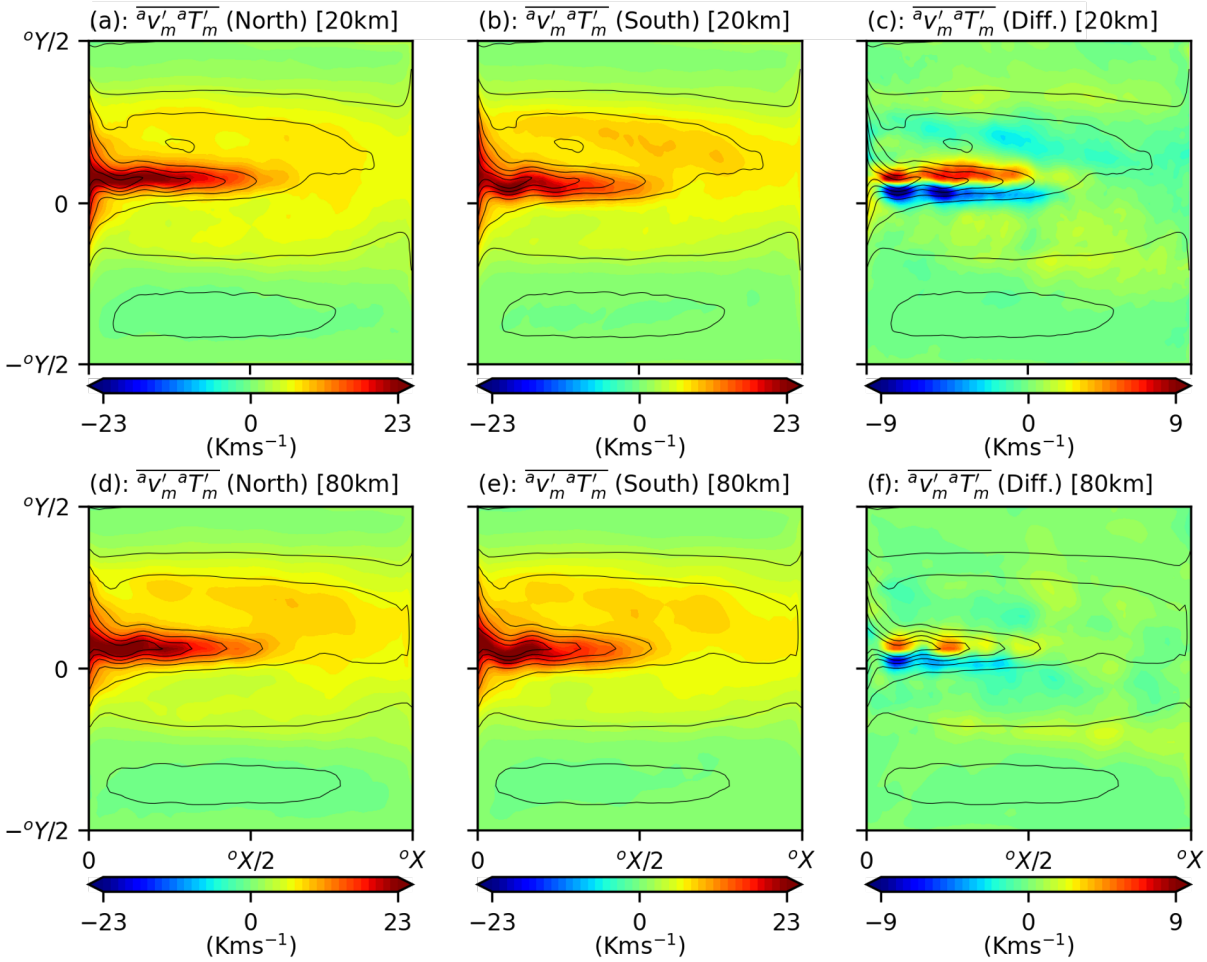

Figure 3.14: Conditionally time-averaged meridional eddy heat fluxes over years for ocean eastward jet extension in poleward and equatorward positions. Top panels show fluxes for a 20 km atmosphere while bottom panels show fluxes for a 80 km atmosphere. (a, d): Conditionally time-averaged meridional eddy heat fluxes for eastward jet extension in poleward position. (b, e) Conditionally time-averaged meridional eddy heat fluxes for eastward jet extension in equatorward position. (c, f): Anomalous heat flux between the poleward and equatorward states. The black contours show the time-averaged meridional heat flux profile over the entire simulation period.

meridional shifts in the SST front (see Figs. 3.14c,f) despite the time-averaged state itself being fairly well resolved. The anomalous fluxes between the poleward and equatorward states of the SST front are smaller in both magnitude and zonal extent, i.e., the meridional eddy heat flux profiles for the ocean eastward jet in the poleward and equatorward states are almost identical for the 80 km atmosphere. Since the ocean circulation is almost identical with the nominal 5 km resolution maintained in both climates, this difference is attributed, in part, to the lack of the atmospheric eddies' ability to resolve the small meridional scales associated with shifts in the SST front. Indeed, the magnitude of the meridional shift between the two states is around 200 km which is poorly resolved by the 80 km

atmosphere. Consequently for the 80 km atmosphere, this leads to a $70-80\%$ reduction in strength of the anomalous line source of heat flux and vorticity patterns in Figs. 3.12c,d. Around half of this reduction in strength is due to a corresponding weaker SST anomaly which is likely due to damped positive feedbacks in the 80 km atmosphere climate. The other half of the reduction is unaccounted for and is likely due to inhibited atmospheric eddies. The correlation of the associated temporal SVD coefficients also drops from 0.85 in the 20 km atmosphere to 0.59 in the 80 km atmosphere. This difference in strength of the anomalous line source of vorticity likely explains the two different inertial responses of the atmospheric jet with the increased zonal asymmetry acting as a proxy for the atmosphere's sensitivity to underlying shifts of the SST front. Indeed, if the SST front was fixed in its meridional position, which is similar to the response of the 80 km atmosphere, we would expect to see pressure anomalies of similar strength over the western and eastern ocean basin. In addition, the reduction in correlation between the surface heat flux anomaly and associated westerly jet response is indicative of a stronger dependence on the background flow state (Peng et al., 1997; Peng and Whitaker, 1999).

3.4.4 Summary of ocean gyre influences on the climate variability

Our analysis has revealed the following positive feedback mechanism for enhanced low-frequency climate variability:

1. East-west positive-negative PV anomalies arise in the middle-isopycnal atmosphere over the ocean basin as part of a wavenumber-6 Rossby wave disturbance.

2. This propagates into the lower-isopycnal atmosphere via baroclinic instabilities and surface stresses generate positive and negative vorticity fluxes over the western and eastern ocean basins, respectively. The growth of baroclinic instabilities is significantly strengthened over the ocean basin due to the presence of the SST front.

3. The ocean gyres respond through a weakening of the subtropical recirculation zone and a poleward meridional shift of the eastward jet extension. Full dynamical interpretation of this ocean

gyre response may be seen in Chapter 4, but preliminary analysis indicates that these two responses are governed by distinct mechanisms.

4. SST anomalies are generated as a consequence of shifts in the inter-gyre boundary and deformations of the eastward jet extension. This then leads to sensible and latent heat flux anomalies that generate strong diabatic entrainment anomalies in the atmosphere. The sensitivity of the atmosphere to underlying SST front shifts is highly dependent on resolution.

5. The diabatic entrainments trigger baroclinic instabilities that grow downstream of the westerly jet and eventually lead to a strong barotropic circulation over the eastern basin. This atmospheric response is shown to be modified by eddies and dependent on the atmosphere's ability to resolve meridional scales associated with the SST front shift.

6. This atmosphere response then reinvigorates the PV variability and generates a positive feedback onto the gyres.

3.5 Discussion

Although the model we have used in this chapter is highly idealised, e.g. lack of moisture, overturning circulation, vertical motions, seasonality combined with a simple model geometry, proper capturing of complex eddy dynamics in the ocean and atmosphere have revealed relevant coupled interactions (e.g. Famooss Paolini et al., 2022) that enhance the low-frequency variability. We believe these modes play an important role in understanding the midlatitude climate and that this study opens up more avenues of future work.

This chapter focused on the effects of ocean-atmosphere coupling on the modelled climate and established the anatomy of the low-frequency climate variability. EOF analysis of the 2-yr low-pass filtered, atmosphere PV variability showed two wavenumber-6 Rossby wave modes shifted out of phase in the longitudinal direction. These EOFs consisted of patterns with alternating-signed circulation anomalies, similar to those found in Hogg et al. (2006). Despite these EOFs appearing at first to form a travelling-wave pair, the disparity in the total explained variance fraction in temporal

behaviour meant that the EOFs should be treated separately. The difference in explained variances was found to be due to the competition between ocean-atmosphere coupling strength and land-sea contrast. Coupling the atmosphere to its mixed layer doubled the variance of one EOF in particular, indicating stronger coupling of this EOF with the ocean gyres. Ocean gyre coupling with the atmosphere also likely leads to the reduced zonal structure of the atmospheric jet meridional shift pattern in the benchmark modelled climate which may have influences on atmospheric blocking strength (Famooss Paolini et al., 2022). Previously, only time-scale modifications of atmospheric modes have been deemed possible (e.g. Hogg et al., 2006; Kravtsov et al., 2007) so this finding is, to our knowledge, new and important. The corresponding diabatic entrainment mode that was correlated to the standing Rossby wave mode was found to be strongest over the ocean basin. This is also where baroclinic instabilities grow fastest due to the sharpening of meridional AST gradients via eddy heat fluxes.

EOF analysis of the filtered, upper-isopycnal ocean PV variability data showed the two leading EOFs consisted of changes in strength of the subtropical inertial recirculation zone and meridional displacements of the ocean eastward jet extension. These EOFs were both found to be strengthened by coupling over the entire low-frequency spectrum. Such modes of variability have been seen frequently in QG models (e.g. Hogg et al., 2005; Berloff et al., 2007a) as they appear from the intrinsic low-frequency variability of the ocean gyres.

The ocean was found to respond in two possible ways to east-west positive-negative dipole forcing over the basin: 1) weakening of the subtropical recirculation zone and shrinking of the respective gyre at a relatively fast $0-1$-yr response time-scale; 2) a poleward meridional shift of the eastward jet extension at a relatively slow $2-3$-yr response time-scale. However, the estimation of this response is uncertain with the associated correlation coefficients remaining at fairly similar levels over the entire range of computed time-lags. This is likely due to high levels of mesoscale turbulence that reduce ocean gyre predictability (Nonaka et al., 2016) and repeated positive feedbacks present in the modelled climate. The sensible and latent heat flux response associated with the meridional shift of the eastward jet generated atmosphere diabatic forcings that reinforced the initial dipole forcing, and thus, reinvigorate the ocean gyre modes. Again, this is consistent with our findings of increased, broadband ocean gyre variability through coupling. The nature of this positive feedback between the ocean and

atmosphere bears some resemblance to the interannual coupled interaction found by Goodman and Marshall (1999), Kravtsov et al. (2006) and Farneti (2007). This coupled interaction involves the westward propagation of coupled Rossby waves and enhanced interannual variability due to positive feedbacks. The time-scale of this interaction is found to be controlled by the basin crossing time of the ocean baroclinic Rossby wave. The coupled interaction in our model appears similar, with an initial ocean gyre response time-scale of $2-3$-yrs which may be due to wave propagation, but positive feedbacks persist for up to much longer interdecadal time-scales. In addition, the atmospheric mode of the coupled interaction in our model appears to be a standing wave Rossby wave mode, rather than a phase-locked wave seen by Goodman and Marshall (1999); Kravtsov et al. (2006); Farneti (2007).

The asymmetry in the atmosphere response, where the westerly jet is displaced less over the western basin and more over the eastern basin, is strongest in the lower-isopycnal layer due to the reduced momentum of the lower-isopycnal jet. The final pressure anomaly in the lower-isopycnal atmosphere is a barotropic circulation anomaly over the eastern basin. This asymmetry in the response is so much so that the lower-isopycnal pressure response is now also correlated to the modified westerly jet meridional shift mode. This mode was only detected after computing SVDs using data subsampled over the ocean basin region only, rather than the entire atmosphere. The structure of this westerly jet meridional shift EOF is different in structure to modes seen in Kravtsov et al. (2007) because it is less zonally symmetric.

The response of the atmosphere to meridional shifts in the SST front was also found to be dependent on the atmospheric resolution. For resolutions where the meridional scale of the shift is well-resolved, shifts in the low-level baroclinicity translate to a weaker inertial deflection of the jet over the SST front and a stronger inertial deflection of the jet downstream. The asymmetric inertial deflection of the jet is likely due to the eddy-induced, line source of vorticity generated by the SST front shift. When the meridional scale of the SST front shift is poorly resolved, it is now unable to detect the changes in the low-level baroclinicity as well, so although a entrainment mode still exists, this mode is no longer controlled by meridional shifts of the eastward jet extension and the anomalous line source of vorticity is significantly weakened. Note that although the diabatic entrainment is still strengthened by the presence of the SST front which restores the low-level baroclinicity, the control of the variability is now handed over to the atmosphere, likely through a stronger dependence of the atmospheric response

to the background flow state. This lack of atmospheric sensitivity to meridional shifts in the SST front at 80 km resolution may be a contributing factor to why previous studies using this model struggled to capture many of these feedbacks of SST variability on the atmosphere (Hogg et al., 2006).

Although this chapter has revealed the anatomy of delayed, wind-induced ocean gyre variability, we are yet to show the ocean processes driving the ocean gyre modes. We have proposed that certain patterns of ocean forcing activate modes of ocean gyre variability but exactly how they do this is still unclear and further analysis of the underlying dynamics is required. To do this, the next chapter will require a series of ocean-only simulations run under fixed wind-stresses and thermal forcings to determine whether we are able to reproduce the effects of ocean entrainment observed in the coupled model. An analysis of ocean PV budgets will also be required to quantify the sources and sinks of PV within each of the gyres (see Chapter 4).

Parts of this chapter have been taken from Kurashina and Berloff (2022a), all of which is original work that has been conducted by the author.

Chapter 4

Coupling of the wind-driven ocean gyres to jet streams: Mechanisms

4.1 Introduction

In the previous chapter, we decomposed the anatomy of the modelled climate variability. This chapter will now look at the mechanisms that are responsible for governing the observed, wind-induced ocean gyre responses. We will start by giving a brief recap of the important results from the previous chapter which are necessary for subsequent analysis.

4.2 Recap of wind-induced ocean PV variability from Chapter 3

The 2-yr low-pass filtered upper-isopycnal ocean PV variability was found to be dominated by two statistically independent modes or EOFs. These modes were also not found to form travelling wave-like behaviours and showed a lack of correlation at any time-lag. The first mode involved changes in strength of the subtropical recirculation zone, as well as changes in size of the respective gyre, while the second mode involved meridional shifts of the eastward jet extension. The low-pass filtered atmosphere PV variability was found to be dominated by two wavenumber-6 modes with one of

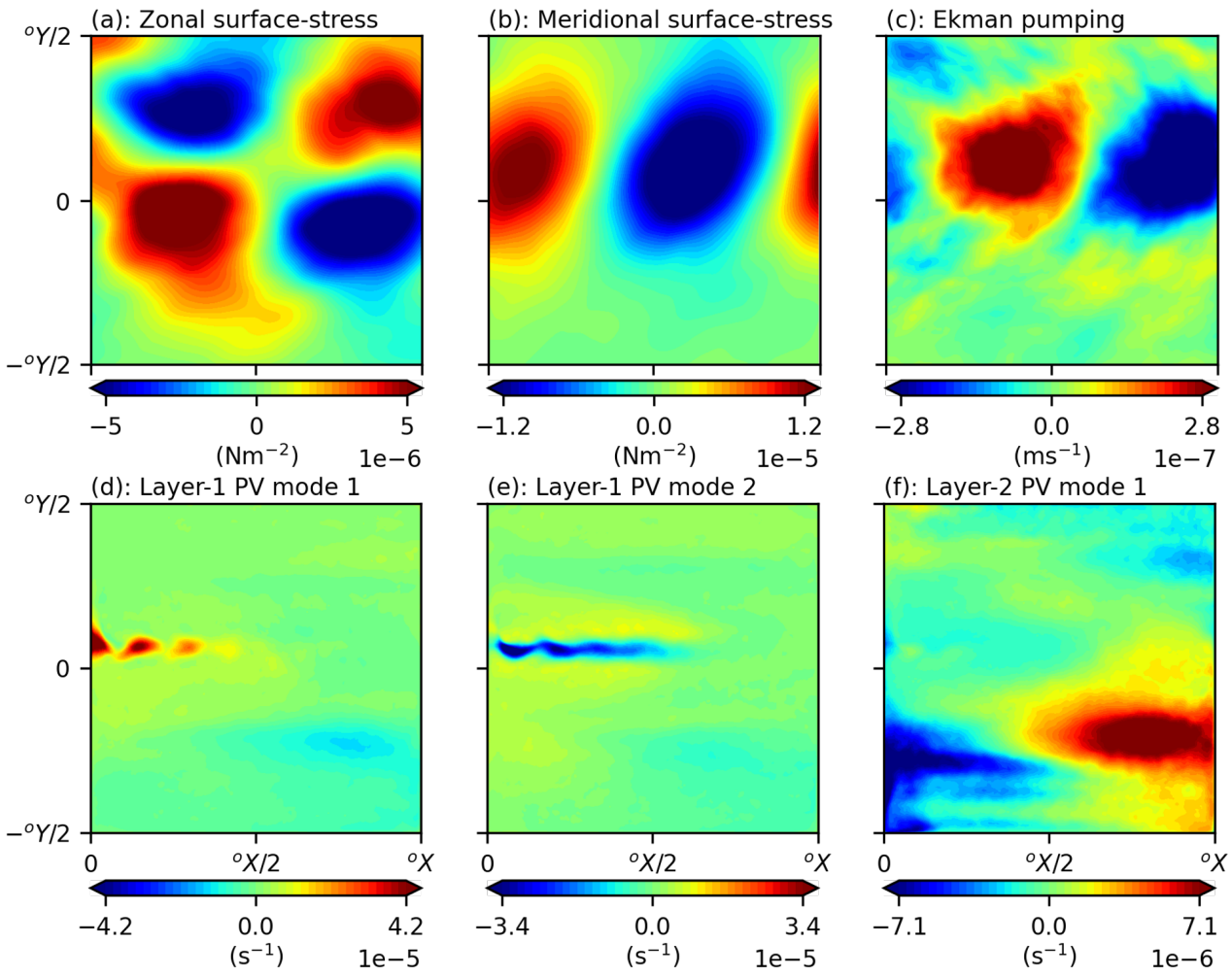

Figure 4.1: Delayed modes of ocean gyre variability induced by east-west dipole ocean forcing as well as their correlated wind-stress fields. These modes persist for lags of up to 16 yrs so we have averaged over them to create an aggregated mode. Modes obtained from analysis in Chapter 3. (a): Zonal ocean surface-stress anomaly. (b): Meridional ocean surface-stress anomaly. (c): Ocean Ekman pumping. (d): Upper-isopycnal ocean PV response mode 1. (e): Upper-isopycnal ocean PV response mode 2. (f): Middle-isopycnal ocean PV response.

these modes coupling strongly with the ocean gyre dynamics. These modes of the atmosphere were found to transfer momentum into the lower atmosphere through relatively fast events of baroclinic instabilities. Momentum is then transferred into the ocean through wind-stress anomalies that arise through frictional effects.

Modes of covariability between wind-induced ocean forcing and the ocean gyre response were found through SVDs. The ocean and atmosphere modes associated with one phase, or polarity, of this wind-induced ocean gyre variability are presented in Fig. 4.1 and involve the aforementioned modes of low-pass filtered ocean and atmosphere PV variability. Figs. 4.1a,b show the wind-stress modes generated

by the atmosphere PV variability, with cyclonic wind-stresses over the western ocean basin and anti-cyclonic wind-stresses over the eastern ocean basin. This then results in east-west dipole wind-stress curl anomalies in the upper-isopycnal ocean (Fig. 4.1c), with a corresponding weaker and opposite-signed diabatic entrainment forcing in the middle-isopycnal ocean (omitted, see previous chapter).

Two responses were found in the upper-isopycnal ocean gyres to this forcing. The first was a weakening of the negative PV-signed subtropical recirculation zone (Fig. 4.1d); the second response of the ocean gyres was a poleward meridional shift of the eastward jet extension (Fig. 4.1e).

The middle-isopycnal ocean PV response was found to be contained within the subtropical gyre where diabatic entrainment dominates. This response involved the PV redistribution of vorticity flux anomalies in the subtropical gyre with a negative-signed PV anomaly protruding from the western boundary and a positive-signed PV anomaly protruding from the eastern basin (Fig. 4.1f). This mode was found to be correlated to the upper-isopycnal PV response in Fig. 4.1d. A similar barotropic, middle-isopycnal response for Fig. 4.1e was found when checking the streamfunction response to the same mode of ocean forcing.

Although a robust statistical link was established between these modes of ocean forcing and response variables, full interpretation of the mechanisms and physical processes responsible in driving these changes in the ocean has yet to be looked at. This is because both the nature of the ocean forcing and response was complex. Firstly, the ocean forcing mode contains two opposite-signed vorticity flux anomalies situated in the western and eastern ocean basins. Secondly, there are two uncorrelated (at any time-lag) upper-isopycnal ocean gyre responses to this anomalous forcing. Clearly, these results are not easily applicable to any single mechanism proposed by studies such as those involving monopolar vorticity fluxes (e.g. Dewar, 2003; Sasaki et al., 2013) and are thus possible governed by more than one mechanism. The simplest explanation for this is that two distinct mechanisms are involved in governing this decadal wind-induced ocean gyre response, one for each vorticity flux anomaly in the western and eastern ocean basins. Our main aim in this chapter is to investigate the validity of this hypothesis through the modelling of multiple, fixed-wind, double gyre circulations.

Section 4.3 shows the reference solutions to the modelled ocean circulation; Section 4.4 shows the time-averaged responses of the double gyre circulation under different fixed wind-stress forcings. A

discussion and summary of the main results are given in Section 4.5.

4.3 Benchmark modelled ocean circulation

4.3.1 Notation

The notation we used in previous sections included left-superscripts of variables such as 'o' or 'a' for ocean and atmosphere, as well as right-subscript, 'm' or integer i, to indicate the mixed layer or i-th isopycnal layer, respectively. Layers were counted away from the ocean-atmosphere interface. In this chapter, we will be restricting our focus on ocean variables only so we will be drop the left superscript and assume all variables are oceanic.

4.3.2 Benchmark ocean forcings

The forcings for the benchmark double gyre circulations are given in Fig. 4.2. Recall that the ocean-only configuration of this model only requires us to define the mechanical forcing τ and thermal forcing $\mathbf{F}$. These are fixed in time and are obtained from taking the time-averages of these variables obtained from the fully coupled model run in Chapter 3.

4.3.3 Defining ocean forcings for double gyre experiments

Although our benchmark ocean circulation is computed using the time-averaged wind-stresses $(\overline{\tau^x_{\text{cpl}}}, \overline{\tau^y_{\text{cpl}}})$ obtained from the benchmark coupled climate in Chapter 3, we will also compute other double gyre circulations by adding on some wind-stress anomaly (τ'^x, τ'^y) onto $(\overline{\tau^x_{\text{cpl}}}, \overline{\tau^y_{\text{cpl}}})$. Since the primary aim of this chapter is to understand the spatial inhomogeneity of the ocean gyre response to wind-stress curls found in Chapter 3, we will base our forcings on the aforementioned wind-stress anomalies shown in Figs. 4.1a,b. We will check the effect of both positive and negative phases of these wind-stress anomalies for completeness and scale them according to their respective measures of

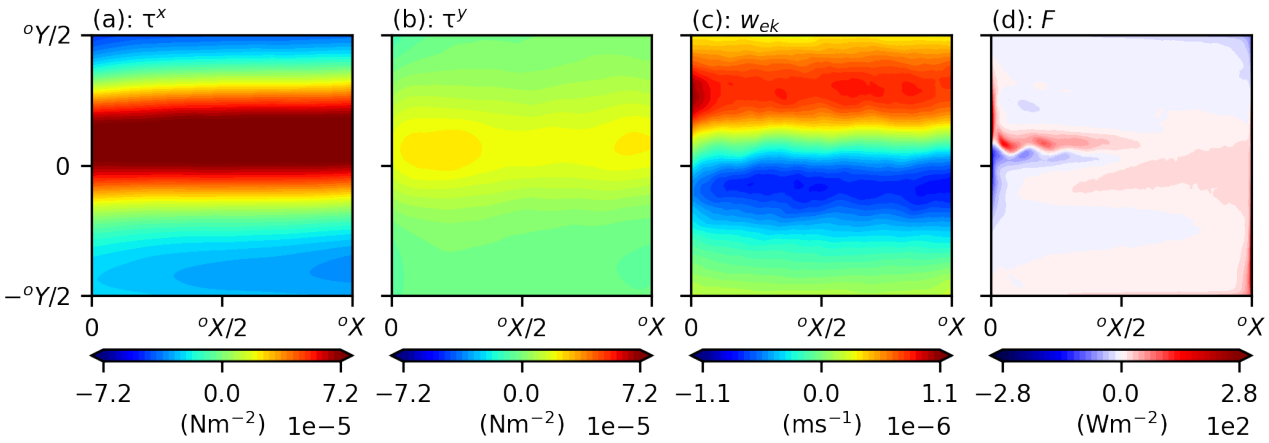

Figure 4.2: Prescribed ocean forcings used in the benchmark solution for the ocean-only configuration of Q-GCM. Note that the Ekman pumping forcing in (c) is not directly passed into the model, but rather, it is the wind-stress fields (a, b) that are used. These prescribed forcings are obtained from the time-averaged benchmark solutions obtained from the coupled configuration of Q-GCM in Chapter 3. (a): Zonal wind-stress. (b): Meridional wind-stress. (c): Ekman pumping. (d): Diabatic heating.

variability (see Section 4.4 for list of forcings used). Further double gyre circulations with modified wind-stresses derived from Figs. 4.1a,b will be computed and defined later on in the chapter (see Subsection 4.4.5).

Although the diabatic heating term F is able to influence the diabatic entrainment e_1, we will assume this effect is relatively small and leave it unchanged in order to isolate the effects of wind-stress anomalies on the gyres. This removes adding unnecessary variables to the experiments which may over-complicate the dynamical picture.

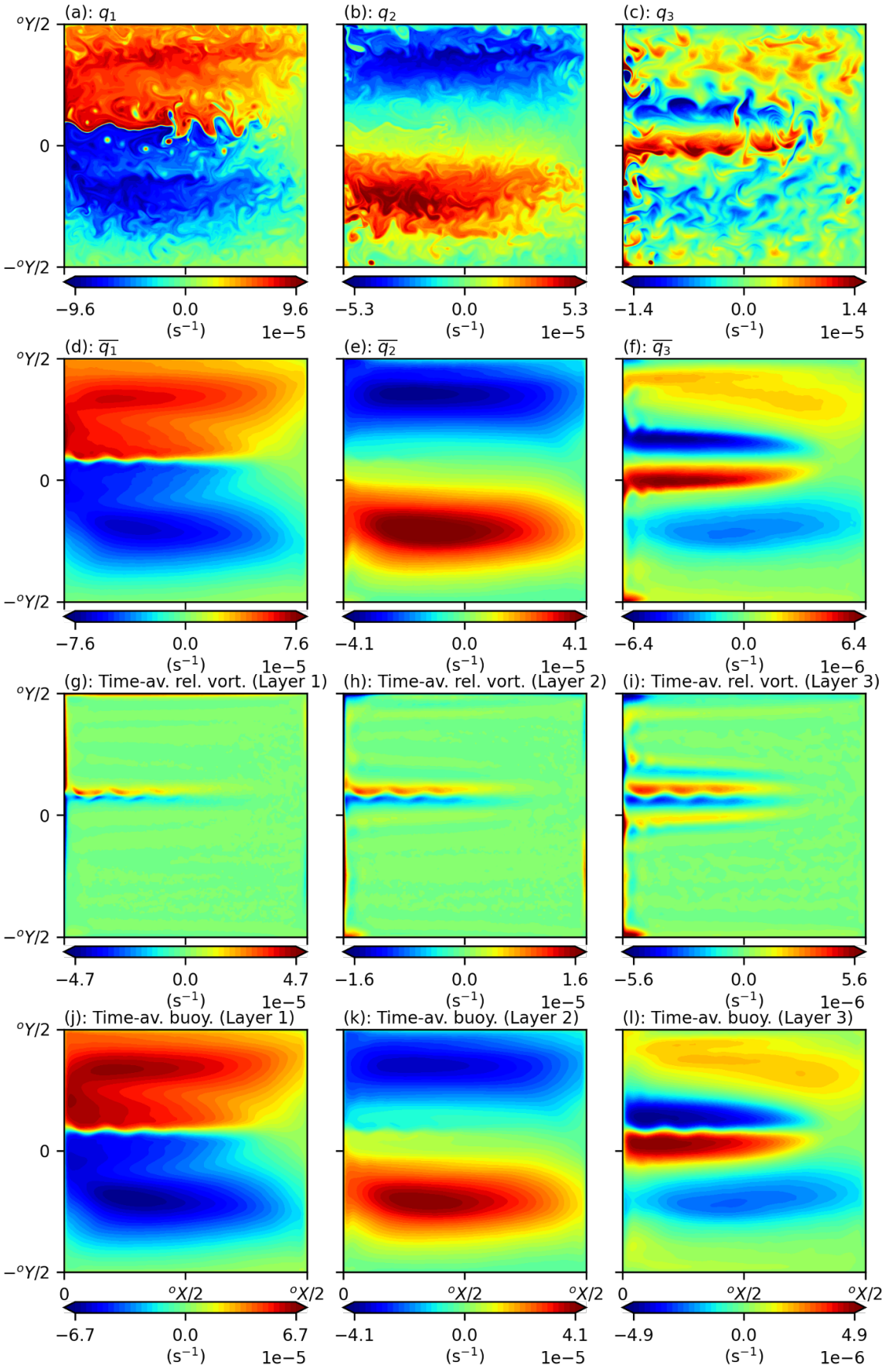

Figure 4.3: PV anomalies, relative vorticity and buoyancies for the double gyre circulation in statistical equilibrium. Left to right panels show upper- to lower-isopycnal layers, respectively. (a - c): Instantaneous PV anomalies. (d - f): Time-averaged PV anomalies. (g - i): Time-averaged relative vorticities. (j - l): Time-averaged buoyancy.

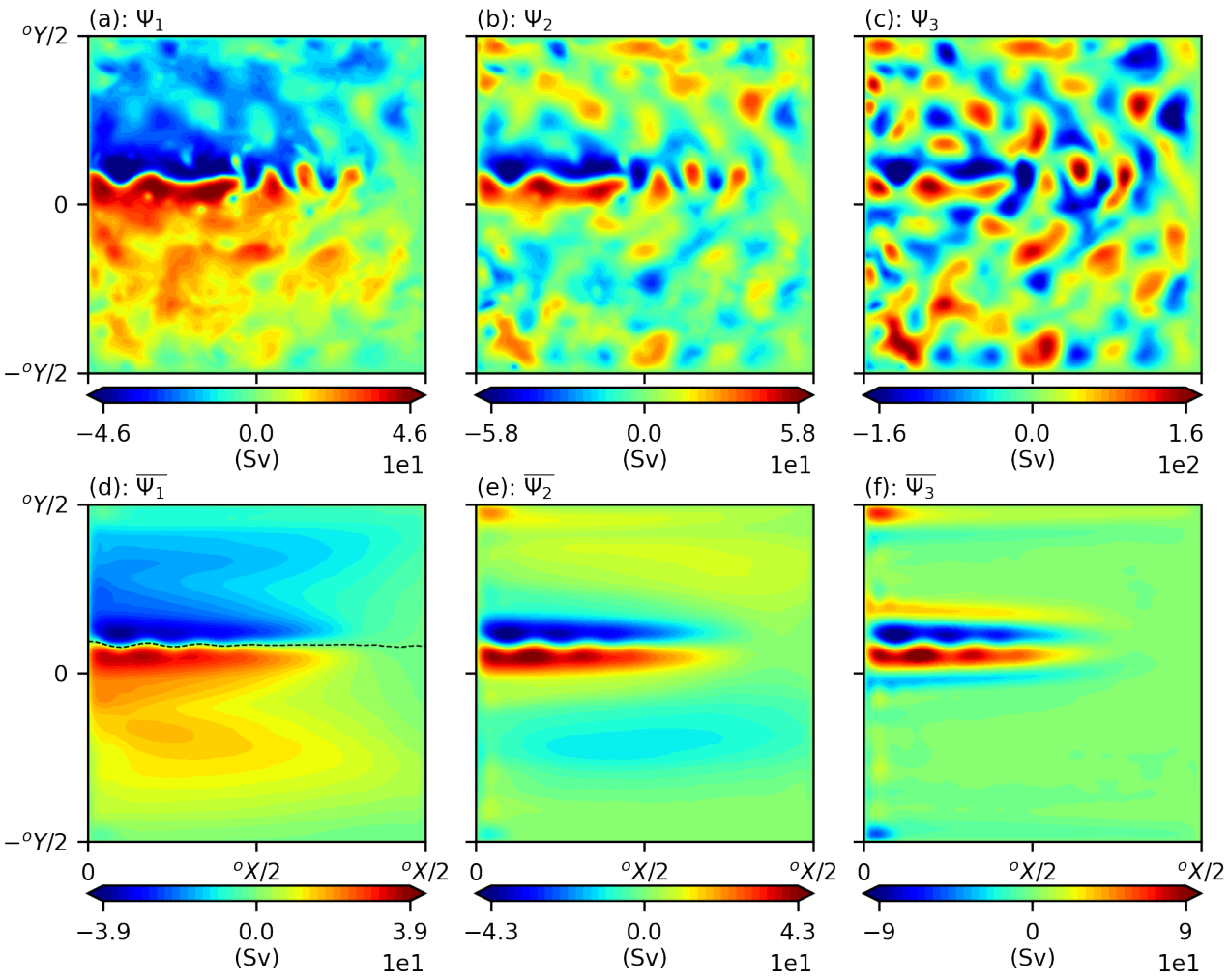

Figure 4.4: Transport streamfunctions for the double gyre circulation in statistical equilibrium. Top and bottom panels correspond to instantaneous and time-averaged fields, respectively. Left to right panels show upper- to lower-isopycnal layers, respectively. See Subsection 2.3.1 for the calculation method.

4.3.4 Reference solutions

We now present the benchmark double gyre circulation using the model described in Subsection 2.1.2 with a simulation period of 120-yrs with a 20-yr spinup period. The chosen fixed-in-time mechanical wind-stress and diabatic thermal forcings are given in Fig. 4.2. The instantaneous and time-averaged PV anomalies are shown in Fig. 4.3, as well as their constituent relative vorticity and buoyancy components. Fig. 4.4 shows the instantaneous and time-averaged transport streamfunction fields. In the upper-isopycnal layer, the ocean gyres consist of large pools of positive and negative PV anomaly in the subpolar and subtropical gyres with inter-gyre exchanges of PV anomalies con-

trolled by mesoscale eddies which are shed off by the powerful eastward jet. The middle-isopycnal layer is driven by diabatic entrainment of opposite sign to the upper-isopycnal layer. The consequent sign change in the PV in the middle-isopycnal layer is due to both the strong circulation in upper-isopycnal layer combined with the diabatic entrainment forcing. PV homogenisation by the effect of eddies is also clearly visible in the middle-isopycnal layer (Rhines and Young, 1982). The lower-isopycnal layer is not directly forced by Ekman pumping or diabatic entrainments and is only driven by nonlinear dynamics due to eddy effects (Holland and Rhines, 1980).

Figs. 4.3g-l show the time-averaged relative vorticity and buoyancy components of PV anomaly in each layer. Relative vorticity appears weak in the vast majority of the ocean basin except near the western and southern boundaries where they lead to the generation of sharp relative vorticity gradients. This induces large viscous boundary fluxes of PV which drains the gyres of enstrophy. There are also relative vorticity contours situated along the jet which is advected from the WBCs. This is because although the WBLs drain PV from the gyres, the effects of nonlinear dynamics in this region inhibits its ability to do so (Cessi et al., 1987; Lozier and Riser, 1989; Kurashina et al., 2021). On the other hand, buoyancy appears dominant in the remainder of the gyres and along the eastward jet extension and recirculation zones. Large pools of time-averaged buoyancies in these regions allow for the development of baroclincic instabilities which propagate eddy momentum into the lower layers through form stresses (McWilliams, 2008).

The instantaneous and time-averaged SSTs are also presented in Figs. 4.5a,b. SSTs have a similar structure to Fig. 4.3a, consisting of a warmer subtropical gyre which is separated from the cooler subpolar gyre by the SST front. Again, we see inter-gyre exchanges of warm and cold mesoscale eddies due to the turbulent eastward jet extension. The main effect of this SST front is to shift the vorticity fluxes from dominating in the subpolar gyre, as is the case for Ekman pumping (Fig. 4.2c), to dominating in the subtropical gyre (Fig. 4.5c). This creates a roughly equal total vorticity flux for each gyre in the upper-isopycnal layer but creates a significant vorticity flux imbalance in the middle isopycnal layer which only receives diabatic forcing.

Qualitatively, this benchmark ocean circulation is similar to the benchmark ocean circulation in Chapter 3. This is as expected as the parameter choices for the ocean model are identical for both. One

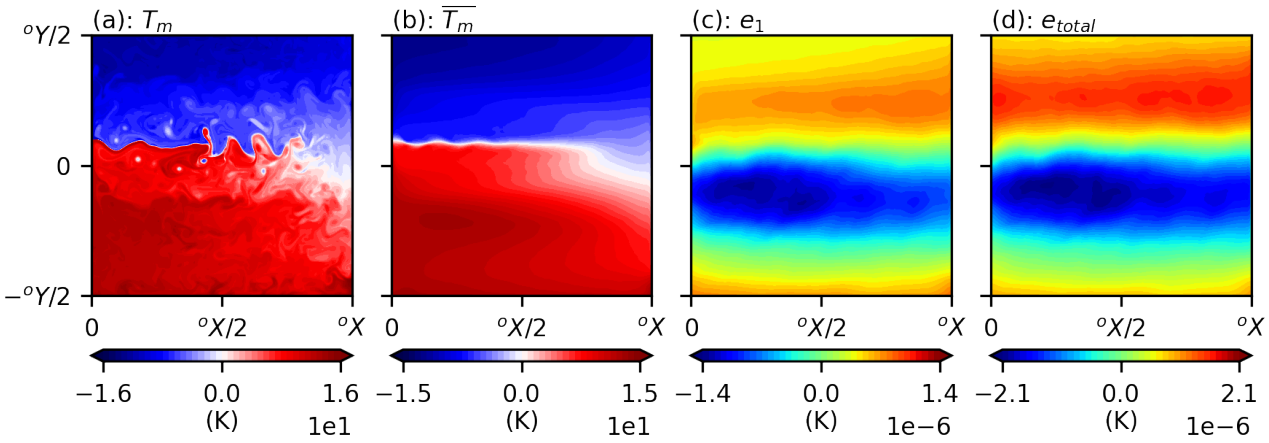

Figure 4.5: SSTs, diabatic and upper ocean total entrainment in the ocean mixed layer for the double gyre circulation. (a): Instantaneous SST. (b): Time-averaged SST. (c): Time-averaged diabatic entrainment,. (d): Time-averaged upper ocean total entrainment.

difference appears to be that the eastward jet extension and recirculation zones appear stronger in the ocean-only configuration of the model, with the time-averaged mass transport increasing by around 10% in each isopycnal layer. This is expected since time-varying ocean forcing, which is the case in the coupled configuration of this model from Chapter 3, has the effect of destabilising the eastward jet extension which causes the jet to break apart more often. For example, highly variable Ekman pumping anomalies near the jet separation region have been shown to weaken the global ocean gyre circulation (Hogg et al., 2009). We also observe that there are sharper PV and SST gradients across the eastward jet and SST fronts, respectively. This is also due to reduced inter-gyre exchanges of PV and heat across the more stable jet.

PV flux from	SP (Upper)	ST (Upper)	SP (Middle)	ST (Middle)
Wind (G_{W})	Mean: $+2.86$ σ: 0.02	Mean: -2.66 σ: 0.02	Mean: -0.66 σ: 0.01	Mean: $+0.66$ σ: 0.01
Inter-gyre PV (G_{IF})	Mean: -1.57 σ: 2.99	Mean: $+1.58$ σ: 2.99	Mean: $+0.24$ σ: 0.29	Mean: -0.25 σ: 0.29
Viscous boundary flux (G_{VB})	Mean: -1.17 σ: 0.11	Mean: $+0.96$ σ: 0.12	Mean: $+0.37$ σ: 0.06	Mean: -0.36 σ: 0.07
Tendency (G_{T})	Mean: $+0.11$ σ: 2.98	Mean: -0.12 σ: 2.98	Mean: $+0.04$ σ: 0.30	Mean: $+0.05$ σ: 0.30

Table 4.1: Reference (Control) time-averaged, gyre-integrated PV budget of benchmark double gyre circulation for upper- and-middle isopycnal layers ($\mathrm{m}^2\mathrm{s}^{-2}$). Values in brackets indicate the standard deviations of the corresponding gyre-integrated PV flux. SP and ST indicate subpolar and subtropical gyres, respectively.

Now that we have shown our reference double gyre circulation, we move onto defining our different

mechanical forcings to simulate multiple other double gyre circulations. In Chapter 3 we linked anomalous ocean forcings to certain delayed responses in our double gyre circulation. We will now attempt to isolate these ocean responses by reproducing the correct upper ocean total entrainment forcings in terms of fixed wind-stresses which we will use to drive the circulation.

4.4 Time-averaged ocean gyre responses under different fixed mechanical forcings

4.4.1 Experiment design

We now run two double gyre circulation experiments with different mechanical forcings. The model parameters are identical to those used in the benchmark simulated ocean circulation with the only variable being the mechanical forcing, or wind-stresses, while keeping the thermal forcing fixed. This approach allows us to isolate the first-order effects of momentum transfers from the ocean due to wind-stresses on the double gyre circulation. Simulation periods of 120-yrs, with a 20-yr spinup period, are chosen to reduce uncertainty due to strong decadal variability of the gyres. Our main aim from running these experiments is to determine whether certain prescribed, fixed wind-stress forcings reproduce the expected ocean gyre responses. In addition, we are also interested in gaining some insight into the physical processes and mechanisms involved with inducing any changes in the double gyre circulation. In particular, we would like to show that eastern and western basin vorticity fluxes induced by wind-stress curl anomalies generate two distinct responses in the upper-isopycnal ocean.

Our prescribed wind-stress forcing is constructed by adding some wind-stress vector anomaly onto the benchmark double gyre forcing $\overline{\tau_{\text{cpl}}}$ given in Figs. 4.2a,b. Since the aim of these experiments is to reproduce the ocean gyre forcings and responses from Chapter 3, we will choose the wind-stress anomalies to be those shown in Figs. 4.1a,b. The structure of the wind-stress anomalies in Figs. 4.1a,b is such that they lead to an east-west dipole wind-stress curl anomaly in the ocean basin. These patterns are scaled by (σ^x, σ^y) which correspond to one standard deviation of the corresponding mode-strength time series, or principal component (von Storch and Zwiers, 1999). This is computed

using data obtained from Chapter 3. Two separate double gyre circulations will be computed such that ocean gyre responses to both polarities, or phases, of the wind-stress anomalies may be checked. These two experiments and their corresponding forcings are given in Table 4.2. After checking the responses of the double gyre circulation under these different wind-stress forcings, we will compute time-averaged, gyre-integrated PV budgets of the upper- and middle-isopycnal layers (see Subsection 2.3.2). The lower-isopycnal layer budgets are neglected as they are not directly forced by winds.

Experiment No.	Wind-stress τ
Control (Reference solution)	$\tau = \overline{\tau_{\text{cpl}}}$
1	$\tau = \overline{\tau_{\text{cpl}}} + \tau_{\text{eof}}$
2	$\tau = \overline{\tau_{\text{cpl}}} - \tau_{\text{eof}}$

Table 4.2: List of forcings used in the PV budgets computed under different Ekman pumping regimes. The Control forcing is τ_{cpl} in Figs. 4.2a,b. The wind-stress anomalies are given in Figs. 4.1a,b and are scaled by 1 standard deviation of its measured temporal variability in Chapter 3.

From these two experiments run under different mechanical forcings, we are interested in: 1) Are we able to reproduce similar ocean gyre responses, in a time-averaged sense, to those found in Chapter 3? 2) What are the associated changes in the PV budgets relative to the benchmark circulation?; 3) What are the likely physical processes involved? We will answer these questions in the context of a key hypothesis made in Chapter 3: that the ocean gyre response to vorticity flux anomalies in the western and eastern ocean basins are governed by distinct mechanisms.

4.4.2 Time-averaged ocean forcings under prescribed wind-stresses

Fig. 4.6 shows the time-averaged modelled Ekman pumping, diabatic and upper ocean total entrainments. The modelled Ekman pumping forcing is almost identical in structure to that of Fig. 4.1c which is expected since the corresponding wind-stress and Ekman pumping modes were found to be highly correlated in Chapter 3. Note that our modelled Ekman pumping is 15% weaker than what is observed in the coupled model which is likely due to the lack of positive feedbacks. These east-west dipole Ekman pumping anomalies that sit largely over the subpolar gyre are then pushed equatorward and into a narrower latitudinal band by the SST distribution in the form of diabatic entrainments. Although the structure of this forcing is modified and strengthened by the SST field, the east-west dipole forcing pattern is still maintained. Indeed, the diabatic forcing is a considerable 60% stronger

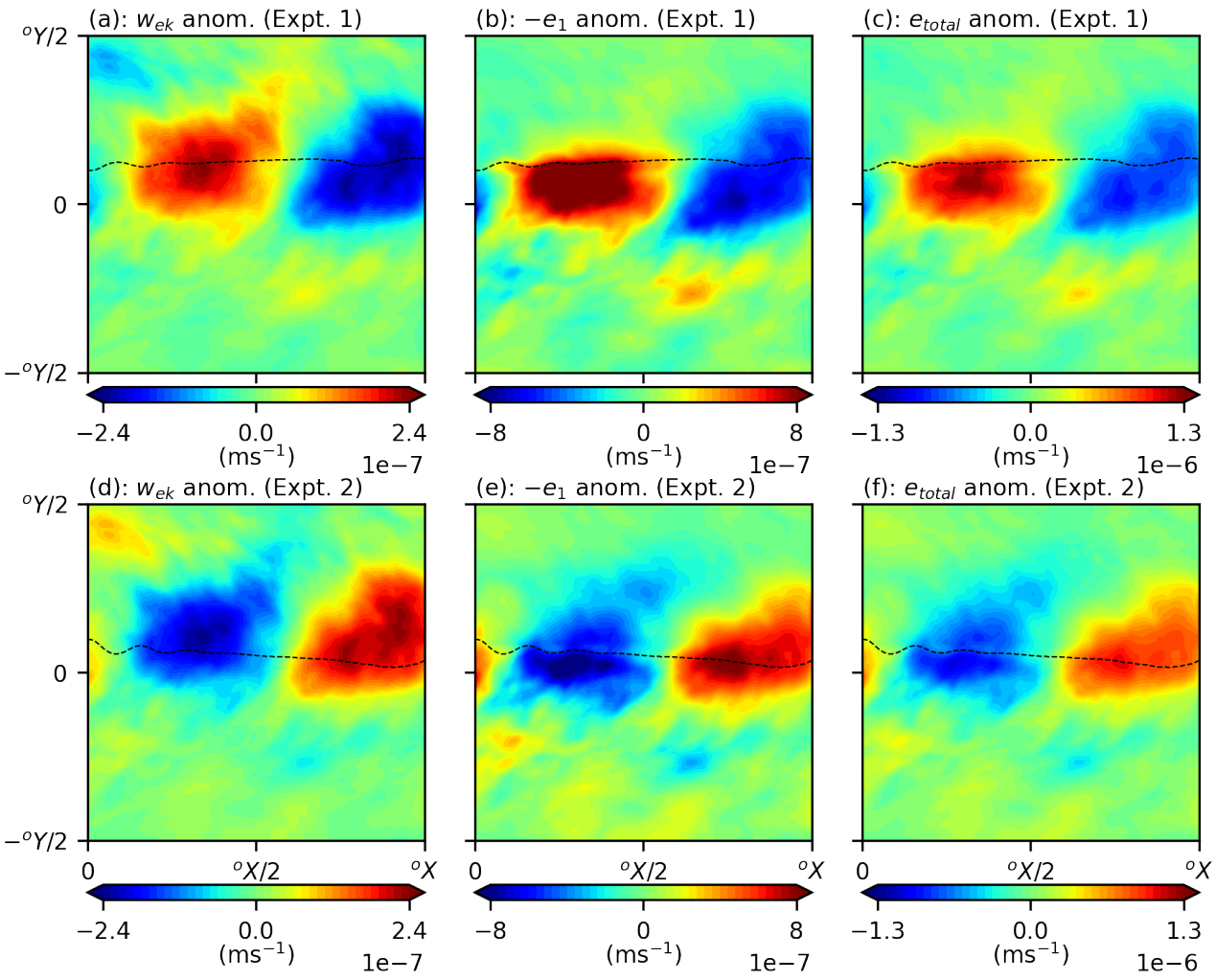

Figure 4.6: Time-averaged ocean forcing anomalies for Experiments 1 and 2 in comparison to the Control (see Table 4.2). Top row shows forcing anomalies for Experiment 1 and bottom row shows forcing anomalies for Experiment 2. (a, d): Ekman pumping anomaly. (b, e): Diabatic entrainment anomaly (sign-flipped to show upper-isopycnal). (c, f); Upper ocean total entrainment. Black dashed line indicates time-averaged position of inter-gyre boundary for the respecive modelled double gyre circulation.

than what is measured in the coupled model, this is likely due to the highly idealised formulation of diabatic heating in the ocean (see Subsection 2.1.2). Analysis from Chapter 3 similarly found that although the SST field was only able to partially modify the ocean forcing structure, its large-scale structure and variability was controlled by the atmospheric variability.

Overall, the modelled ocean forcings show that the simple addition of wind-stress anomalies, without modification of diabatic heating, is able to successfully reproduce east-west dipole vorticity flux patterns in the ocean basin. Although the modelled ocean forcings are not entirely perfect, e.g. overly strong diabatic entrainment, our aim is not in perfectly reproducing the exact ocean forcings, but in

understanding the response of the ocean gyres to vorticity flux anomalies over the western and eastern basins. Hence, these modelled ocean forcings will suffice for the needs of our analysis.

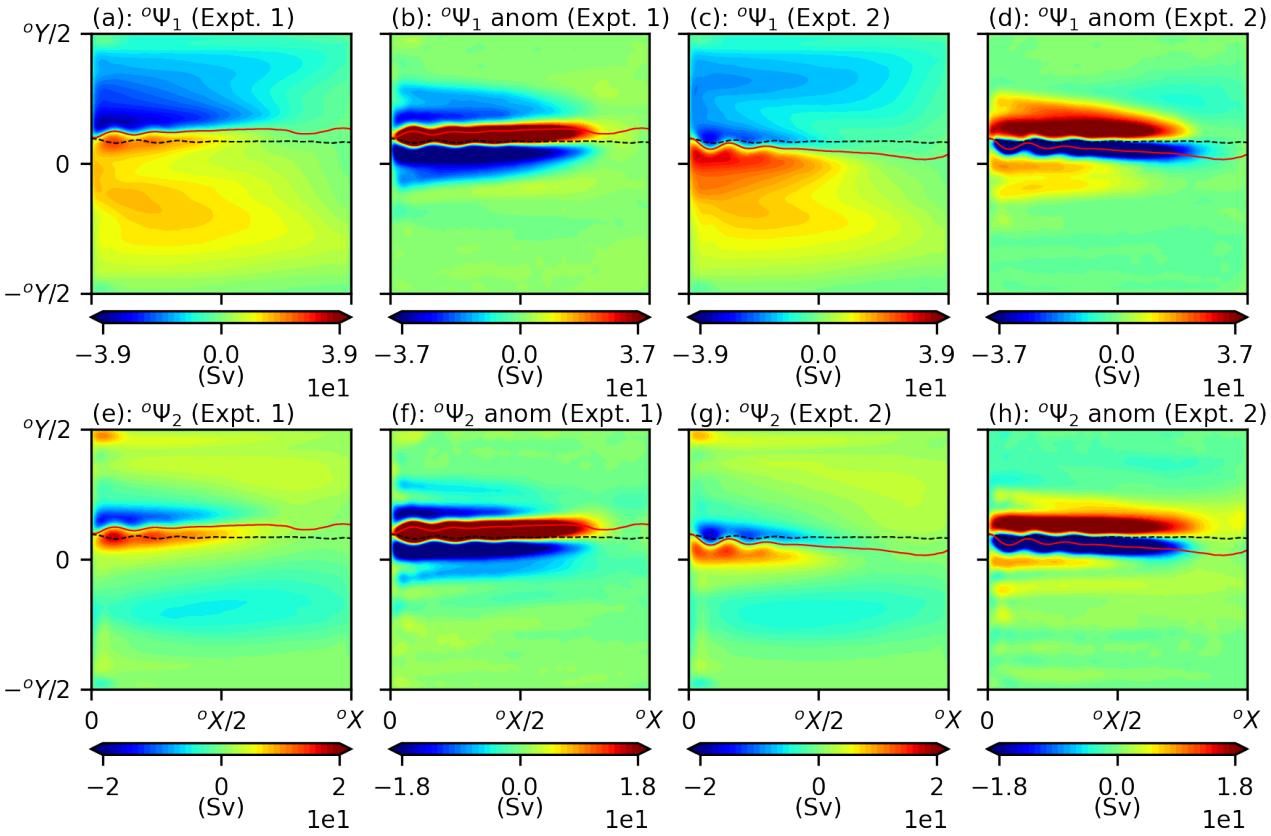

Figure 4.7: Time-averaged transport streamfunctions and deviations from Control for Experiments 1 and 2. Black dashed line indicates time-averaged position of the inter-gyre boundary in the Control Experiment; red filled line indicates time-averaged position of inter-gyre boundary in the respective experiment. Panels (a, c) and (e, g) are plotted with the same colorbar as Figs. 4.4d and 4.4e, respectively. Panels (b, d, f, h) are saturated to show the weaker circulation anomalies in the inertial recirculations. (a, b): Upper-isopycnal time-averaged transport streamfunction for Experiment 1 and anomaly from Control. (c, d): Upper-isopycnal time-averaged transport streamfunction for Experiment 2 and anomaly from Control. (e, f): Middle-isopycnal time-averaged transport streamfunction for Experiment 1 and anomaly from Control. (g, h): Middle-isopycnal time-averaged transport streamfunction for Experiment 2 and anomaly from Control.

4.4.3 Time-averaged circulation response to wind-stress anomalies

The time-averaged response of the upper-isopycnal ocean circulation is shown in Fig. 4.7. Note that the ocean gyre circulations in Experiments 1 and 2 have weakened eastward jet extensions and gyres in comparison to the Control with both jets showing reductions in time-averaged mass transports. This is expected since the derived wind-stress anomalies act to increase the wind-forcing asymmetry into

the gyres from a relatively straight east-west forcing (Fig. 4.2c) to more convoluted forcings (Figs. 4.6a-d). Weakened eastward jet extensions due to increased wind-forcing asymmetry have been noted by Rhines and Schopp (1991), particularly near the eastward jet separation region (Hogg et al., 2009).

The wind-stress forcing in Experiment 1 leads to a weakened subtropical recirculation zone, strengthened subpolar recirculation zone and a poleward shift change in the jet-axis tilt. This change in jet-axis tilt is consistent with findings by Moro (1988) and Hogg et al. (2005) where the dominant recirculation zone, in this case the subpolar recirculation, pulls the jet towards itself. This slightly counter-intuitive result is because the dynamics of the ocean gyres is controlled by the PV circulation, rather than inertia. The entire eastward jet is also shifted poleward in comparison to the benchmark circulation except at the eastward jet separation region where the subtropical WBC is deflected poleward, rather than equatorward, as it separates from the western boundary. These changes in the circulation are largely consistent with findings in Chapter 3 where changes in strength of the recirculation zones and a poleward shift in the eastward jet extension were also observed. The anomalous circulation shown for the upper- and middle-isopycnal layers (Figs. 4.7b,f) are almost identical in structure and show an asymmetric tripole anomaly along the eastward jet and recirculation zones. The largely barotropic structure of this anomaly indicates downwards transfers of momentum from the upper-isopycnal layer in the form of eddy form stresses (McWilliams, 2008). However, the response of the middle-isopycnal layer is such that the subpolar recirculation zone now has a greater vertical shear, while the subtropical recirculation zone has a lesser vertical shear (in comparison to Figs. 4.4d,e) This effect will be shown to have an important consequence on the baroclinicity of the inertial recirculations and vertical momentum transfers later on. Similar patterns as modes of decadal ocean gyre variability have been noted by Hogg et al. (2005); Berloff et al. (2007b, etc.) and have been described more simply as 'meridional jet shift' modes. We will describe this mode as a combination of relative recirculation zone strength change, leading to a change in jet-axis tilt, and a separate northward meridional shift of the entire jet. In our situation, this more detailed decomposition of the asymmetric tripole circulation anomaly is necessary as preliminary analysis from Chapter 3 indicates the changes associated with the relative recirculation zone strength and meridional jet shift are controlled by distinct mechanisms.

In a similar but opposite fashion, wind-stress forcings in Experiment 2 lead to a weakening of the subpolar recirculation zone, strengthening of the subtropical recirculation zone, a consequent equa-

torward shift in the jet-axis tilt, and a equatorward meridional shift of the eastward jet extension in the upper-isopycnal layer. The jet also appears to be now deflected more strongly equatorward as it separates from the western boundary. In the middle-isopycnal layer, the response is such that the subpolar recirculation zone now has a lesser vertical shear and the subtropical recirculation has a greater vertical shear (in comparison to Figs 4.4)

There are certainly differences in the modelled ocean circulation response in comparison to Chapter 3. This includes changes in strength of the subpolar recirculation zone and gyre, along with greater changes in the jet-axis tilt. However, this is not necessarily a problem since both east-west dipole vorticity flux anomalies are still well modelled and generic changes in the inertial recirculations and meridional shifts of the jet are still captured. This means that any findings in this chapter, including the responsible mechanisms, are still of value and applicable to findings of Chapter 3.

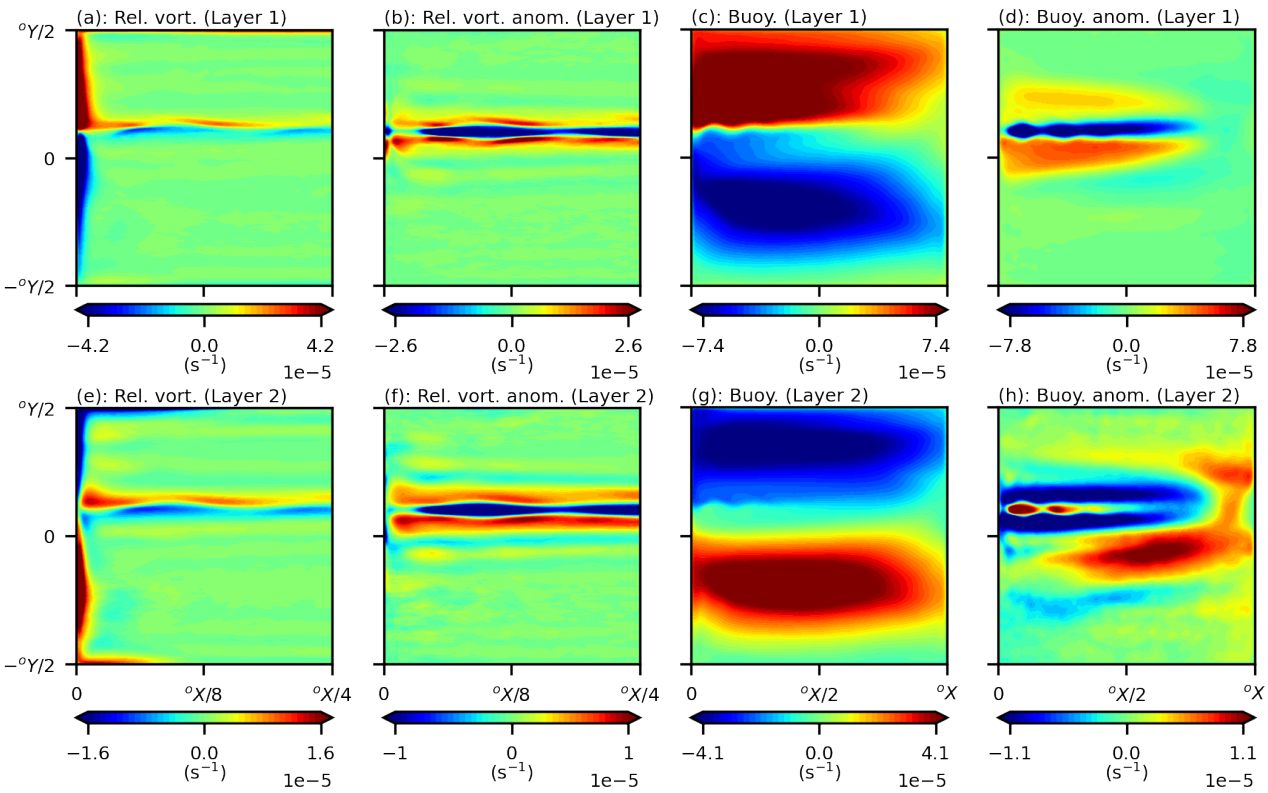

Figure 4.8: Experiment 1 time-averaged relative vorticity and buoyancies with anomalies given relative to reference double gyre circulation (see Figs. 4.3g-l). Top and bottom panels show upper- and middle-isopycnal layers, respectively. Relative vorticities (a, b, e, f) are only shown over the western quarter of the ocean basin to show jet separation region.

4.4.4 Time-averaged PV response to wind-stress anomalies

Figs. 4.8, 4.9 show effects of wind-stress anomalies on the PV anomaly distribution in the gyres. In this case, we have separated out PV anomalies into relative vorticity, which are strongest near the western boundary and inertial recirculation zones, and buoyancy components, which are strong over the entire ocean except near the western boundary. Figs. 4.8b,d and Figs. 4.9b,d reveal the dominant effect on the upper-isopycnal PV is the generation of time-averaged, asymmetric, tripole buoyancy and relative vorticity anomalies over the eastward jet and recirculation zones. The time-averaged buoyancy anomalies are roughly $2-3$ times stronger than the accompanying relative vorticity anomalies over the eastward jet and recirculation zones. The central anomaly of these tripole patterns are largely due to shifts in the time-averaged location of the inter-gyre boundary, while the opposite-signed anomalies that lie adjacent on either side are associated with changes in the recirculation zones. If we compare the circulation changes in the upper- and middle-isopycnal recirculation zones for Experiments 1 and 2, i.e. Figs. 4.7b,d and Figs. 4.7d,h, respectively, with the buoyancy anomalies in the same location, i.e. Figs. 4.8d and 4.9d ,respectively, there is now a corresponding change in the baroclinicity of the inertial recirculation zones. For example, in Fig. 4.8d, the subpolar recirculation zone has increased time-averaged buoyancy, or increased baroclinicity, and the subtropical recirculation zone has decreased time-averaged buoyancy, or decreased baroclonicity. Similar and opposite changes may be observed in Fig. 4.9d. The response of the inertial recirculation zones is a direct consequence of the local anomalous forcing that sits over the region, namely the western basin wind-stress curl anomaly. Through changes in their baroclinicity, this allows the inertial recirculations to either more or less efficiently transfer momentum into the lower layers through baroclinic instabilities.

The positive time-averaged buoyancy anomaly in Fig. 4.9d due to eastern basin wind-stress curls anomalies appears to be connected to the central buoyancy anomaly along the eastward jet extension. This indicates a non-local ocean gyre response but needs to be confirmed with further analysis (see Subsection 4.4.5). Buoyancy anomalies in the middle-isopycnal layer show similar but opposite-signed anomalies along the recirculation zones and eastward jet. There are also time-averaged buoyancy anomalies in the eastern basin on either side of the eastward jet extension associated with the

gyre recirculations of eastern basin vorticity fluxes. Such an anomaly is not visible in the upper-isopycnal layer which indicates the ocean response to eastern basin forcing is baroclinic in nature. This is important since if the eastern basin wind-stress curl in the upper-isopycnal was being advected by the gyre recirculations, then we should be able to observe it like we have done so in the middle-isopycnal layer. We note that we do not observe PV anomalies similar to those in Fig. 4.1f. This is likely due to inaccuracies in the modelled diabatic entrainments from idealised formulations of thermal forcing in the model.

Outside of the eastward jet regions, relative vorticity anomalies only appear significant very close to the eastward jet separation region where local modification of the WBL occurs. For example in Fig. 4.8b, relative vorticity anomalies in the eastward jet separation region is due to the poleward deflection of the subtropical WBC. A similar pattern may be seen in Fig. 4.9b for poleward deflection of the subtropical WBC. Changes in the relative vorticity profile along the remainder of the western boundary are almost negligible, which agree with our findings that the measured changes in ocean gyre circulation are not triggered by processes in the WBL (e.g. Cessi et al., 1987) but more likely by reorganisations of the eastward jet extension and inertial recirculations due to anomalous wind-forcing.

Indeed, we have already postulated that the western basin wind-stress curl anomaly response in the inertial recirculation zones is likely due to nonlinear adjustment of the ocean gyres through effects of advection (Dewar, 2003). However, it is still unclear what the role of the eastern basin wind-stress curls is on the gyres. Furthermore, we are also not sure whether the meridional shift of the eastward jet extension is a secondary response of the recirculation zone nonlinear adjustment or whether it is a separate response related to the eastern basin forcing. We will continue our analysis on this matter in the next Subsection.

4.4.5 Existence of waves and importance of eastern basin forcing

Although a local ocean gyre response may be described for the wind-stress curl anomaly in the western basin, it is unclear from the two double gyre experiments alone whether the wind-stress curls in

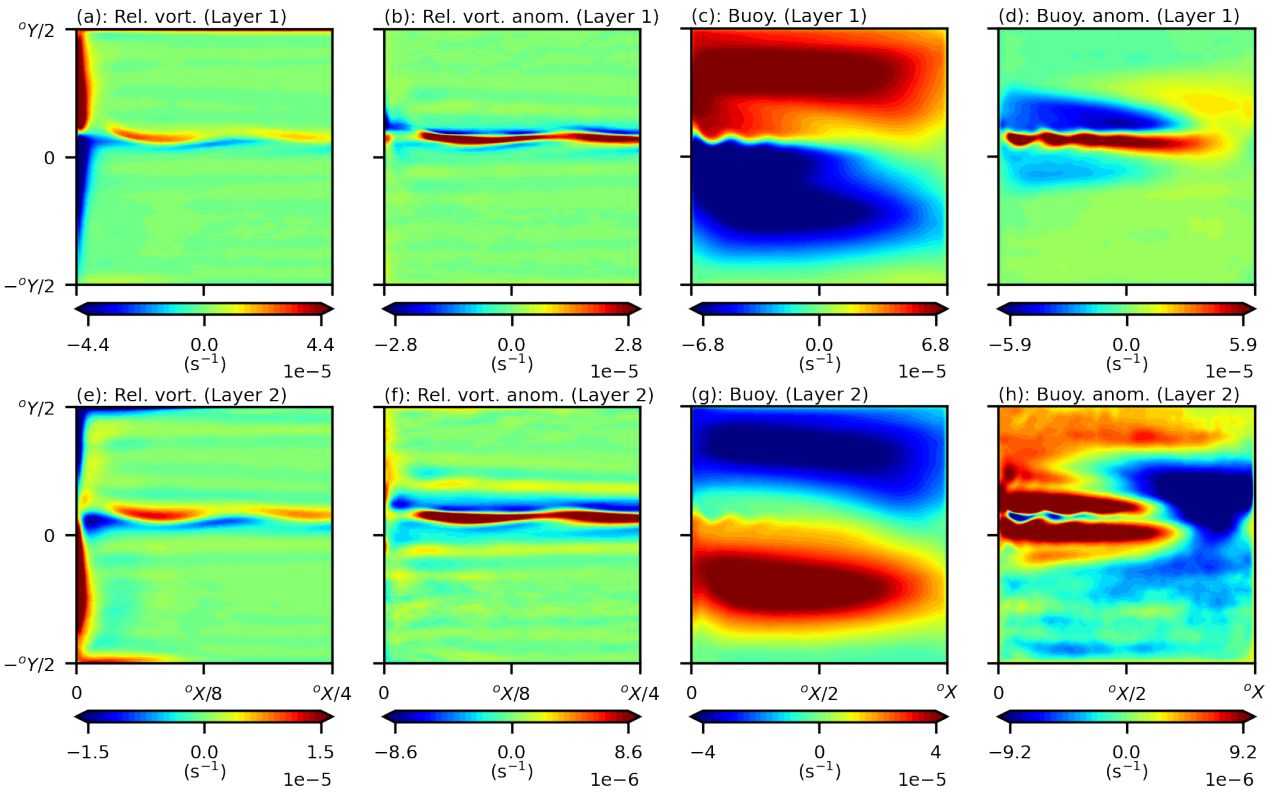

Figure 4.9: Experiment 2 time-averaged relative vorticity and buoyancies with anomalies given relative to reference double gyre circulation (see Figs. 4.3g-l). Top and bottom panels show upper- and middle-isopycnal layers, respectively. Relative vorticities (a, b, e, f) are only shown over the western quarter of the ocean basin to show jet separation region.

the eastern basin are important. For example, we are still not sure whether the meridional shift of the jet is part of the inertial recirculation zone response or whether they are related to eastern basin wind-stress curls. To motivate some further analysis we turn our attention to a relevant hypothesis by Sasaki and Schneider (2011) and Sasaki et al. (2013). They postulated a westward-propagating baroclinic Rossby wave induced by a wind-stress curls in the eastern North Pacific is responsible for meridional shifts in the Kuroshio extension. Since this effect is non-local to the forcing[1], we cannot directly check whether this mechanism is involved by looking at the time-averaged ocean gyre responses in Fig. 4.7 alone. Hence, further work is needed to check that such a mechanism is feasible in our modelled double gyre circulation.

We may check for the presence of westward-propagating signals from the eastern basin by plotting time-longitude plots of PV anomalies (see Fig. 4.10). We change coordinate systems such as we track the PV along the time-averaged position of the eastward jet extensions, i.e. the inter-gyre boundaries,

[1]Unlike forcing over the western basin where the response in the recirculation zone is local to its forcing

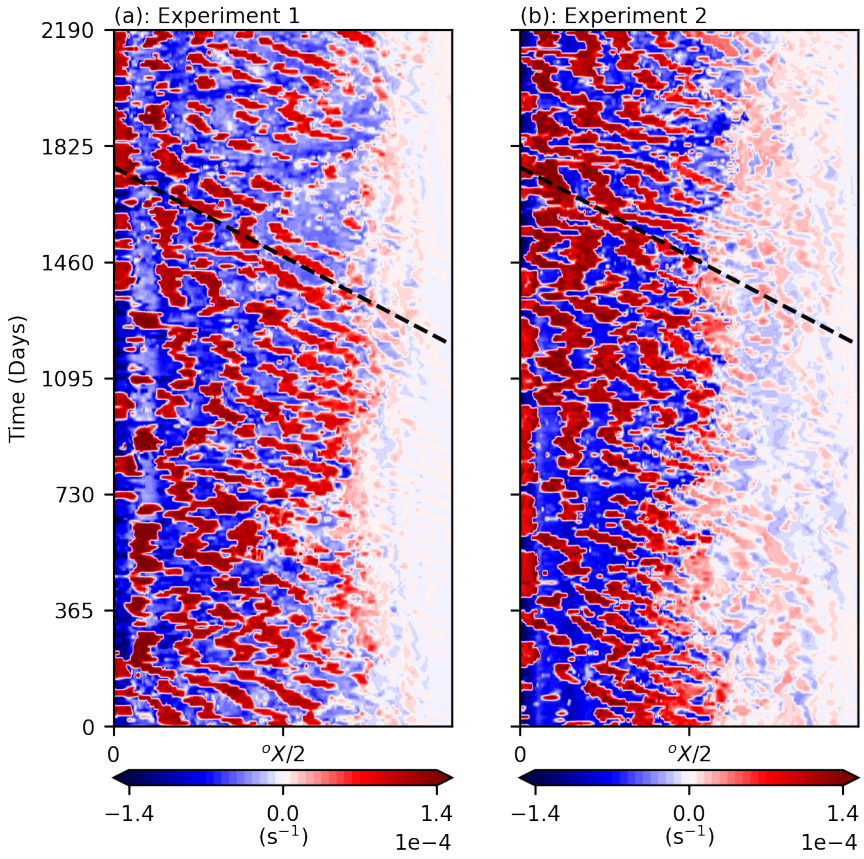

Figure 4.10: Presence of nonlinear, baroclinic Rossby waves along the eastward jet extension. Data is taken over a 6-yr period for the system in statistical equilibrium. (a): PV anomalies along the time-averaged position of the eastward jet extension in Experiment 1. (b): PV anomalies along the time-averaged position of the eastward jet extension in Experiment 2. Approximate trajectory of wave is plotted in both panels with a phase speed $c_R = 10\,\mathrm{cm\,s^{-1}}$.

in each experiment. Both experiments show there are clearly westward-propagating Rossby waves along the eastward jet extension with wave formation in the eastern basin. There is a noticeable increase in concentration of PV as the Rossby waves enter the eastward jet extension region. Such an intensification is consistent with the narrowing of the meridional scale of the wave as it enters the eastward jet extension region. This is because the wave narrows in structure it increases in PV concentration in order to conserve PV (Sasaki et al., 2013). Rossby wave phase speed is approximated using a basin crossing time of $\sim$ 1.5-yrs which yields a propagation speed of $c_R = 10\,\mathrm{cm\,s^{-1}}$. These speeds are around twice as fast as those predicted by Dewar (2003) and Sasaki et al. (2013). This could be due to quasilinear interaction of the Rossby wave with the mean flow which increases wave speed propagation (Dewar and Morris, 2000). However, this is just a hypothesis and further work which is outside the scope of this thesis is necessary to fully understand this phenomenon.

Note that although it is clear that westward-propagating wave behaviour is visible along the eastward jet, the signal is strongly influenced by the powerful effects of advection. Indeed, many of the propagating waves appear to be destroyed by effects of time-averaged advection of the eastward jet which may be seen by the presence of Rossby deformation scale standing waves (Fig. 4.10), particularly near the western boundary where the jet is strongest. These regions also show strong, intrinsic, interannual variability of the eastward jet that occurs due to vigorous mesoscale activity. This means that although Rossby wave signal travels at a largely predictable speed, their arrival at the western boundary is not guaranteed. This leads to reduced predictability of wind-induced ocean gyre variability due to strong effects of time-averaged advection and intrinsic variability of the eastward jet.

Finally, to check that eastern basin vorticity flux anomalies do indeed induce meridional shifts of the eastward jet extension, we run another two additional sets of double gyre simulations with modified forcings from Experiments 1 and 2. These modified wind-stress forcings are identical except that the eastern basin vorticity flux anomaly is weakened by setting the eastern basin zonal wind-stress anomalies in Fig. 4.1b to zero. These modified Experiments 1 and 2 double gyre forcings will be referred to as supplementary Experiments 3 and 4 forcings, respectively.

Figs. 4.11a,b,d,e show the modelled time-averaged Ekman pumping and upper ocean total entrainments under the reduced eastern basin wind-stress forcings. It is easy to see that setting the eastern basin zonal wind-stress anomaly in Fig. 4.1b to zero does indeed reduce both the time-averaged Ekman pumping and upper ocean total entrainments in the region by $\sim 50\%$. Furthermore, western basin forcings appear almost identical to those shown in Figs. 4.6a,c,d,f. Hence, it is reasonable to assume that any observed changes between the modelled circulations in Figs. 4.11c,f and Figs. 4.7a,c, respectively, are purely due to reduced wind-stress curls in the eastern ocean basin.

Indeed, the reduced eastern basin wind-stress curl anomaly leads to an equatorward meridional shift of the inter-gyre boundary in Fig. 4.11c and a poleward meridional shift of the inter-gyre boundary in Fig. 4.11f. The strengths of the inertial recirculation zones and axis tilt of the eastward jet remain identical, or very similar, to Figs. 4.7a,c. This agrees with our hypothesis that the western basin vorticity flux anomaly is responsible for changes in strength of the inertial recirculation zones. Furthermore, and more interestingly, this also implies that the eastern basin wind-stress anomaly is re-

sponsible for independently controlling meridional shifts of the inter-gyre boundary. The direction of the meridional shifts in Fig. 4.11b,c is consistent with the baroclinic Rossby wave adjustment mechanism proposed by Sasaki et al. (2013), with an anti-cyclonic wind-stress curl leading to a poleward meridional shift of the eastward jet. However, in these experiments we show the direction of induced meridional shift by reducing wind-stress curl anomalies in the eastern basin. The magnitude of the shift observed in each panel is around 75 km which is slightly less than the meridional shifts measured in Chapter 3. This is expected since the eastern basin wind-curls are only reduced in magnitude and not set to zero.

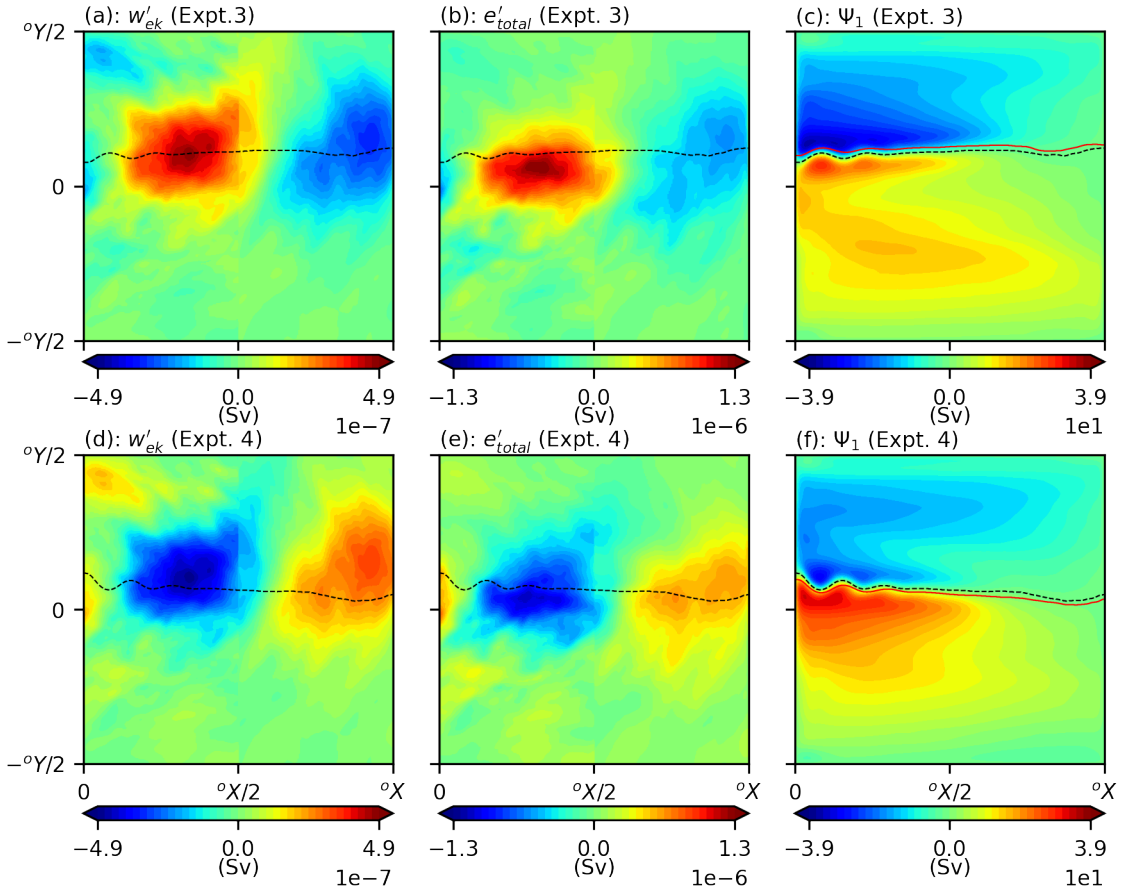

Figure 4.11: Modified ocean forcing and time-averaged ocean gyre responses to this wind-stress anomaly. (a, d): Modified Ekman pumping for Experiments 3 and 4, respectively. (b, e): Modified upper ocean total entrainment for Experiments 3 and 4, respectively. (c, f): Time-averaged upper-isopycnal transport streamfunction for Experiments 3 and 4, respectively. Time-averaged positions of the inter-gyre boundary from Experiments 1 and 2 are given by the filled red lines. The time-averaged positions of the inter-gyre boundary from Experiments 3 and 4, i.e. the modified forcings, are given by the dashed black lines.

4.4.6 Time-averaged response of PV sources and sinks in the ocean gyres

PV flux from	SP (Upper)	ST (Upper)	SP (Middle)	ST (Middle)
Wind (G_{W})	$+2.66\,(-0.20)$	$-2.47\,(+0.19)$	$-0.57\,(+0.09)$	$+0.57\,(-0.09)$
Inter-gyre PV flux (G_{IF})	$-1.37\,(+0.20)$	$+1.37\,(-0.21)$	$+0.15\,(-0.09)$	$-0.15\,(+0.10)$
Viscous boundary flux (G_{VB})	$-1.13\,(+0.04)$	$+0.95\,(-0.01)$	$+0.38\,(+0.01)$	$-0.37\,(-0.01)$
Tendency (G_{T})	$+0.17\,(+0.06)$	$-0.16\,(-0.04)$	$-0.04\,(-0.08)$	$+0.05\,(+0.00)$

Table 4.3: Experiment 1 time-averaged, gyre-integrated PV budget for upper- and middle-isopycnal layers ($\mathrm{m}^2\mathrm{s}^{-2}$). Values in brackets indicate the change in time-averaged PV flux compared to the reference PV budget with Control forcing. SP and ST indicate subpolar and subtropical gyres, respectively.

The time-averaged, gyre-integrated PV budgets for Experiment 1 in the upper- and middle-isopycnal layers are given in Table 4.3. In the upper-isopycnal layer, there is a $7-8\%$ drop in the wind-induced vorticity fluxes for each gyre. This is expected since asymmetry of the forcing has now increased as well as the jet-axis tilt change due to the adjustments in relative recirculation zone strengths. To counteract this, the inter-gyre PV flux in the gyres falls by 20% and the viscous boundary fluxes fall by $1-4\%$. I.e. there is a drop in measured PV sinks due to the drop in available PV in the gyres. In this experiment, the inter-gyre PV flux handles the vast majority of the decrease in wind-induced vorticity flux while the viscous boundary fluxes only account for a small portion. This is consistent with our findings that the western boundary layer is only adjusted near the jet separation region so changes in the viscous boundary flux will consequently be small. The changes in the PV budget were found to be statistically significant under a one-tailed Student's *t*-test with a 95% confidence interval. Changes in the PV tendency were not found to be statistically significant.

PV flux from	SP (Upper)	ST (Upper)	SP (Middle)	ST (Middle)
Wind (G_{W})	$+2.79\,(-0.07)$	$-2.58\,(+0.18)$	$-0.64\,(+0.02)$	$+0.64\,(-0.02)$
Inter-gyre PV flux (G_{IF})	$-1.50\,(+0.07)$	$+1.50\,(-0.08)$	$+0.23\,(-0.01)$	$-0.24\,(+0.01)$
Viscous boundary flux (G_{VB})	$-1.12\,(+0.05)$	$+0.88\,(-0.08)$	$+0.36\,(-0.01)$	$-0.35\,(+0.01)$
Tendency (G_{T})	$+0.17\,(+0.06)$	$-0.19\,(-0.07)$	$-0.04\,(-0.08)$	$+0.05\,(+0.00)$

Table 4.4: Experiment 2 time-averaged, gyre-integrated PV budget for upper- and middle-isopycnal layers ($\mathrm{m}^2\mathrm{s}^{-2}$). Values in brackets indicate the change in time-averaged PV flux compared to the reference PV budget with Control forcing. SP and ST indicate subpolar and subtropical gyres, respectively.

Similar but smaller changes were observed for Experiment 2 in the upper-isopycnal layer (see Table 4.4). The wind-induced vorticity fluxes dropped by $2-7\%$, inter-gyre PV fluxes fell by 5% and

viscous boundary fluxes by $4-9\%$. In this situation however, changes in the inter-gyre PV flux are also no longer statistically significant under the same null hypothesis along with the change in tendency. PV budget changes in the middle-isopycnal layer appear to largely mirror the upper isopycnal layer except that the forcing is smaller due to only diabatic entrainment being present which is further weakened by the larger depth of the isopycnal layer.

Overall, our analysis shows that increased wind-forcing asymmetry decreases vorticity fluxes into the ocean gyres. The response of the ocean gyre circulation is consistent with a reduction in PV sinks across the gyres. This is achieved either through a drop in inter-gyre PV flux and/or a drop in viscous boundary fluxes where local restructuring of the WBL near the jet separation region is able to reduce normal relative vorticity gradients. We note that although the PV budgets are useful in capturing basin-integrated changes in the ocean gyres, more location-dependent circulation changes such as responses to western and eastern basin forcings are not well captured.

4.4.7 Summary of time-averaged ocean gyre responses to east-west vorticity flux anomaly dipoles

The ocean gyre response was found to be different according to the location of the vorticity flux anomaly in the ocean basin. Wind-stress curl anomalies in the western basin were associated with changes in relative strength of the inertial recirculation zones which consequently affected the jet-axis tilt. For example, a positive wind-stress curl in the western basin of upper-isopycnal layer was found to weaken the subtropical recirculation zone and strengthen the subpolar recirculation zone. This led to a relatively stronger subpolar gyre which pulled the eastward jet into a poleward tilt. This increases the baroclinicity of the subpolar recirculation zone and decreases the baroclinicity of the subtropical recirculation zone. This allows the subpolar recirculation zone to more efficiently transfer excess momentum into the lower layers due to increased anomalous PV flux. A similar but opposite pattern may be observed for the subtropical recirculation zone.

The wind-stress curl anomalies in the eastern basin on the other hand were found to affect the meridional position of the eastward jet extension. Our results with reduced wind-stress forcings in the

eastern basin led to reductions in the magnitude of the eastward jet meridional shift, while the recirculation zone strengths remained unchanged. The presence of westward-propagating waves from the eastern boundary which travel along the eastward jet confirmed the existence of baroclinic Rossby waves likely responsible for the meridional shift. These findings imply the presence of two distinct mechanisms of decadal ocean gyre variability (Dewar, 2003; Sasaki et al., 2013). Furthermore, the response of the ocean gyres seems to depend on the spatial location of the forcing.

4.5 Discussion

This chapter investigated the time-averaged response of the ocean gyres to wind-stress curl anomalies found in Chapter 3. These modes of atmospheric variability arise as a consequence of large-scale, standing Rossby wave disturbance growth and are hence relevant to the midlatitude climate variability. Although analysis in Chapter 3 found a statistical link between these modes of atmospheric variability and the delayed ocean gyre responses, it did not reveal enough about the nature of the dynamics and physical processes involved. Indeed, the complexity of the involved mode of atmospheric variability, which contains zonal asymmetries, and the two seemingly uncorrelated responses in the ocean gyres, at any time-lag, warranted further investigation.

The main finding of this chapter is the spatially-inhomogeneous response to wind-stress curl anomalies in the ocean basin. That is, wind-stress curl anomalies in the western and eastern ocean basins generate distinct responses in the modelled double gyre circulation. Although these two observed mechanisms of decadal ocean gyre variability are not new (see Dewar, 2003; Hogg et al., 2005; Berloff et al., 2007b; Sasaki and Schneider, 2011; Sasaki et al., 2013, for examples), the finding that both of these mechanisms act largely independently in the same modelled circulation is, to our knowledge, a new one[2]. Note that local restructuring of the WBL and changes in advective processes of the jet in Sasaki et al. (2013) are triggered by arrival of Rossby waves and are hence not independent processes.

The findings from our reduced eastern basin wind-stress curl experiments and the existence of Rossby

[2]We note here that these mechanisms are not entirely independent from each other since powerful advective effects of the inertial recirculation zones are able to disrupt the Rossby wave propagation along the eastward jet.

wave propagation along the eastward jet is crucial in showing that these two aforementioned mechanisms are distinct. For example, if it was true that the eastern basin forcing was important in determining recirculation zone strengths, then this should have been observed when the eastern basin forcing was reduced. Furthermore, the existence of wave-like behaviours along the eastward jet provided a means for the ocean gyres to respond to anomalous forcing which acts largely independently of the advection-dominated inertial recirculation zones. Our observation of propagating waves is potentially inconsistent with findings by Dewar (2003) where adjustment of the ocean gyres to anomalous wind-induced vorticity fluxes was unlikely to be caused by Rossby wave propagation. However, we believe this is likely due to the relatively small longitudinal ocean basin dimension (less than half the size of ours) which generates a double gyre circulation with an eastward jet that nearly reaches the eastern boundary. This means that any wind-induced Rossby waves are quickly broken up by the turbulence and powerful time-averaged advection of the eastward jet. The existence of Rossby waves in our modelled double gyre circulation is nevertheless still rather remarkable given the fact that our modelled jet is both stronger in its time-averaged transport and in its turbulent behaviour.

In summary, we believe the spatially inhomogeneous response of the ocean gyres to large-scale wind-stress anomalies depends on the time-averaged circulation itself. In regions where the time-averaged circulation is strong, i.e. the inertial recirculations and eastward jet extension, the response is dominated by advective effects and changes in the time-averaged circulation of those regions. Conversely, the presence of strong time-averaged circulation provides unfavourable conditions for the formation of wind-induced Rossby waves which are quickly broken up.

On the other hand, in regions where the time-averaged circulation is weak, i.e. in the eastern ocean basin, the conditions are now favourable for Rossby wave formation due to the largely stagnant flow in this region. Again, conversely, these regions also provide unfavourable conditions for advective processes to respond to anomalous forcing. Indeed, the only possible advective response is by gyre recirculations which are unlikely to be able to generate the measured eastward jet response since mixing and stirring effects dominate and lead to quick loss of PV memory by fluid parcels (Rhines and Schopp, 1991; Kurashina et al., 2021).

Although these modelled ocean gyre responses show some differences with Chapter 3, our findings

remain highly relevant and applicable. For example, the fact that our two upper-isopycnal ocean gyre responses are governed by distinct mechanisms is consistent with the lack of temporal correlations (at any time-scale) in the ocean gyre response modes from Chapter 3. Furthermore, the reduced predictability of these ocean gyre responses from Chapter 3 is well explained by the finding that both of these mechanisms involve regions of the ocean gyres where the effects of mesoscale turbulence are strong.

Parts of this chapter have been taken from Kurashina and Berloff (2022b), all of which is original work that has been conducted by the author.

Chapter 5

Western boundary layer nonlinear control of ocean gyres

5.1 Introduction

Although the previous chapters have looked at mechanisms that drive variability of the ocean gyres and the contained WBCs, eastward jet and inertial recirculations, they have not investigated the nonlinear dynamics that sustain the circulation itself. This chapter will focus on the effect of nonlinear dynamics in the WBCs that control important processes in the ocean gyres such as eddy backscatter and inter-gyre PV exchange.

5.2 Benchmark modelled ocean circulation

The ocean model used in this chapter differs from the previous chapters as it is adiabatic, i.e. fixed temperature, and uses a different advection scheme (Karabasov et al., 2009). However, the rest of the details of the model are very similar to the ocean-only configuration of Q-GCM. The model consists of a square box ocean with three stacked isopycnal layers and is driven by fixed winds. Since the model is adiabatic, there is no ocean mixed layer or diabatic entrainments modelled so it is driven

entirely by Ekman pumping in the upper-isopycnal layer. To avoid repeated information, the details of the model have been moved to Appendix A.3.

The benchmark ocean circulation is obtained by running for a 60-yrs with a 20-yr spinup period. Data was accumulated every day. Another linearised, Sverdrup ocean circulation with Munk boundary layer approximation is also computed with an set of identical parameters (see Appendix A.3 for linearisation).

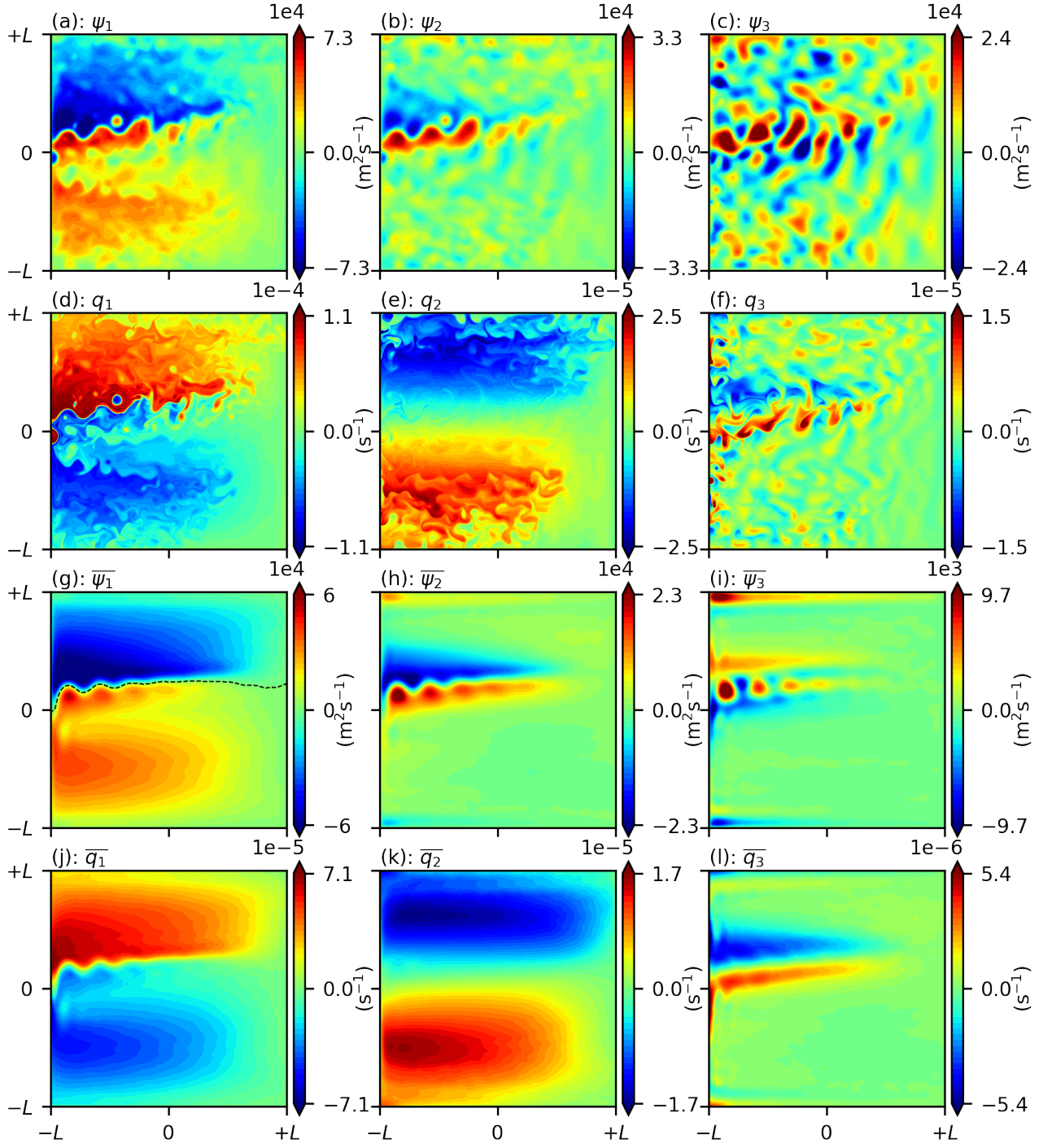

Figure 5.1: Reference solutions for the benchmark modelled double gyre circulation in statistical equilibrium. Panels from left to right show upper- to lower-isopycnal layers, respectively. Panels in the top-half of the figure show instantaneous fields and panels in bottom-half show time-averaged fields. (a - c): Instantaneous ocean transport streamfunction. (d - f): Instantaneous ocean PV anomaly. (g - i): Time-averaged ocean transport streamfunction fields. (j - l): Time-averaged ocean PV anomaly fields. Inter-gyre boundary, shown in (g), is defined by the time-averaged contour emanating from the western boundary.

We present typical snapshots and time-averaged solutions of system (A.7) in Fig. 5.1. The modelled ocean circulation is qualitatively very similar to those shown in Chapters 3 and 4. This is largely due to the very similar parameter choices made in the model (see Table A.2).

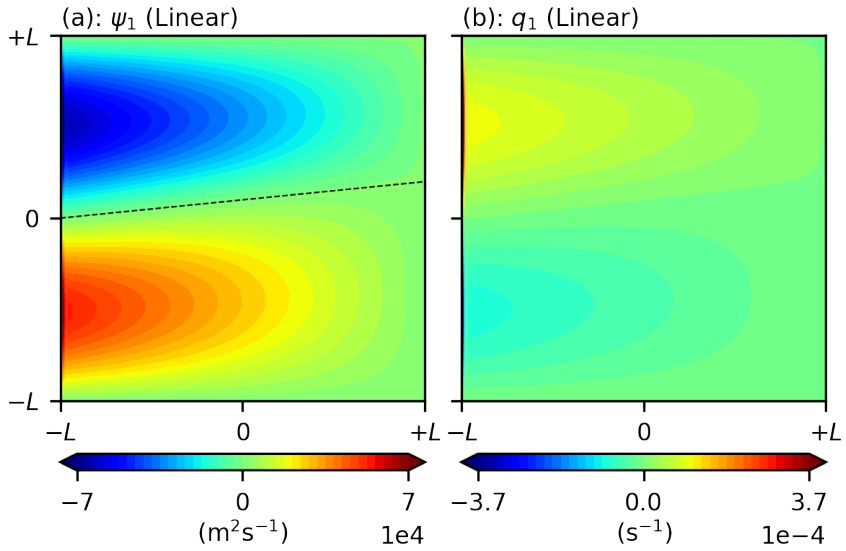

Figure 5.2: Reference solutions for linearised system (A.11) in the upper-isopycnal layer. Inter-gyre boundary in (a) is defined in the same manner as discussed in the caption of Fig. 5.1.

Fig. 5.2 shows that the Sverdrup (i.e., linear) gyres and WBCs in the upper-isopycnal layer are present but differ from the nonlinear-dynamics solutions. Furthermore, nonlinear phenomena such as the eastward jet and recirculation zones are missing. Contour plots for the lower layers are omitted as these only show the gravest basin modes propagating across the basin. This is because the eddy forcing that drives the lower layers (Holland, 1978) is no longer present.

5.3 Influences of nonlinear dynamics on the ocean gyres

5.3.1 The nonlinear western boundary layer

The differences in structure of the upper-layer WBL are particularly significant when inspecting Figs. 5.1g,j and Figs. 5.2a,b. Fig. 5.2b shows much stronger zonal PV gradients near the western boundary which are accompanied by increased meridional velocities in the region. Typical time-averaged meridional velocities for system (A.7) are $1\,\mathrm{ms}^{-1}$, while they are up to $4\,\mathrm{ms}^{-1}$ for system (A.11). This

implies a cutting down of high velocity and vorticity in the WBL through nonlinear effects. Indeed, Veronis (1966a) also showed through a perturbation analysis that this restructuring of the WBL is likely due to the meridional inhomogeneities in the structure of the wind-forcing and ocean gyres. Furthermore, they showed that this restructuring is controlled by effects of PV advection. However, it is unclear what processes maintain the structure of the WBL after the assumptions of the stability analysis break down. A full analysis of the advection term in (A.7a) is required to understand this which is outside the scope of this chapter. Reduction of WBC velocities also indicates that the nonlinear-dynamics solutions will also show a decrease in viscous relative vorticity fluxes through the western boundary in comparison to the linear-dynamics solutions (Spall, 2014, see also Subsection 5.3.3). We now continue our analysis by defining the counter-rotating gyre anomalies (CGAs) through a solution decomposition.

5.3.2 Solution decomposition

The CGAs, as well as other nonlinear circulation features, are defined by decomposing the nonlinear-dynamics solutions into the linear-dynamics (subscript 'lin'), time-averaged advection-induced nonlinear anomalies (subscript $\oplus$) and transient fluctuations (primed):

$$\psi_i = \overline{\psi}_{i,\mathrm{lin}} + \overline{\psi}_{i,\oplus} + \psi_i', \tag{5.1}$$

for layers $i = 1,2,3$ (see Shevchenko and Berloff (2016) for identical decomposition). Note that the time-averaged streamfunction is given by $\overline{\psi}_i = \overline{\psi}_{i,\mathrm{lin}} + \overline{\psi}_{i,\oplus}$. This process is also repeated for PV anomalies. We choose this particular decomposition as we want to highlight the regions where the discrepancy between the nonlinear-dynamics solutions, i.e., system (A.7), and linear-dynamics solutions, i.e., system (A.11), is greatest. This then allows us to pinpoint regions where nonlinear effects are particularly strong, which will guide our analysis in later sections. Comparisons of the nonlinear-dynamics against the linear dynamics have been used in the past to study recirculation zones and eastward jets (e.g. Veronis, 1966a; Harrison and Stalos, 1982), and we will be utilising the same technique for the CGAs.

The time-averaged advection-induced anomalies (Fig. 5.3a,b) reveal the recirculation zones on either side of the eastward jet, and the sharp zonal PV anomaly gradients near the western boundary that extend out into the gyre interiors. The CGAs are seen embedded in the subpolar and subtropical gyres as opposite-signed, anti-cyclonic and cyclonic anomalies, respectively. We stress here that since the CGAs are defined as a deviation from the linear-dynamics solutions, they would not necessarily be visible in observations/models without this particular solution decomposition. However, we will show that these anomalies are dynamically important and linked to mechanisms which control the double gyre circulation.

Upon further inspection of these anomalies, we see that they are, in fact, two separate lobes (see Fig. 5.3f). The first lobe, which is by far the stronger anomaly, is situated within the viscous sublayer (VSL) of the WBLs. We will refer to this lobe as the 'WBL lobe' for brevity. The second lobe, which is a much weaker but larger-scale anomaly, is spread throughout the western half of each gyre interior. This lobe will be referred to as the 'interior lobe'. Why the CGAs are separated into two separate lobes and the influences of nonlinearity in this regions on the global circulation is still not fully known.

For the lower layers, the equivalent plots for Fig. 5.3 are seen by observing Figs. 5.1h-l. This is because the lower layers are essentially stagnant for the linear-dynamics solutions. Inspecting these plots, we see that the recirculation zones are visible in the lower layers but no CGA-like patterns are present. Thus, we conclude that the CGAs are confined to the upper-isopycnal layer, which is the only layer driven directly by wind-stress curl.

Shevchenko and Berloff (2016) found that by strengthening the CGAs via an external forcing term, the eastward jet was weakened. But, they did not analyse in detail the associated dynamics. We continue our analysis of the CGAs by examining the relative vorticity fluxes at the western boundary, where the time-averaged advection-induced anomalies are strongest.

5.3.3 Excess PV buildup

To better understand how nonlinear effects adjust the large-scale circulation in the upper-isopycnal layer, we calculate PV budgets for both the linear- and nonlinear-dynamics solutions. A similar budget is computed in Berloff et al. (2007b), albeit with different model configurations. The sources and sinks of PV in the upper-isopycnal layer are considered below and PV fluxes are estimated and given in Table 5.1. The terms of the PV budget are very similar to the terms obtained in the PV budget for Q-GCM (see Subsection 2.3.2), so their description is omitted to avoid repetition. Note the inter-gyre viscous fluxes are included here for the linear-dynamics solutions but their contribution is still relatively small.

PV flux from	Linear-dynamics solutions	Nonlinear-dynamics solutions
Wind	-1.060 $(+1.319)$	-0.938 $(+1.197)$
Viscous boundary flux	$+1.059$ (-1.319)	$+0.176$ (-0.254)
Inter-gyre PV flux	N/A	$+0.828$ (-0.828)
Inter-gyre viscous flux	Negligible	$+0.003$ (-0.003)
Tendency	Negligible	-0.069 $(+0.111)$

Table 5.1: PV budgets for linear- and nonlinear-dynamics solutions for the subtropical gyre in the upper-isopycnal layer $(\mathrm{m}^2\mathrm{s}^{-2})$. Bracketed values are identical computations made for the subpolar gyre. Terms that account for $< 0.05\%$ of the budget are deemed as negligible. We found that the PV budget was largely insensitive to small changes made in the inter-gyre boundary.

Since the WBL lobes of the CGAs consist of strong advection-induced PV anomalies in the WBL, we expect a reduction in the zonal relative vorticity gradients near the western boundary, which is confirmed in Fig. 5.4. Indeed, this leads to $> 80\%$ reduction in viscous boundary fluxes (Table 5.1), which is balanced by the inter-gyre PV fluxes. The sign change in advection-induced PV anomalies at the western boundary does not increase the magnitude of relative vorticity in this region, but instead reduces it, as there is also a corresponding sign change in relative vorticity near the western boundary. This then leads to a reduction in viscous boundary fluxes, as they are governed by normal derivatives of relative vorticity.

These results are consistent with those made by Cessi et al. (1987) and Kiss (2002), where there should be a larger loss of PV. Cessi et al. (1987) showed that the excess PV then drives the recirculation zones, and Kiss (2002) argued that this effect may also be involved in the WBC separation. Our

results differ from these studies, as we have used a double gyre, rather than a single-gyre model. This gives the model an extra mechanism to remove excess PV, which is through the inter-gyre PV fluxes downstream of the WBCs.

The extent to which the CGAs are consistent with a linear response to the geometric wind effect[1] is checked by reducing the wind-stress amplitude τ_0 by 20%[2]. This is to mimic the impact of the geometric wind effect on wind-curl fluxes for each gyre. We will see from the results of this experiment that even by overestimating the impact of the geometric wind effect, the linear response alone is not strong enough. Relative vorticities, rather than PV anomalies, are used to show the linear response, as they determine the viscous boundary fluxes. Fig. 5.5a shows anti-cyclonic and cyclonic anomalies situated within the subpolar and subtropical WBLs, respectively, similar, in shape, to the WBL lobe of the CGAs seen in Fig. 5.3f. Furthermore, Fig. 5.5b shows a weaker, second lobe similar to those observed in Fig. 5.3b. However, the linear response to reduced wind-curl input in the ocean interior is basin-wide, rather than being confined to the western half of the gyres. This implies that the shape of the CGAs is consistent with a linear response to the geometric wind effect but this alone cannot account for the nonlinear-dynamics anomalies, which are significantly stronger. Indeed, the linear response only accounts for $\sim 15\%$ of the viscous boundary flux reduction drop, which may also be seen by comparing the PV budgets of the linear- and nonlinear-dynamics solutions (Table 5.1).

The separation of the two lobes of the CGAs (Fig. 5.3) also suggests that the mechanisms that drive these circulation features are unlikely to be the same. To confirm this, we produced scatter plots of PV anomalies against the velocity streamfunction (see Fig. 5.6). In the interior lobe, we see a functional (nearly linear) relationship between PV anomaly and velocity streamfunction values, implying the formation of Fofonoff-type gyres (Fofonoff, 1954). However, in the WBL, the effects of friction make the above mentioned relationship unfeasible.

Examining the inter-gyre PV fluxes in Table 5.1, we see they take up a considerably larger proportion of the PV budget compared to Berloff et al. (2007b). This is attributed to the much smaller eddy-viscosity parameter and a boundary condition parameter choice which creates a more turbulent double

[1]The geoemtric wind effect is the misalignment of the zero wind-curl line and the eastward jet extension that leads to a reduction in wind-curl flux into the ocean gyres.

[2]We define the linear response to the geometric wind effect as the difference between the time-averaged linear-dynamics solutions for 80% and 100% wind-stress amplitudes, respectively.

gyre circulation. Since higher inter-gyre PV fluxes are directly associated with stronger advection-induced anomalies in the WBL, we expect CGAs to only become observable in more nonlinear and turbulent double gyre circulation. Along with the drop in viscous boundary fluxes, the inter-gyre PV flux increase accounts for the largest changes in the PV budget for the linear- and nonlinear-dynamics solutions.

In order to understand the chain of events that leads to both the viscous boundary flux reduction and increase in inter-gyre PV fluxes, we performed a numerical experiment, where we solved system (A.7), but using the time-averaged solution to system (A.11) as the initial condition. This may be interpreted as a 'switching on' experiment where nonlinear dynamics are suddenly turned on in a linear-dynamics flow regime. Such experiments are useful as they give an indication into the nonlinear dynamics that maintain the ocean gyre circulation. What we would expect to see is the time-averaged linear-dynamics solution (Fig. 5.2) to converge towards the nonlinear-dynamics solutions (Fig. 5.1), thus, leading to the adjustments in the PV budgets observed in Table 5.1. The time scales associated with these adjustments can help us to identify the likely causal chains taking place. For example, it may be the case that viscous boundary flux reductions, induced by the nonlinear boundary layer, create a PV accumulation which must be rectified by the inter-gyre PV fluxes. Then, we would expect the time scale of this PV budget adjustment in our experiment to be of WBC advective time scales $T_{\text{wbc}} \sim L/U \approx 11\,\text{days}$, where L is the basin length scale and $U = 2\,\text{ms}^{-1}$ is the WBC velocity scale. Alternatively, the uptake in inter-gyre PV fluxes could reduce PV concentrations within each gyre which then reduce the viscous boundary fluxes. If this were the case, then we would expect to see the PV budget adjustment to take place over gyre recirculation time scales $T_{\text{gyre}} \approx O(1\,\text{yr})$. We found that the viscous boundary flux adjustment took place over an extremely short time frame ($\sim 20\,\text{days}$), which indicates that it is the WBC advective time scales which are important in the PV budget adjustment. Hence, it is likely that the nonlinear boundary layer is inducing PV accumulation within the VSL, which must be rectified downstream by the inter-gyre PV fluxes.

To summarise, the shapes of the CGAs are consistent with the linear, weakened wind-curl response created by the geometric wind effect. But this cannot account fully for the CGAs, as the linear response by itself is too weak without considering nonlinear effects. In the interior lobe, we see the formation of Fofonoff-type gyres which arise in nonlinear free-flow situations. On the other hand, in

Ensemble statistic	Subtropical gyre	Subpolar gyre
Total released	6221 (7891)	6659 (5022)
Migration count	1341 (579)	2365 (579)
Migration %	19.7 (7.3)	35.5 (11.5)
Averaged outgoing q' ($10^{-5}\,\mathrm{s}^{-1}$)	-1.3 (-1.7)	$+1.5$ ($+1.0$)

Table 5.2: Ensemble statistics obtained from Lagrangian particles seeded in VSLs of the subtropical and subpolar gyres. Numbers in brackets are results obtained from seeding particles randomly within the corresponding gyre. Ensemble-averaged PV fluctuations were obtained for migrating particles only and measured at first crossing of the buffer zone (see text for more details).

the WBL nonlinear effects reduce zonal relative vorticity gradients near the western boundary, and this severely inhibits the ability of the WBCs to dissipate PV through viscous boundary fluxes. This creates a growing PV imbalance which is only rectified downstream by the inter-gyre PV fluxes. We conclude that this rectification of the PV imbalance must be controlled by an inter-gyre PV exchange mechanism. Such inter-gyre mechanisms are not new, e.g., Yang (1996) and Coulliette and Wiggins (2001) have studied inter-gyre transports before. However, the link between insufficient PV loss in the VSLs and inter-gyre exchanges of PV has not been made. A similar link between anomalous PV generated in the WBL driving the corresponding recirculation zone has been made before (Cessi et al., 1987), but this mechanism acts to strengthen the ocean gyres, rather than to weaken them. In the next section, we will switch to a Lagrangian framework which is more suited to identify the underlying mechanism, as well as to confirm hypotheses made in this section.

5.4 Lagrangian particle analysis

Since the suspect inter-gyre PV exchange necessarily requires long-range transport of PV, a Lagrangian particle analysis is well-suited to identifying the mechanism responsible. Are fluid parcels within the VSLs statistically biased to permanently migrate between the gyres? What are the inter-gyre gateways, if they exist, and is there a measurable PV advection taking place? We investigate these questions via a Lagrangian particle analysis, which is described in details in the following section.

5.4.1 Experiment design

We released $N = 400$ particles randomly positioned within the VSL of the upper-isopycnal WBC in 60-day intervals. The VSL was chosen as this is the region where the PV accumulation has been found to be occurring (Lozier and Riser, 1989; Kiss, 2002). We define the VSL width to be the perpendicular distance from the western boundary at which the plane parallel to the western boundary gives zero viscous boundary fluxes for each gyre. This coincides with the zonal gradient of relative vorticity profiles changing signs, which we found to be ~ 15 km (see Fig. 5.4). Particles were advected for a period of 8-yrs, with a total of 10 releases. This was repeated for the 4 sets of 10-yr model runs computed for the reference doube-gyre circulation in statistical equilibrium. The particle evolution time length of 8-yrs was chosen, because it allows particles on average to make one complete gyre circuit, regardless of where a particle was seeded. Seedings were made up to 7.5 km away from the western boundary, well within the VSLs, which are about two grid cells wide. The total number of particles that permanently migrated from one gyre to the other after the evolution period were compared to the total number released in that gyre. Using the inter-gyre boundary by itself is unsuitable for this task as this produces false identifications when checking which gyre the particle is positioned in. This is due to the high variability of the eastward jet position which will regularly diverge from its time-averaged position. In order to remedy this, we introduced a buffer zone of 450 km on either side of the inter-gyre boundary, which particles must cross for the particle to be flagged as 'migrated'. Small adjustments of the width of the buffer zone did not significantly affect any of our results. This experiment was repeated with particles seeded randomly within the ocean interior, which acted as our control case. For Lagrangian particles that migrated over to the opposite gyre, their total PV is approximated using a 2D cubic spatial interpolation at each time step. This experiment differs from Berloff et al. (2002), where a more general analysis of mixing/stirring processes within different regions of the ocean gyres was considered in order to develop stochastic parametrisations. The analysis in this chapter is more specific as we are attempting to link insufficient PV dissipation in the VSLs with inter-gyre PV exchanges.

5.4.2 Results

For particles seeded in both the subtropical and subpolar VSLs, we found that they were $2-3$ times more likely to permanently migrate between the gyres than when particles were seeded in the gyre interiors (Table 5.2). Such an increase in migration rate is statistically significant, indicating that there are active inter-gyre pathways from the VSLs to the opposite gyre. Table 5.2 shows that after migration the ensemble-average behaviour of the particles is to advect transient PV fluctuations which are opposite-signed to that of the gyre. The transient PV fluctuation of the i-th Lagrangian particle after migration is taken by measuring $q'(t_i, x(t_i))$, where t_i is the first crossing time of particle i. This confirms that there is an inter-gyre PV exchange mechanism taking place, as the PV values are measured well outside the eastward jet extension region and recirculation zones, where the eddy backscatter mechanism is predominantly active (Berloff, 2016) and may possibly work against the inter-gyre PV exchange. The existence of this mechanism allows for the correction of the PV imbalance created in the WBL. Table 5.2 also indicates that the PV fluxes are larger from the subpolar gyre than the subtropical gyre, which is consistent with the reductions in viscous boundary fluxes in Table 5.1 for each gyre. The total PV of migrating particles seeded randomly within each gyre also indicate that transient PV fluctuations are being advected from the gyre interiors. However, upon further inspection of these trajectories, we found that these particles had entered the WBL and then migrated gyres.

Although the inter-gyre PV exchange mechanism is active for both gyres, the qualitative behaviour of associated particle trajectories is asymmetric. For example, particles released in the subtropical VSL (see Fig. 5.7) tend to migrate through the eastern half of the eastward jet where it is weakest and where there are time-averaged PV fluxes between the gyres (Fig. 5.8a). Then, the migrated particles remain trapped in the eastern half of the gyre, away from the CGAs up to 500 days after seeding. This indicates that any excess PV from the VSL is lost through diffusive processes long before they reach the interior lobe of the CGAs. Hence, the interior lobes of the CGAs remain unlikely to be a consequence of the inter-gyre PV exchange, but rather, the formation of Fofonoff-type gyres.

For particles released in subpolar VSL (Fig. 5.9), instead of only being able to migrate between the gyres near the eastern boundary, particles are able to migrate across the entire length of the jet via the shedding of mesoscale eddies (see Fig. 5.8b). This allows migrating particles to initially mix

more quickly in the subtropical gyre (see Figs. 5.7c and 5.9c), due to the increased number of inter-gyre gateways. After 250 days, the migrated particles have already begun to leave the subtropical recirculation zone and enter the interior gyres. However, once again, the majority of these particles remain trapped in the eastern half of the gyre until the end of the advection period. These results are consistent with observations made in Rhines and Schopp (1991) where a loss of 'memory' of material properties occurs in similar regions of the ocean. This suggests that the reverse situation to our hypothesis, i.e., inter-gyre PV exchange reducing viscous boundary fluxes at the western boundary is unlikely to be the case, as seen from our Lagrangian perspective on the dynamics.

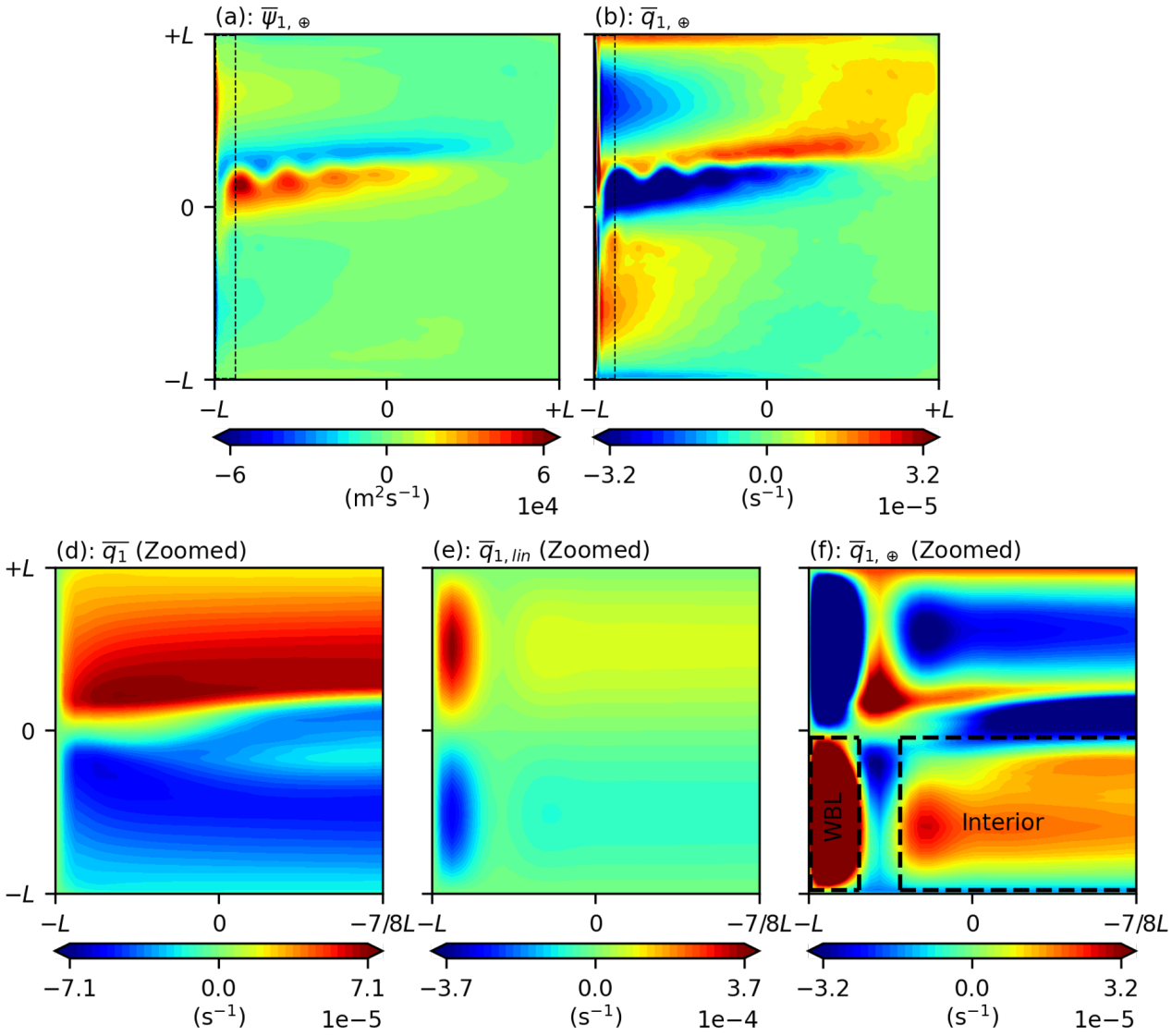

Figure 5.3: Time-averaged advection-induced anomalies in the upper-isopycnal layer for double gyre circulation in statistical equilibrium. (a): Velocity streamfunction. (b): PV anomaly. Box surrounded by black dotted lines indicates region near western boundary plotted in (d - f). Areas that contain the subtropical WBL and interior lobes of the CGAs are marked out by dotted lines in (f). Note that the interior lobe extends further outside of (f) into the ocean interior. Panels (b, f) are also saturated to better show anomalies in ocean interior.

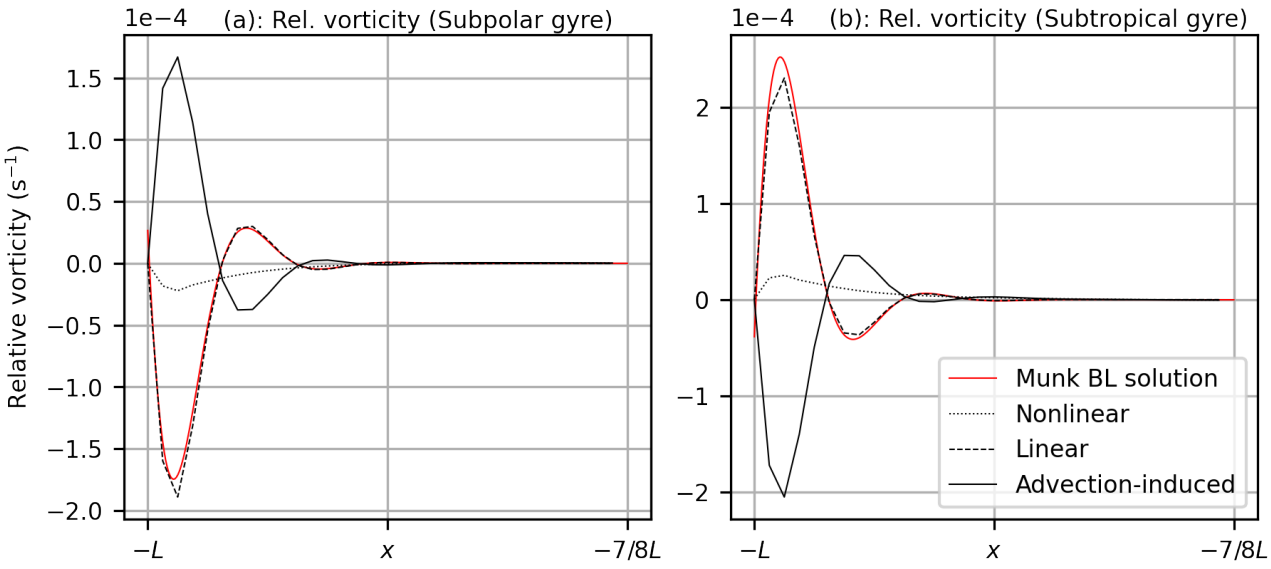

Figure 5.4: Time-averaged relative vorticity profiles near the western boundary of linear- and nonlinear-dynamics solutions, and advection-induced anomalies. The generalised Munk boundary-layer solution (see Appendix of Kurashina et al., 2021) is added to compare with the linear-dynamics solution. Profiles have been meridionally averaged over (a) subtropical gyre, (b) subpolar gyre.

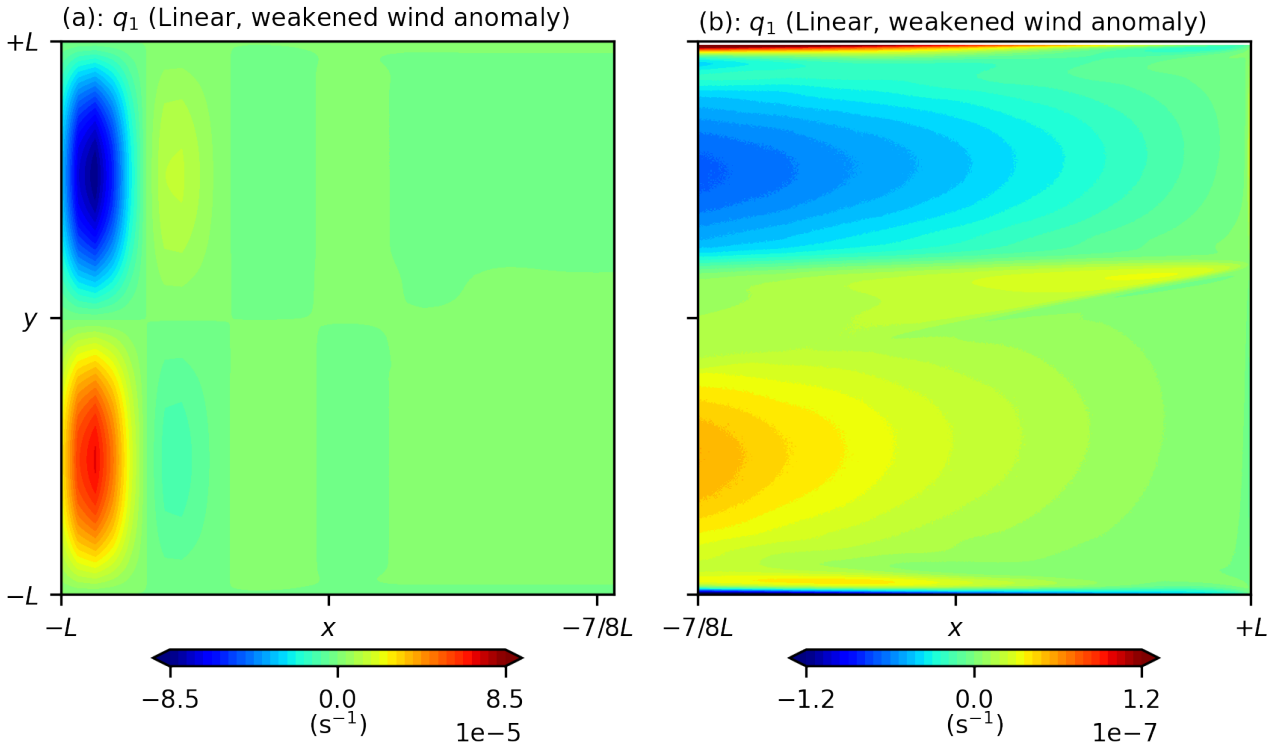

Figure 5.5: Time-averaged, linear, weakened wind-curl response for relative vorticities in the upper-isopycnal layer. Left and right panels show the ocean basin partitioned into (a): Western boundary and (b): Ocean interior regions.

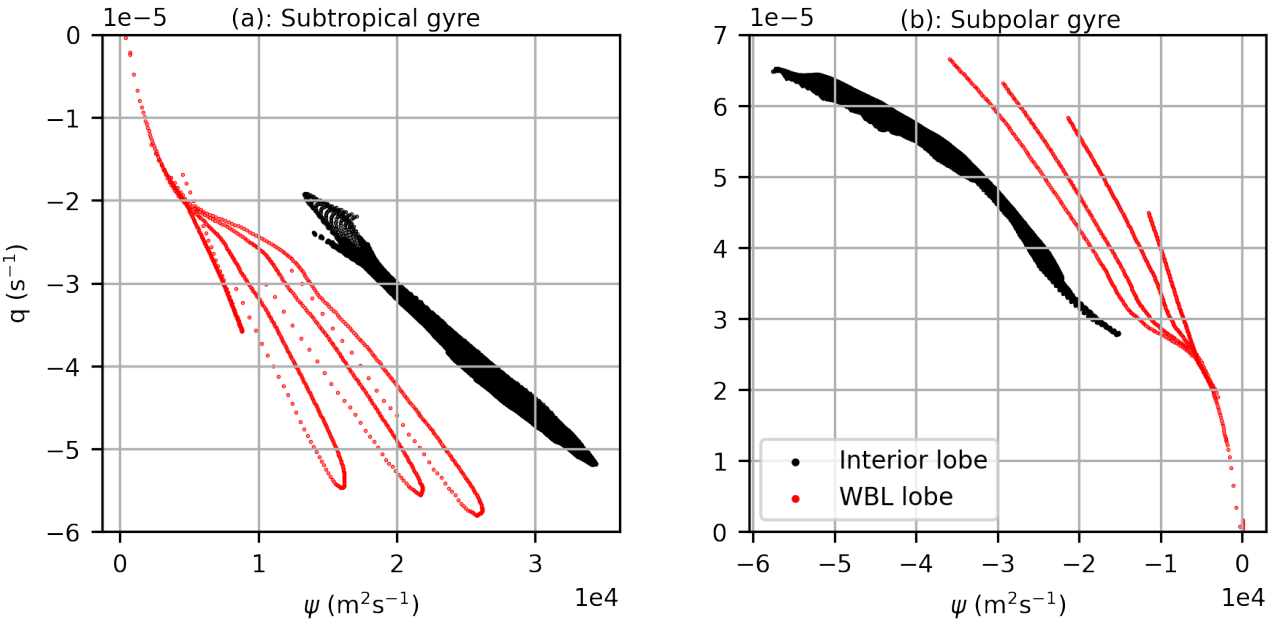

Figure 5.6: Scatter plots of PV anomalies against velocity streamfunction for grid points in the interior and WBL lobes of the CGAs: (a) subtropical gyre, (b) subpolar gyre.

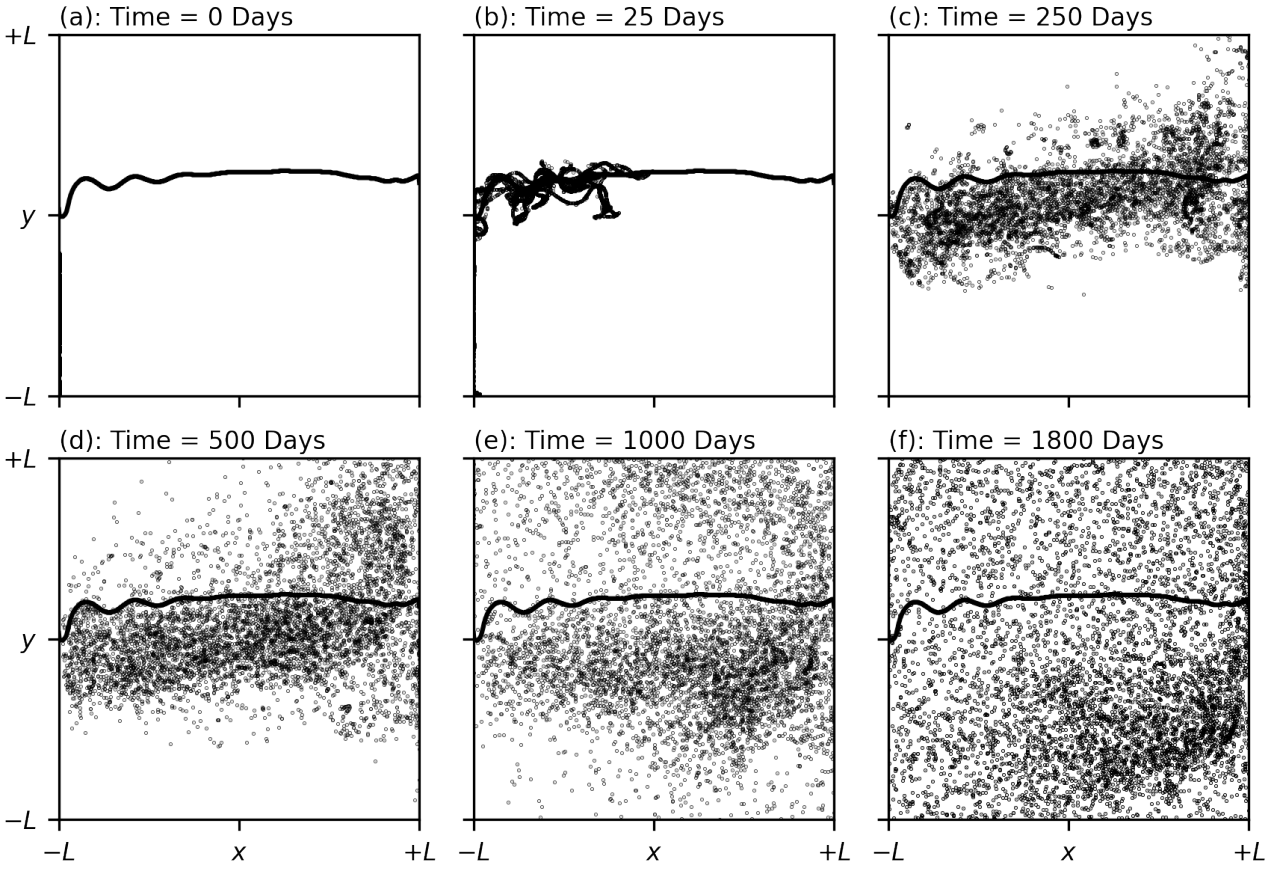

Figure 5.7: Ensemble distribution of Lagrangian particles in the upper-isopycnal layer at $t = 0, 25, 50, 250, 500$ and 1800 days. Particles were seeded in the VSL of the subtropical WBC.

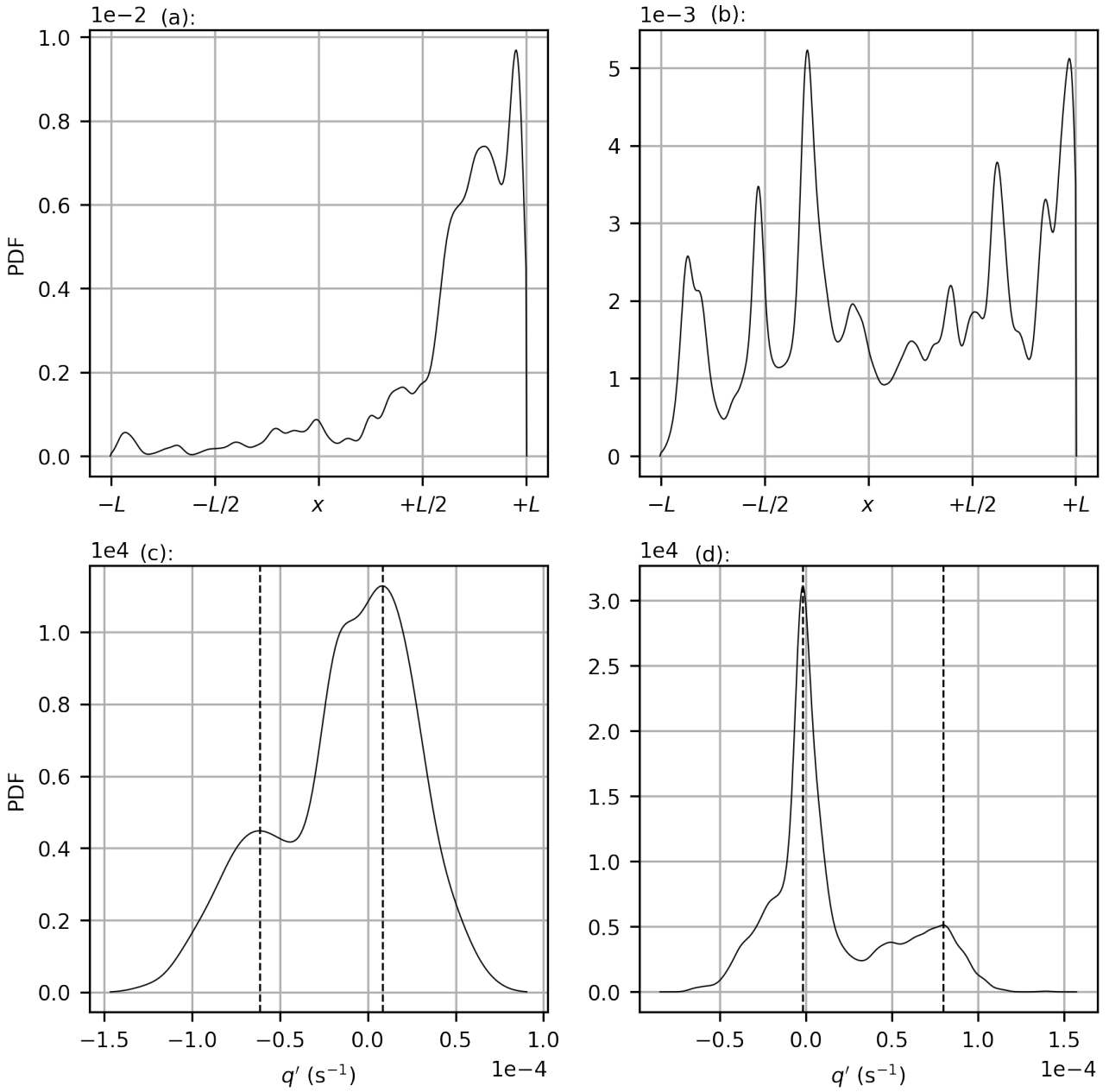

Figure 5.8: Top panels show PDFs of longitude measured at first crossing time of the buffer zone for seedings in: (a) subtropical, and (b) subpolar VSL. Bottom panels show PDFs of transient PV fluctuations measured at first crossing time of the buffer zone for seedings in: (c) subtropical, and (d) subpolar VSL. Dashed lines indicate the locations of the peaks of transient PV fluctuations. PDFs are obtained using kernel density estimators with data gathered through ensemble trajectories. Gaussian kernels have been used and the optimal bandwidth is found using cross-validation techniques. Small adjustments of buffer-zone width did not significantly affect the shapes of the distributions.

It also appears from our experiments that the eastward jet extension is more permeable in the anti-cyclonic direction. That is, there are more active inter-gyre pathways from the subpolar to subtropical gyre, as compared to the reverse direction. Furthermore, inter-gyre pathways from the subpolar to subtropical gyre exist across the entire jet extension. While on the other hand, inter-gyre pathways from the subtropical to subpolar gyre are limited to the eastern portion of the jet. To our knowledge the shapes of distributions in Fig. 5.8a,b has not been observed before. We believe this is because the Lagrangian particle longitudes are measured at the first crossing of the buffer zone, rather than at the inter-gyre boundary (e.g. Berloff et al., 2002). Such asymmetric behaviour indicates that inter-gyre PV fluxes from the subpolar to the subtropical gyres are generated more strongly through the action of mesoscale eddies while the reverse case takes place through the time-averaged PV fluxes. We theorise that this effect is due to the geometric wind effect which is largely situated over the subtropical recirculation zone. This leads to the wind-curl fluxes to act as a PV sink over this region, while it remains a PV source over the remainder of the ocean basin. A PV sink acting over the recirculation zones implies a weakening of the subtropical recirculation zone which may increase the likelihood of migration from the subpolar VSL.

Figs. 5.8c,d show the distribution of transient PV fluctuations measured after migration. For seedings in both VSLs, there is a clear double-peak pattern visible. The larger peak consists of particles which have already removed their excess PV, while the smaller peak consists of particles that are still holding excess. This double-peak distribution is expected to eventually merge into a single-peak distribution as migrating particles have their PV homogenised by the ocean gyres. We confirmed this by checking the PV of migrating particles at the end of the evolution period and found that this was the case. Indeed, the distribution in Fig. 5.8c appears closer to reaching its long-time limit. We believe this is due to the longer time scales associated with the migration from the subtropical VSL.

Although the differences in behaviour of the migrating particles from each VSL are notable, the particles that do not migrate between the gyres behave largely the same. These particles enter the downstream recirculation zones where they advect excess PV from the VSLs. Once inside, the particles backscatter and strengthen the eastward jet (Cessi et al., 1987; Nakano et al., 2008).

Particles seeded randomly within the ocean interior (Figs. 5.10, 5.11) largely remain trapped within

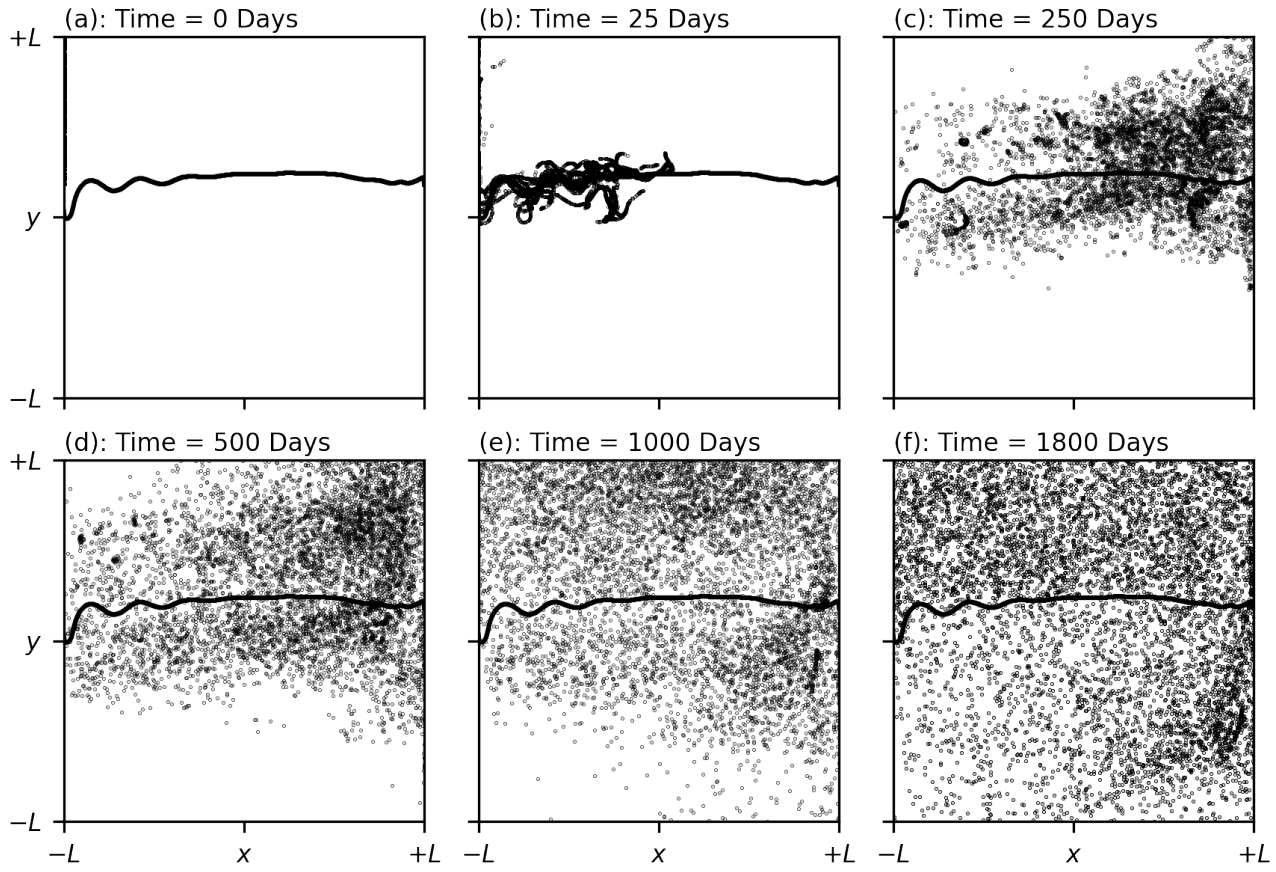

Figure 5.9: The same as Fig. 5.7 but for Lagrangian particles seeded in the VSL of the subpolar WBC.

their respective gyres. This indicates that particles seeded here are not responsible for the inter-gyre PV exchange mechanism seen in Figs. 5.7 and 5.9.

The results of seeding in the VSLs show that an inter-gyre PV exchange mechanism is active, but that this mechanism is not responsible for the interior lobe of the CGAs. This again is consistent with our previous hypothesis that the interior lobes are due to the formation of Fofonoff-type gyres which must be distinct from the PV exchange mechanism. To confirm that the interior lobes are not generated by the inter-gyre PV exchange mechanism, we seeded Lagrangian particles in the interior lobe of the CGAs and advected the particles, but reversed in time. We found that particles seeded in the interior lobe regions were not statistically biased to originate from the opposite gyre and behaved similarly to particles seeded in the ocean interior.

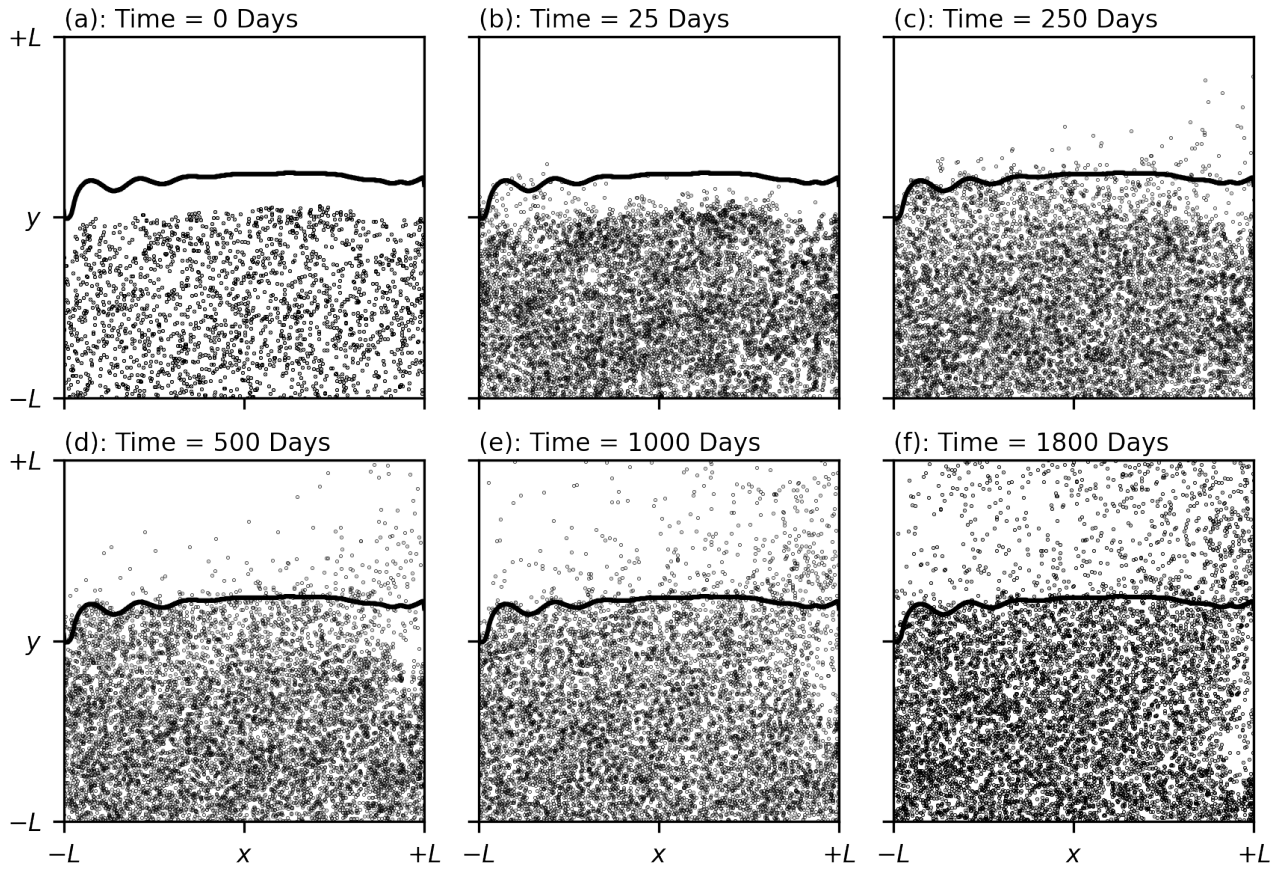

Figure 5.10: The same as Fig. 5.7 but for Lagrangian particles seeded randomly in the subtropical gyre.

5.4.3 The inter-gyre PV exchange mechanism

The inter-gyre PV exchange is described by following an ensemble of Lagrangian particles released in the subpolar VSL (see Fig. 5.12 for a schematic):

1. The nonlinear western boundary layer reduces viscous boundary fluxes through effects of PV advection. This leads to an accumulation of PV within the VSLs.

2. Particles now move downstream where they enter the eastward jet. The majority of these particles then enter the recirculation zone where they fortify the eddy backscatter.

3. The remainder of these particles migrate permanently to the opposite gyre, where they are able to rectify the PV imbalance created in (1).

4. Particles enter the Sverdrup-gyre circulation in the eastern half of the basin. By the time they

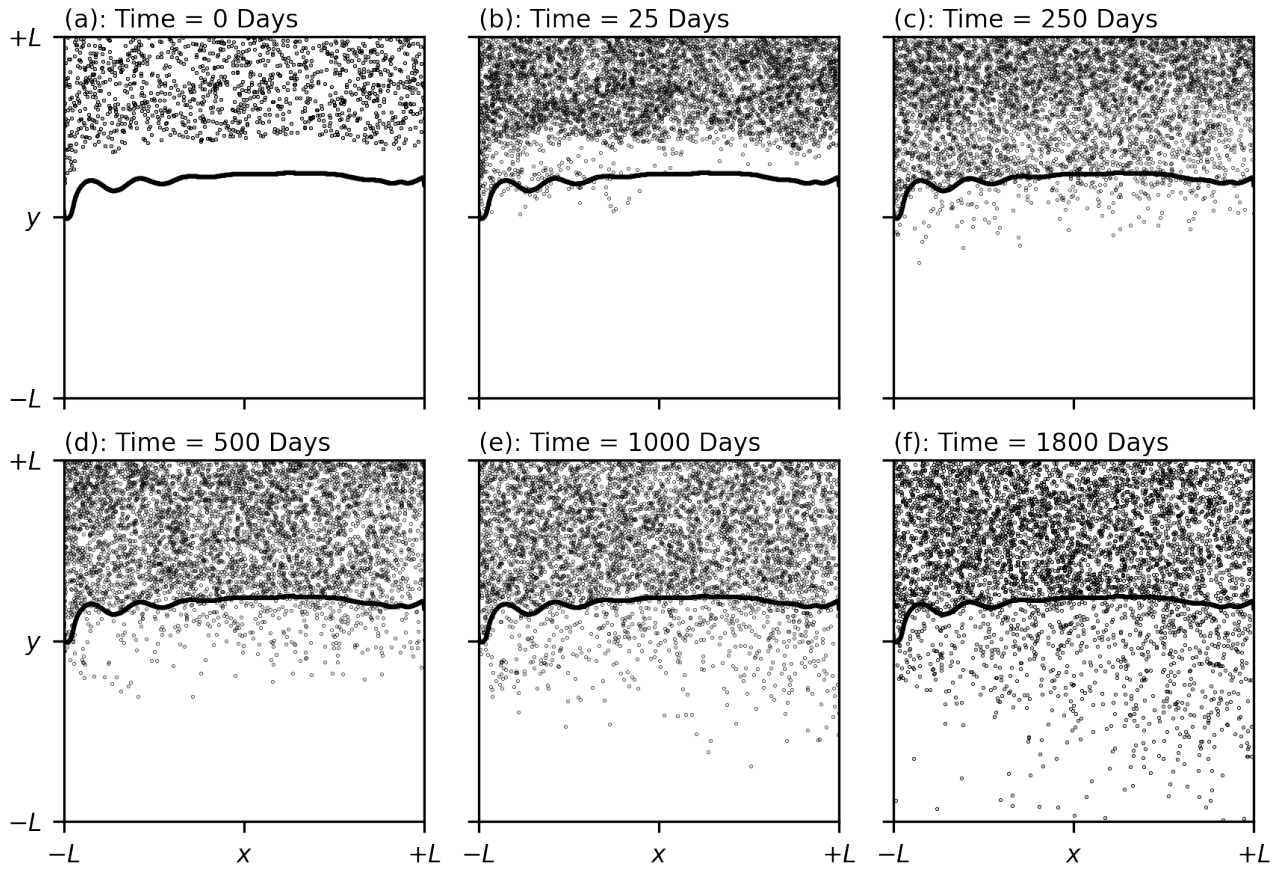

Figure 5.11: The same as Fig. 5.7 but for Lagrangian particles seeded randomly in the subpolar gyre.

reach the WBCs, they have already acclimatised to the background flow and the process is repeated.

5.5 Summary and discussion

Before we move onto a discussion of the main findings in the chapter, we acknowledge that it is difficult to completely diagnose the effects of nonlinear dynamics in the ocean gyre circulation. This is due to the nature of nonlinear dynamics itself, rather than the analysis which we believe is comprehensive and robust. Given the presented evidence from our analysis, the findings below are our best explanation for what we believe is occurring in the modelled circulation. Indeed, every stage of our analysis has, so far, been consistent with our proposed theory.

In this chapter, we examined the impacts of nonlinear dynamics in the WBLs on the classical wind-

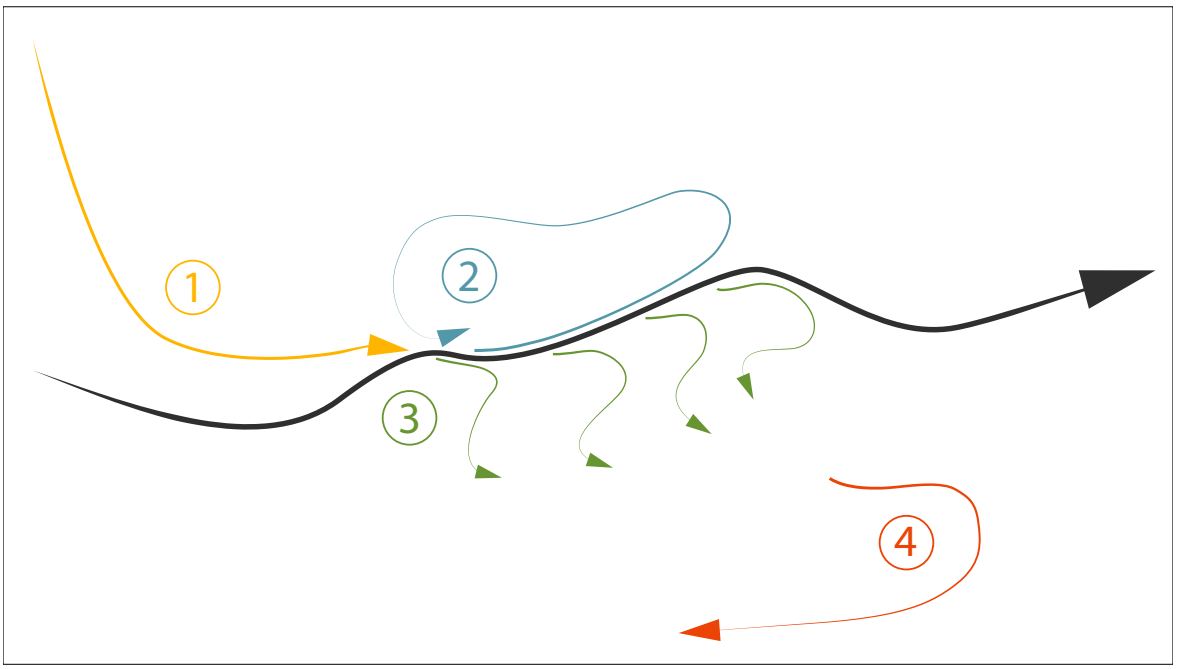

Figure 5.12: Schematic of inter-gyre PV exchange mechanism. Curved black arrow represents the eastward jet extension. Coloured arrows indicate orientation of mass fluxes associated with PV exchange mechanism, each colour and number represents a step of the mechanism described in Section 5.4.3. 1. Fluid parcels in the VSL lose insufficient PV through the western boundary. 2. The majority of these fluid parcels then enter the recirculation zones where they backscatter. 3. Remaining fluid parcels migrate across the eastward jet extension where they close the PV budget. 4. Migrated particles get acclimatised to the background PV in the mid-ocean.

driven double gyre circulation. Much of the analysis was motivated by the nonlinear circulation features known as CGAs, which have only been discovered relatively recently (Shevchenko and Berloff, 2016), but we found our results are more far reaching. Such studies of the WBCs are frequent in the literature (e.g. Lozier and Riser, 1989; Haidvogel et al., 1992; Berloff and McWilliams, 1999b) and studies of the linear dynamics are even more so. However, the recent advances in simulating more realistic, turbulent QG double gyre circulation, and effective use of Lagrangian particle analysis have revealed unique insights.

Initial analysis of the CGAs showed that they are split into two separate lobes. The first lobe, consisting of stronger advection-induced anomalies, lies close to the boundary within the VSLs of the WBCs. The second lobe is weaker in strength, but spreads throughout the western half of the gyre. The WBL lobe was found to be created by nonlinear adjustment of the WBL, leading to the widening and deceleration of the WBC. This result was consistent with Veronis (1966a,b) where the WBL restructuring was found to be induced by PV advection. Consequently, this led to a significant viscous

boundary flux reduction at the western boundary, as predicted by the theory in Spall (2014). This flux reduction led to an accumulation of PV, and hence enstrophy within the ocean gyres, which must be removed downstream via an inter-gyre PV exchange mechanism. Indeed, a similar insufficient loss of PV within the VSLs has been previously observed by Cessi et al. (1987), Lozier and Riser (1989), Kiss (2002) and Nakano et al. (2008). This phenomenon has also been found to drive the recirculation zones (Cessi et al., 1987; Nakano et al., 2008), but its link with inter-gyre PV exchange has not been made before. We also checked that although the geometric wind effect would also correspond to a reduction in viscous boundary fluxes, the effect was far too weak. Furthermore, the interior lobe was found to be due to the formation of Fofonoff-type gyres. This indicates that the nonlinear mechanisms involved within each of these lobes are likely distinct.

We performed a Lagrangian particle analysis to confirm the link between the VSLs of the WBCs and the inter-gyre PV exchange mechanism. Studies of inter-gyre transport through jet instabilities, ring formations and large-scale changes in wind-forcing, etc. have been looked at before (e.g. Yang, 1996; Coulliette and Wiggins, 2001; Berloff et al., 2002, 2007b), but the potential control through of the inter-gyre transport by the VSL is again, to our knowledge, a new revelation. Confirmation of the inter-gyre PV exchange mechanism through a Lagrangian particle analysis allowed for the PV imbalance to be rectified. These migrating particles were also found to congregate in regions far from the interior lobe of the CGAs, and hence, unlikely to contribute to their formation. The loss of 'memory' property of material properties in the mid-ocean (see Rhines and Schopp, 1991) also indicates that the 'reverse' to our hypothesis, i.e., inter-gyre PV exchange reducing viscous boundary fluxes, is unlikely to be the case from this Lagrangian perspective. Finally, particles that do not migrate between the gyres were found to enter their respective recirculation zones where they backscatter. This implies that nonlinear processes within the WBLs are vital in driving mechanisms that both support and weaken the eastward jet. Indeed, Berloff et al. (2007b) found that intrinsic, decadal modes of variability in the ocean gyres were attributed to competition between these exact two mechanisms.

Although we have revealed some interesting dynamics within this chapter, it is important to note that our model contains significant idealisations, which we must highlight. Firstly, the lack of continental slope and the idealised basin geometry leads to, at the very least, an oversimplification of the boundary-layer dynamics. Stern (1998), and more recently Schoonover et al. (2017), indicated that

continental slope acts as a source of cyclonic vorticity for subtropical WBCs which itself transports anti-cyclonic vorticity. This mechanism was also found by Schoonover et al. (2017) to be vital for boundary current separation. These studies suggest that continental slope is likely to even further inhibit viscous boundary fluxes along coastlines. Another idealisation is that coupling of the eastward jet extension and overlying atmosphere have been neglected (see Chapter 3).

As a concluding remark, it has become even more apparent to us throughout this chapter that correct modelling of physical processes within the WBL are vital to not only understand the local physics, but the global circulation itself. We emphasise that realistic simulations of the ocean gyres may only be possible through accurate representations of the nonlinear processes within the WBCs. This may require grid resolutions even higher than simply resolving the mesoscales to fully capture the dynamics occurring in these regions.

Parts of this chapter have been taken from Kurashina et al. (2021), all of which is original work that has been conducted by the author.

Chapter 6

Conclusions

This thesis investigated the anatomy and mechanisms of low-frequency variability in the ocean gyres and jet stream using idealised, eddy-resolving models of the midlatitude climate. We believe such models offer a unique perspective into the topic due to their rich dynamical behaviours and transparency under analysis, which allow for in-depth explorations of the underlying physical processes.

However, before moving onto the main findings of this thesis, it is important to note certain idealisations in these models which should be noted to understand their relevance in nature. Firstly, the modelled SST fronts in Chapters 3 and 4 are too sharp and may be overestimating ocean SST-induced feed backs. The simple formulation of convection in the model, which is highly active in the midlatitudes over the WBCs, may also be leading to adverse effects in the modelled circulation. Furthermore, the lack of meridional overturning circulation, which is an important feature of the North Atlantic ocean circulation, is not modelled in Q-GCM or CABARET. Idealised geometries in the model may also lead to the strengthening or weakening of certain modes of variability which may not necessarily be occuring in nature.

Despite these idealised aspects of the modelled climate, we believe the benefits of using such models far outweigh the risks, as long as the limitations of such models are known. Both Q-GCM and CABARET still remain highly relevant in studying interactions of the ocean gyre circulation with important climate oscillations such as the North Atlantic Oscillation (NAO) and Pacific North American Pattern (PNA).

Our analysis began in Chapter 3 which looked at decomposing the coupled variability in the modelled climate. It was revealed that there is a positive feedback between meridional shifts of the eastward jet extension and downstream anchoring of the atmospheric westerly jet. Both the ocean and atmosphere responses found in the aforementioned coupled feedback is strongly controlled by eddy dynamics and the low-frequency variability was found to increase when coupling in the model is active. In the ocean, mesoscale turbulence likely reduces predictability of the ocean gyre response, while in the atmosphere, eddies were responsible for maintaining the line source of vorticity that anchored the atmospheric jet downstream. In order to better discern the role of eddies in the atmospheric response, a supplementary modelled climate with reduced atmospheric resolution was computed. It was found that reducing the atmospheric resolution, which consequently damps atmospheric eddies, led to a reduction in this downstream deflection of the westerly jet. This is because as the atmospheric resolution is decreased, the eddies cannot resolve the relatively small meridional shifts in the SST front and associated shifts in the centre of low-level baroclinicity.

In a continuation of analysis in the previous chapter, Chapter 4 looked at better understanding the ocean gyre response to wind-stress anomalies involved in the identified positive feedback mechanism. More in-depth investigation of the ocean gyre response was necessary due to the complex structure of the responsible wind-stress mode which generated an east-west dipole vorticity flux. Furthermore, two found ocean gyre responses to the same mode of forcing were statistically independent, indicating that the responses are governed by distinct processes and mechanisms. A series of double gyre circulations under different, fixed wind-stress forcings were computed and the time-averaged response of the ocean gyres was evaluated. We found that reducing the eastern basin wind-stress curl also reduced the magnitude of the meridional shift of the eastward jet extension, while the jet-axis tilt and recirculation zone strengths were preserved. This implied that western basin wind-stress curls control inertial recirculation zone strength while eastern basin wind-stress curls control meridional shifts of the eastward jet extension. The western basin ocean gyre response is consistent with a non-linear adjustment of the ocean gyres (Dewar, 2003); while the eastern basin ocean gyre response is more consistent with a baroclinic Rossby wave adjustment. The existence of Rossby wave formation, their westward propagation from the eastern boundary, and our demonstration that these two separate responses may be controlled independently supports this hypothesis. It is thus concluded that the

ocean gyre response is likely spatially inhomogeneous, i.e. the response of the gyres is dependent on the location of the applied wind-stress forcing.

Finally, Chapter 5 investigated the role of nonlinear dynamics in WBCs that maintain the ocean gyre circulation. In particular, we focused on the role of insufficient viscous PV fluxes at western boundaries and how they impact on downstream processes in the inertial recirculations and eastward jet. This chapter differs from Chapters 3, 4 as it does not look at adjustment of the ocean gyre circulation to wind-stress anomalies, but rather, the adjustment due to nonlinear dynamics in the VSL of WBCs. Two main effects on the ocean gyre circulation were found. The first was in supporting the downstream inertial recirculation zones which act to strengthen the eastward jet through eddy backscatter; the second was in the necessary inducing of inter-gyre PV exchange to conserve PV. Through a Lagrangian particle analysis, inter-gyre pathways were identified and shown to be dependent on which gyre the fluid parcels migrate from. In addition, a measurable PV advection was found to be taking place between the VSLs and corresponding opposite gyres. Causality of the WBL control on downstream processes was established through an additional 'switching on' experiment where nonlinear dynamics are turned on and transition between the linear- and nonlinear-dynamics solutions is checked. The time-scale of the transition was rapid and consistent with intense restructuring of the WBL due to nonlinear dynamics in the region, rather than decreases in concentration of PV in the gyres which would have a much slower, expected time-scale response. Furthermore, the fast 'loss of memory' of fluid parcels after migrating gyres makes it unlikely that advective processes that occur in this region are able to contribute to reductions in viscous boundary fluxes.

Although the approaches to Chapters 3, 4 and Chapter 5 were rather different, i.e. the former looked at anomalous circulation based upon a benchmark circulation while the latter looked at anomalous circulation based upon a linear, Sverdrup-like circulation, their overlapping findings are consistent with each other. For example, it has been shown in both sets of approaches that advective processes in the eastern basin are unlikely to lead to large-scale changes in the ocean gyre circulation. In fact, PV may only leave this region through the westward propagation of Rossby waves and the rest is mixed and stirred up by small-scale advective processes in the region. We also found that although the nonlinear restructuring of the WBL is intense, the resultant WBL appears rather stable under different wind-stress anomalies and only local restructuring near the jet separation regions was found.

In summary, we believe the quasigeostrophic double gyre circulation is maintained by nonlinear dynamics that occurs in the VSL of WBCs which may be modified by wind-induced vorticity fluxes due to the atmospheric variability or geometric wind effect. This is then able to adjust the double gyre circulation through changes in strength and position of the eastward jet through advective processes in the inertial recirculations or the propagation of jet-trapped Rossby waves.

Potential future work includes checking the effect of damping ocean eddies on the climate variability. For example, if the ocean resolution is dropped to, say, 20 km, is the positive feedback mechanism in Chapter 3 damped? If this is the case, then eddy-resolving resolutions in the ocean *and* atmosphere are required for this positive feedback to be significant in the coupled model. Another avenue of research is understanding the trigger for regime shifts in the coupled model. Positive feedbacks alone are not enough to generate sustained oscillations in the model and something must lead to negative feedbacks that either cause the atmospheric jet or ocean eastward jet to switch between poleward and equatorward states. Indeed, the ocean eastward jet in its poleward state led to increased surface heat flux over the subtropical WBC which may drain heat from the ocean mixed layer if it is not recovered by diabatic heating. Since the positive feedbacks require heat from the ocean mixed layer to sustain it, this may limit the time-scale of the positive feedback and could lead to the ocean to revert to its mean state to restore heat. Indeed, as surface heat fluxes over the subtropical WBC decrease for the ocean jet in its equatorward state, this may encourage the jet to switch states and lead to the generation of sustained climate oscillations.

Appendix A

A.1 Reduced atmospheric resolution parameters

Parameter	Value	Description
${}^aX \times {}^aY$	30 720 km × 7680 km	Domain size
$\Delta^a x$	80 km*	Horizontal grid spacing
$\Delta^a t$	90 s*	Time step
${}^aH_k$	(2000, 3000, 4000) m	Layer thickness
${}^aH_m$	1000 m	Mean BL thickness
${}^a\rho$	1 $\mathrm{kg\,m^{-3}}$	Density
${}^aC_p$	1000 $\mathrm{J\,kg^{-1}\,K^{-1}}$	Specific heat capacity
${}^ag'_k$	(1.2, 0.4) $\mathrm{m\,s^{-2}}$	Reduced gravity
${}^aA_4$	1.0×10^{14} $\mathrm{m^4\ s^{-1}}$*	Biharmonic viscosity coeff.
${}^a\alpha_{bc}$	1	Partial-slip BC coeff.
${}^aK_2$	2.5×10^4 $\mathrm{m^2\,s^{-1}}$*	Laplacian diffusion coeff.
${}^aK_4$	2.0×10^{14} $\mathrm{m^4\,s^{-1}}$*	Biharmonic diffusion coeff.
K_η	2.0×10^5 $\mathrm{m^2\ s^{-1}}$*	Diffusion coeff. for ${}^a\eta_m$
${}^ar_{dk}$	(496, 259) km	Baroclinic Rossby radii

Table A.1: Parameters for the channel atmosphere model in the reduced atmospheric resolution (80 km) modelled climate. Parameters that are different from the benchmark atmospheric model (Table 2.2) have an asterisk * added next to the value.

A.2 Overactive convection in the subpolar gyre

Fig. A.1 shows the effect of overactive convection on the time-averaged, upper ocean total entrainment. Extremely large values of entrainments due to persistent convection events were found near the subpolar WBC separation region where extreme lows in SSTs develop. Convection events are not

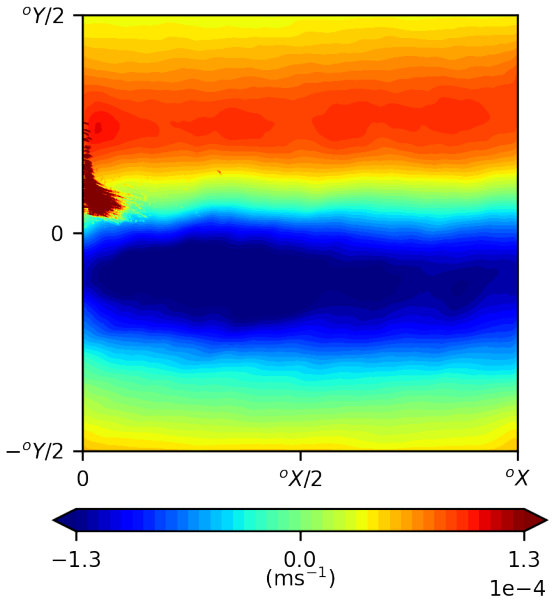

Figure A.1: Overactive convection in the subpolar WBC. Time-averaged upper-ocean total entrainment e_{total} with contour plots saturated by a factor of 65. Data was averaged over a 40-yr period for a system in statistical equilibrium

necessarily a problem in this model if similar values were found in the coupled configuration of this model. However, we found zero events of ocean convection in KB22, leading us to conclude that such values of entrainment are aphysical. Such large forcings of diabatic entrainment near the eastward jet separation region led to weakening of the ocean gyre circulation. Such double gyre circulations were akin to those computed by Hogg et al. (2009) where strong Ekman pumping anomalies near the jet separation region destabilised the jet.

The colours in Fig. A.1 have been saturated by a factor of 65 to make the forcing over the remainder of the gyres visible. The fact that entrainments over the remainder of the gyres are at normal levels indicates that thermal forcing over the subpolar WBC is likely the cause of the issue. Thermal forcing for an ocean-only configuration of Q-GCM is taken from the time-averaged ocean diabatic heating obtained from a fully coupled model run. In our case, the time-averaged diabatic heating from KB22 was used. If the position of the WBCs misaligns with the thermal forcing, which only occupies a small region over the basin (see Fig. 4.2d), then extreme values of surface temperature may develop due to the lack of thermal regulation by the ocean diabatic heating. In the subtropical gyre, surface temperatures are also regulated by a fixed temperature Dirichlet boundary condition. However, the subpolar gyre has no such temperature regulation along the northern boundary. In order to remove

the effects of convection, temperature is capped below at the fixed temperature of the upper-isopycnal layer T_1 but we choose to not model the adjustment in entrainment which accompanies this. For example, whenever T_m falls below T_1, i.e. the ocean is unstably stratified, there is usually an adjustment of the ocean diabatic entrainment term by adding on

$$\delta e_1 = -\frac{H_m(T_1 - T_m)}{2\Delta t \Delta_1 T} \tag{A.1}$$

where Δt is the ocean time-step and $\Delta_1 T = T_1 - T_2$. At the end of the convection step, T_m is set to T_1. In our case, we have removed this entrainment 'correction' term and simply only implemented the temperature capping at the end of the step. This essentially means we have applied an artificial thermal forcing over regions where overly extreme values of low temperatures may develop. Importantly, the model still conserves PV which is important since our analysis relies on this for accurate PV budgets. We recommend a more robust diabatic forcing implementation in this particular model configuration which allows for time-varying sensible and latent heat fluxes against prescribed atmospheric surface temperatures.

A.3 CABARET model

The model used in Chapter 5 is called the CABARET model which is described and implemented in Karabasov et al. (2009)[1]. This model is preferred to Q-GCM for the purposes of this chapter because it allows for more accurate modelling of PV advection in the ocean gyres due to its superior advection scheme. Although the model still mimics the wind-driven, midlatitude ocean circulation, it also differs from the ones used in the previous chapters as it is adiabatic, i.e. only driven by Ekman pumping. Since quasigeostrophic double gyre models have already been introduced in Chapter 2, we keep the description of the model brief and forward the reader to Karabasov et al. (2009) and Berloff (2015) for full details. Key parameters are listed in Table A.2. Note the parameter choices are very similar to those in Table 2.1.

[1]Description of this model was left out in Chapter 2 to

Table A.2: CABARET parameters for the benchmark double gyre ocean model

Parameter	Value	Description
$2L \times 2L$	$3840\,\text{km} \times 3840\,\text{km}$	Domain size
f_0	$0.83 \times 10^{-4}\,\text{s}^{-1}$	Coriolis parameter
γ	$4 \times 10^{-8}\,\text{s}^{-1}$	Bottom friction spin-down parameter
β	$2 \times 10^{-11}\text{m}^{-1}\text{s}^{-1}$	Planetary vorticity gradient
Δx	7.5 km	Horizontal grid spacing
Δt	Varies with CFL condition	Time step
H_k	$(250, 750, 3000)\,\text{m}$	Layer thickness
ρ_1	$1000\,\text{kg}\,\text{m}^{-3}$	Layer-1 Density
ν	$(20, 20, 20)\,\text{m}^2\,\text{s}^{-1}$	Laplacian viscosity coefficient
α	120 km	Partial-slip BC coefficient
r_{dk}	$(40.0, 20.6)\,\text{km}$	Baroclinic Rossby deformation radii

A.3.1 Model geometry

The model consists of a square box ocean with lateral dimensions $2L \times 2L$ and a depth of 4 km. There are three vertically stacked isopycnal layers with depths $(250, 750, 3000)$ m.

A.3.2 The QG equations

The governing QG equations are given in terms of the streamfunction ψ_i and PV anomalies q_i which are defined by

$$q_1 = \nabla^2\psi_1 - \frac{f_0^2}{g_1' H_1}(\psi_1 - \psi_2) \tag{A.2}$$

$$q_2 = \nabla^2\psi_2 - \frac{f_0^2}{g_1' H_2}(\psi_2 - \psi_1) - \frac{f_0^2}{g_2' H_2}(\psi_2 - \psi_3) \tag{A.3}$$

$$q_3 = \nabla^2\psi_3 - \frac{f_0^2}{g_2' H_3}(\psi_3 - \psi_2)\,. \tag{A.4}$$

where the reduced gravities g_1', g_2' are defined by the first and second baroclinic Rossby deformation radii, chosen to be 40.0 km and 20.6 km, respectively.

The QG equations, similar to Section 2.1, may now be written as

$$\frac{\partial q_1}{\partial t} + J(\psi_1, q_1) + \beta \frac{\partial \psi_1}{\partial x} = \frac{1}{\rho_1 H_1} W + \nu \nabla^4 \psi_1 \,, \tag{A.5}$$

$$\frac{\partial q_2}{\partial t} + J(\psi_2, q_2) + \beta \frac{\partial \psi_2}{\partial x} = \nu \nabla^4 \psi_2 \,, \tag{A.6}$$

$$\frac{\partial q_3}{\partial t} + J(\psi_3, q_3) + \beta \frac{\partial \psi_3}{\partial x} = -\gamma \nabla^2 \psi_3 + \nu \nabla^4 \psi_3 \,, \tag{A.7}$$

where $\psi = p/f_0$ is the velocity streamfunction or dynamic pressure scaled by the Coriolis parameter.

The asymmetric wind-forcing is fixed in time and defined as

$$W(x,y) = \begin{cases} -\frac{\pi \tau_0 A}{2L} \sin\left[\frac{\pi(L+y)}{L+Bx}\right], & \text{if } y \leq Bx, \\ +\frac{\pi \tau_0}{2LA} \sin\left[\frac{\pi(y-Bx)}{L-Bx}\right], & \text{if } y > Bx. \end{cases} \tag{A.8}$$

where $A = 0.9, B = 0.2$ and $\tau_0 = 0.08\,\mathrm{Nm}^{-2}$. The extra factor of $1/2$ in (A.8) and an order of magnitude correction in τ are both rectifications of typos in Berloff (2015). Note that A and B are parameters that control the degree of asymmetry in the wind-forcing.

Partial-slip boundary conditions $\psi_{nn} = \alpha \psi_n$, where n is the normal-to-wall unit vector, are enforced on the lateral boundaries (Haidvogel et al., 1992). Note the partial-slip boundary condition parameter is both dimensional and inverted compared to Section 2.1 but its essential implementation is the same. Mass conservation constraints are applied for each layer (McWilliams, 1977). The partial-slip boundary condition parameter $\alpha = 120\,\mathrm{km}$ is chosen such that it is close to a free-slip boundary condition but still allows for momentum flux through the lateral boundaries (Deremble et al., 2011). The equations are solved using the CABARET scheme (Karabasov et al., 2009) with a nominal resolution of $7.5\,\mathrm{km}$, corresponding to a uniform 513^2 grid.

A.3.3 Linearised dynamics

As we are interested in studying advection-induced anomalies, we also require solutions for the linearised dynamics. System (A.7) is linearised around the state of rest to give

$$\frac{\partial q_1}{\partial t} + \beta \frac{\partial \psi_1}{\partial x} = \frac{1}{\rho_1 H_1} W + \nu \nabla^4 \psi_1 \,, \tag{A.9}$$

$$\frac{\partial q_2}{\partial t} + \beta \frac{\partial \psi_2}{\partial x} = \nu \nabla^4 \psi_2 \,, \tag{A.10}$$

$$\frac{\partial q_3}{\partial t} + \beta \frac{\partial \psi_3}{\partial x} = -\gamma \nabla^2 \psi_3 + \nu \nabla^4 \psi_3 \,. \tag{A.11}$$

The parameters for these equations as well as the configuration of the numerical CABARET solver are identical to system (A.7).

A.4 Cope repository

The GitHub repository for all relevant code used in this thesis may be accessed on:

`https://github.com/rkurashina/oceans-imperial`

Bibliography

Alexander, M. et al. (2010). Extratropical air–sea interaction, sea surface temperature variability, and the pacific decadal oscillation. *Climate dynamics: why does climate vary*, 123:148.

Baker, L. H., Shaffrey, L. C., Sutton, R. T., Weisheimer, A., and Scaife, A. A. (2018). An Intercomparison of Skill and Overconfidence/Underconfidence of the Wintertime North Atlantic Oscillation in Multimodel Seasonal Forecasts. *Geophysical Research Letters*, 45(15):7808–7817.

Barnes, E. and Polvani, L. (2013). Response of the Midlatitude Jets, and of Their Variability, to Increased Greenhouse Gases in the CMIP5 Models. *Journal of Climate*, 26(18):7117–7135.

Barsugli, J. and Battisti, D. (1998). The Basic Effects of Atmosphere–Ocean Thermal Coupling on Midlatitude Variability*. *Journal of the Atmospheric Sciences*, 55(4):477–493.

Battisti, D., Bhatt, U., and Alexander, M. (1995). A modelling study of the interannual variability in the wintertime North Atlantic ocean. *Journal of Climate*, 8(12):3067–3083.

Berloff, P. (2005). On dynamically consistent eddy fluxes. *Dynamics of Atmospheres and Oceans*, 38(3-4):123–146.

Berloff, P. (2015). Dynamically consistent parameterization of mesoscale eddies. Part I: simple model. *Ocean Modelling*, 85:1–19.

Berloff, P. (2016). Dynamically consistent parameterization of mesoscale eddies. Part II: eddy fluxes and diffusivity from transient impulses. *Fluids*, 22(1).

Berloff, P., Dewar, W., Kravtsov, S., and McWilliams, J. (2007a). Ocean eddy dynamics in a coupled ocean–atmosphere model. *Journal of Physical Oceanography*, 37(5):1103–1121.

Berloff, P., Hogg, A., and Dewar, W. (2007b). The turbulent oscillator: a mechanism of low-frequency variability of the wind-driven ocean gyres. *Journal of Physical Oceanography*, 37(9):2363–2386.

Berloff, P. and McWilliams, J. (1999a). Large-scale, low-frequency variability in wind-driven ocean gyres. *Journal of Physical Oceanography*, 29:1925–1948.

Berloff, P. and McWilliams, J. (1999b). Quasigeostrophic dynamics of the western boundary current. *Journal of Physical Oceanography*, 29:2607–2634.

Berloff, P., McWilliams, J., and Bracco, A. (2002). Material transport in oceanic gyres. Part I: phenomenology. *Journal of Physical Oceanography*, 32:764–796.

Bjerknes, J. (1964). Atlantic Air-Sea Interaction. *Advances in Geophysics*, 10:1–82.

Brayshaw, D., Hoskins, B., and Blackburn, M. (2008). The Storm-Track Response to Idealized SST Perturbations in an Aquaplanet GCM. *Journal of the Atmospheric Sciences*, 65(9):2842–2860.

Bretherton, C., Smith, C., and Wallace, J. (1992). An Intercomparison of Methods for Finding Coupled Patterns in Climate Data. *Journal of Climate*, 5(6):541–560.

Ceppi, P., Zappa, G., Shepherd, T., and Gregory, J. (2018). Fast and Slow Components of the Extratropical Atmospheric Circulation Response to CO2 Forcing. *Journal of Climate*, 31(3):1091–1105.

Cessi, P., Ierley, G., and Young, W. (1987). A model of the inertial recirculation driven by potential vorticity anomalies. *Journal of Physical Oceanography*, 17:1640–1652.

Collins, M., Knutti, R., Arblaster, J., Dufresne, J.-L., Fichefet, T., Friedlingstein, P., Gao, X., Gutowski, W. J., Johns, T., Krinner, G., et al. (2013). Long-term climate change: projections, commitments and irreversibility. In *Climate change 2013-The physical science basis: Contribution of working group I to the fifth assessment report of the intergovernmental panel on climate change*, pages 1029—-1136. Cambridge University Press.

Coulliette, C. and Wiggins, S. (2001). Intergyre transport in a wind-driven, quasigeostrophic double gyre: An application of lobe dynamics. *European Geosciences Union (EGU)*, 8(1):69–94.

Czaja, A., Frankignoul, C., Minobe, S., and Vannière, B. (2019). Simulating the Midlatitude Atmospheric Circulation: What Might We Gain From High-Resolution Modeling of Air-Sea Interactions? *Current Climate Change Reports*, 5:390–406.

Czaja, A. and Marshall, J. (2001). Observations of atmosphere-ocean coupling in the North Atlantic. *Quarterly Journal of the Royal Meteorological Society*, 127:1893–1916.

Deremble, B., Hogg, A., Berloff, P., and Dewar, W. (2011). On the application of no-slip lateral boundary conditions to 'coarsely' resolved ocean models. *Ocean Modelling*, 39(3-4):411–415.

Dewar, W. (2001). On ocean dynamics in midlatitude climate. *Journal of Climate*, 14(23):4380–4397.

Dewar, W. (2003). Noninear Midlatitude Ocean Adjustment. *Journal of Physical Oceanography*, 33(5):1057–1082.

Dewar, W. and Morris, M. (2000). On the Propagation of Baroclinic Waves in the General Circulation. *Journal of Physical Oceanography*, 30(11):2637–2649.

Dunstone, N., Smith, D., Scaife, A., Hermanson, L., Eade, R., Robinson, N., Andrews, M., and Knight, J. (2016). Skilful predictions of the winter North Atlantic Oscillation one year ahead. *Nature Geoscience 2016 9:11*, 9(11):809–814.

Eyring, V., Bony, S., Meehl, G. A., Senior, C. A., Stevens, B., Stouffer, R. J., and Taylor, K. E. (2016). Overview of the Coupled Model Intercomparison Project Phase 6 (CMIP6) experimental design and organization. *Geoscientific Model Development*, 9(5):1937–1958.

Famooss Paolini, L., Athanasiadis, P., Ruggieri, P., and Bellucci, A. (2022). The atmospheric response to meridional shifts of the Gulf Stream SST front and its dependence on model resolution. *Journal of Climate*, pages 1–57.

Farneti, R. (2007). Coupled interannual Rossby waves in a quasigeostrophic ocean-atmosphere model. *Journal of Physical Oceanography*, 37:1192–1214.

Feliks, Y., Ghil, M., and Simonnet, E. (2004). Low-Frequency Variability in the Midlatitude Atmosphere Induced by an Oceanic Thermal Front. *Journal of the Atmospheric Sciences*, 61(9):961–981.

Fofonoff, N. (1954). Steady flow in a frictionless homogeneous ocean. *Journal of Marine Research*, 13(3):254–262.

Foussard, A., Lapeyre, G., and Plougonven, R. (2019). Storm track response to oceanic eddies in idealized atmospheric simulations. *Journal of Climate*, 32(2):445–463.

Frankignoul, C. and Hasselmann, K. (1977). Stochastic climate models. Part II: application to sea-surface temperature anomalies and thermocline variability. *Tellus*, 29(4):289–305.

Frankignoul, C., Sennéchael, N., Kwon, Y.-O., and Alexander, M. (2011). Influence of the Meridional Shifts of the Kuroshio and the Oyashio Extensions on the Atmospheric Circulation. *Journal of Climate*, 24(3):762–777.

Goodman, J. and Marshall, J. (1999). A model of decadal middle-latitude atmosphere-ocean coupled modes. *Journal of Climate*, 12(2):621–641.

Haidvogel, D., McWilliams, J., and Gent, P. (1992). Boundary current separation in a quasi-geostrophic, eddy-resolving ocean circulation model. *Journal of Physical Oceanography*, 22:882–902.

Harrison, D. and Stalos, S. (1982). On the wind-driven ocean circulation. *Journal of Marine Research*, 40(3):773–791.

Hasselmann, K. (1976). Stochastic climate models. Part I: theory. *Tellus*, 28(6):473–485.

He, J., Kirtman, B., Soden, B., Vecchi, G., Zhang, H., and Winton, M. (2018). Impact of Ocean Eddy Resolution on the Sensitivity of Precipitation to CO2 Increase. *Geophysical Research Letters*, 45(14):7194–7203.

Held, I. and Hoskins, B. (1985). Large-Scale Eddies and the General Circulation of the Troposphere. *Advances in Geophysics*, 28A:3–31.

Hogg, A., Blundell, J., Dewar, W., and Killworth, P. (2014). Formulation and users' guide for Q-GCM. Version 1.5.0. Technical report, Southampton Oceanography Centre.

Hogg, A., Dewar, W., Berloff, P., Kravtsov, S., and Hutchinson, D. (2009). The effects of mesoscale ocean-atmosphere coupling on the large-scale ocean circulation. *Journal of Climate*, 22(15):4066–4082.

Hogg, A., Dewar, W., Killworth, P., and Blundell, J. (2003). A quasi-geostrophic coupled model (Q-GCM). *Monthly Weather Review*, 131(10):2261–2278.

Hogg, A., Dewar, W., Killworth, P., and Blundell, J. (2006). Decadal variability of the midlatitude climate system driven by the ocean circulation. *Journal of Climate*, 19:1149–1166.

Hogg, A., Killworth, P., Blundell, J., and Dewar, W. (2005). Mechanisms of decadal variability of the wind-driven ocean circulation. *Journal of Physical Oceanography*, 35(4):512–531.

Holland, W. (1978). The role of mesoscale eddies in the general circulation of the ocean - numerical experiments using a wind-driven quasi-geostrophic model. *American Meteorological Society*, 8:363–392.

Holland, W. and Rhines, P. (1980). An example of eddy-induced ocean circulation. *Journal of Physical Oceanography*, 10(7):1010–1031.

Hoskins, B. and Karoly, D. (1981). The steady linear response of a spherical atmosphere to thermal and orographic forcing. *Journal of the Atmospheric Sciences*, 38(6):1179–1196.

Hoskins, B. and Valdes, P. (1990). On the existence of storm-tracks. *Journal of the Atmospheric Sciences*, 47(15):1854–1864.

Infanti, J. and Kirtman, B. (2019). A comparison of CCSM4 high-resolution and low-resolution predictions for south Florida and southeast United States drought. *Climate Dynamics*, 52(11):6877–6892.

Jin, F.-F. (1997). A theory of interdecadal climate variability of the North Pacific ocean-atmosphere system*. *Journal of Climate*, 10(8):1821–1835.

Jung, T., Miller, M. J., Palmer, T. N., Towers, P., Wedi, N., Achuthavarier, D., Adams, J. M., Altshuler, E. L., Cash, B. A., Kinter, J. L., Marx, L., Stan, C., and Hodges, K. I. (2012). High-Resolution

Global Climate Simulations with the ECMWF Model in Project Athena: Experimental Design, Model Climate, and Seasonal Forecast Skill. *Journal of Climate*, 25(9):3155–3172.

Karabasov, S., Berloff, P., and Goloviznin, V. (2009). CABARET in the ocean gyres. *Ocean Modelling*, 30(2-3):155–168.

Kim, W., Yeager, S., Chang, P., and Danabasoglu, G. (2018). Low-Frequency North Atlantic Climate Variability in the Community Earth System Model Large Ensemble. *Journal of Climate*, 31(2):787–813.

Kirtman, B., Bitz, C., Bryan, F., Collins, W., Dennis, J., Hearn, N., Kinter, J., Loft, R., Rousset, C., Siqueira, L., Stan, C., Tomas, R., and Vertenstein, M. (2012). Impact of ocean model resolution on CCSM climate simulations. *Climate Dynamics*, 39(6):1303–1328.

Kirtman, B., Perlin, N., and Siqueira, L. (2017). Ocean eddies and climate predictability. *Chaos: An Interdisciplinary Journal of Nonlinear Science*, 126902:17.

Kiss, A. (2002). Potential vorticity "crises", adverse pressure gradients, and western boundary current separation. *Journal of Marine Research*, 60(6):779–803.

Kiss, A. (2010). Dynamics of separating western boundary currents in ocean models. *IOP Conference Series: Earth and Environmental Science*, 11(1):012034.

Klaver, R., Haarsma, R., Vidale, P. L., and Hazeleger, W. (2020). Effective resolution in high resolution global atmospheric models for climate studies. *Atmospheric Science Letters*, 21(4):e952.

Kravtsov, S., Berloff, P., Dewar, W., Ghil, M., and McWilliams, J. (2006). Dynamical Origin of Low-Frequency Variability in a Highly Nonlinear Midlatitude Coupled Model. *Journal of Climate*, 19(24):6391–6408.

Kravtsov, S., Dewar, W., Berloff, P., McWilliams, J., and Ghil, M. (2007). A highly nonlinear coupled mode of decadal variability in a mid-latitude ocean-atmosphere model. *Dynamics of Atmospheres and Oceans*, 43(3-4):123–150.

Kravtsov, S. and Robertson, A. (2002). Midlatitude ocean-atmosphere interaction in an idealized coupled model. *Climate Dynamics*, 19:693–711.

Kravtsov, S., Robertson, A., and Ghil, M. (2003). Low-frequency variability in a baroclinic beta-channel with land-sea contrast*. *Journal of Atmospheric Sciences*, 60(18):2267–2293.

Kurashina, R. and Berloff, P. (2022a). Low-frequency variability enhancement of the midlatitude climate in an eddy-resolving, coupled ocean-atmosphere model. Part I : Anatomy. *preprint, Climate Dynamics*.

Kurashina, R. and Berloff, P. (2022b). Low-frequency variability enhancement of the midlatitude climate in an eddy-resolving, coupled ocean-atmosphere model. Part II: Mechanisms. *preprint, Climate Dynamics*.

Kurashina, R., Berloff, P., and Shevchenko, I. (2021). Western boundary layer nonlinear control of the oceanic gyres. *Journal of Fluid Mechanics*, 918(A43):26.

Kushnir, Y., Robinson, W., Bladé, I., Hall, N., Peng, S., and Sutton, R. (2002). Atmospheric GCM response to extratropical SST anomalies: synthesis and evaluation. *Journal of Climate*, 15(16):2233–2256.

Kwon, Y.-O., Alexander, M., Bond, N., Frankignoul, C., Nakamura, H., Qiu, B., and Thompson, L. (2010). Role of the Gulf Stream and Kuroshio-Oyashio systems in large-scale atmosphere-ocean interaction: A review. *Journal of Climate*, 23(12):3249–3281.

Latif, M. and Barnett, T. (1994). Causes of decadal climate variability over the North Pacific and North America. *Science*, 266(5185):634–637.

Latif, M. and Barnett, T. (1996). Decadal climate variability over the North Pacific and North America: Dynamics and predictability. *Journal of Climate*, 9(10):2407–2423.

Lee, R. W., Woollings, T. J., Hoskins, B. J., Williams, K. D., O'Reilly, C. H., and Masato, G. (2018). Impact of Gulf Stream SST biases on the global atmospheric circulation. *Climate Dynamics*, 51(9-10):3369–3387.

Lozier, M. and Riser, S. (1989). Potential vorticity dynamics of boundary currents in a quasi-geostrophic ocean. *Journal of Physical Oceanography*, 19(9):1373–1396.

Ma, X., Chang, P., Saravanan, R., Montuoro, R., Hsieh, J. S., Wu, D., Lin, X., Wu, L., and Jing, Z. (2015). Distant Influence of Kuroshio Eddies on North Pacific Weather Patterns? *Scientific Reports 2015 5:1*, 5(1):1–7.

Ma, X., Jing, Z., Chang, P., Liu, X., Montuoro, R., Small, R., Bryan, F., Greatbatch, R., Brandt, P., Wu, D., Lin, X., and Wu, L. (2016). Western boundary currents regulated by interaction between ocean eddies and the atmosphere. *Nature*, 535(7613):533–537.

Ma, X., Nakamura, H., Montuoro, R., Wu, L., Wu, D., Chang, P., Saravanan, R., and Lin, X. (2017). Importance of resolving Kuroshio front and eddy influence in simulating the North Pacific storm track. *Journal of Climate*, 30(5):1861–1880.

Mantua, N., Hare, S., Zhang, Y., Wallace, J., and Francis, R. (1997). A Pacific Interdecadal Climate Oscillation with Impacts on Salmon Production. *Bulletin of the American Meteorological Society*, 78(6):1069–1079.

Marshall, J., Armour, K. C., Scott, J. R., Kostov, Y., Hausmann, U., Ferreira, D., Shepherd, T. G., and Bitz, C. M. (2014). The ocean's role in polar climate change: asymmetric Arctic and Antarctic responses to greenhouse gas and ozone forcing. *Philosophical Transactions of the Royal Society A: Mathematical, Physical and Engineering Sciences*, 372(2019):17.

McDougall, T. and Dewar, W. (1998). Vertical Mixing and Cabbeling in Layered Models. *Journal of Physical Oceanography*, 28(7):1458–1480.

McWilliams, J. (1977). A note on a consistent quasigeostrophic model in a multiply connected domain. *Dynamics of Atmospheres and Oceans*, 1(5):427–441.

McWilliams, J. (2008). The nature and consequences of oceanic eddies. In *Geophysical Monograph Series*, volume 177, pages 5–15. American Geophysical Union.

Moro, B. (1988). On the nonlinear Munk model. I. Steady flows. *Dynamics of Atmospheres and Oceans*, 12(3-4):259–287.

Nakamura, H., Sampe, T., Goto, A., Ohfuchi, W., and Xie, S.-P. (2008). On the importance of

midlatitude oceanic frontal zones for the mean state and dominant variability in the tropospheric circulation. *Geophysical Research Letters*, 35(15):L15709.

Nakamura, H., Sampe, T., Tanimoto, Y., and Shimpo, A. (2004). Observed Associations Among Storm Tracks, Jet Streams and Midlatitude Oceanic Fronts. *Geophysical Monograph Series*, 147:329–345.

Nakano, H., Tsujino, H., and Furue, R. (2008). The Kuroshio Current System as a jet and twin "relative" recirculation gyres embedded in the Sverdrup circulation. *Dynamics of Atmospheres and Oceans*, 45(3-4):135–164.

Nonaka, M., Sasai, Y., Sasaki, H., Taguchi, B., and Nakamura, H. (2016). How potentially predictable are midlatitude ocean currents? *Scientific Reports 2016 6:1*, 6(1):1–8.

Okumura, Y., Xie, S.-P., Numaguti, A., and Tanimoto, Y. (2001). Tropical Atlantic air-sea interaction and its influence on the NAO. *Geophysical Research Letters*, 28(8):1507–1510.

O'Reilly, C. and Czaja, A. (2015). The response of the Pacific storm track and atmospheric circulation to Kuroshio Extension variability. *Quarterly Journal of the Royal Meteorological Society*, 141:52–66.

O'Reilly, C., Minobe, S., Kuwano-Yoshida, A., and Woollings, T. (2017). The gulf stream influence on wintertime north atlantic jet variability. *Quarterly Journal of the Royal Meteorological Society*, 143(702):173–183.

Palin, E., Thornton, H., Mathison, C., McCarthy, R., Clark, R., and Dora, J. (2013). Future projections of temperature-related climate change impacts on the railway network of Great Britain. *Climatic Change*, 120(1-2):71–93.

Peng, S., Robinson, W., and Hoerling, M. (1997). The modeled atmospheric response to midlatitude SST anomalies and its dependence on background circulation states. *Journal of Climate*, 10(5):971–987.

Peng, S. and Whitaker, J. (1999). Mechanisms determining the atmospheric response to midlatitude SST anomalies. *Journal of Climate*, 12(5 II):1393–1408.

Piazza, M., Terray, L., Boé, J., Maisonnave, E., and Sanchez-Gomez, E. (2016). Influence of small-scale North Atlantic sea surface temperature patterns on the marine boundary layer and free troposphere: a study using the atmospheric ARPEGE model. *Climate Dynamics*, 46(5-6):1699–1717.

Renggli, D., Leckebusch, G., Ulbrich, U., Gleixner, S., and Faust, E. (2011). The Skill of Seasonal Ensemble Prediction Systems to Forecast Wintertime Windstorm Frequency over the North Atlantic and Europe. *Monthly Weather Review*, 139(9):3052–3068.

Révelard, A., Frankignoul, C., and Kwon, Y.-O. (2018). A Multivariate Estimate of the Cold Season Atmospheric Response to North Pacific SST Variability. *Journal of Climate*, 31(7):2771–2796.

Rhines, P. and Schopp, R. (1991). The Wind-driven Circulation: Quasi-geostrophic Simulations and Theory for Nonsymmetric Winds. *Journal of Physical Oceanography*, 21(9):1438–1469.

Rhines, P. and Young, W. (1982). Homogenization of potential vorticity in planetary gyres. *Journal of Fluid Mechanics*, 122:347–367.

Saba, V. S., Griffies, S. M., Anderson, W. G., Winton, M., Alexander, M. A., Delworth, T. L., Hare, J. A., Harrison, M. J., Rosati, A., Vecchi, G. A., and Zhang, R. (2016). Enhanced warming of the Northwest Atlantic Ocean under climate change. *Journal of Geophysical Research: Oceans*, 121(1):118–132.

Sampe, T., Nakamura, H., Goto, A., and Ohfuchi, W. (2010). Significance of a Midlatitude SST Frontal Zone in the Formation of a Storm Track and an Eddy-Driven Westerly Jet*. *Journal of Climate*, 23(7):1793–1814.

Saravanan, R. and McWilliams, J. (1997). Stochasticity and spatial resonance in interdecadal climate fluctuations. *Journal of Climate*, 10(9):2299–2320.

Sasaki, Y., Minobe, S., and Schneider, N. (2013). Decadal Response of the Kuroshio Extension Jet to Rossby Waves: Observation and Thin-Jet Theory*. *Journal of Physical Oceanography*, 43(2):442–456.

Sasaki, Y. and Schneider, N. (2011). Decadal Shifts of the Kuroshio Extension Jet: Application of Thin-Jet Theory*. *Journal of Physical Oceanography*, 41(5):979–993.

Scaife, A. A., Arribas, A., Blockley, E., Brookshaw, A., Clark, R. T., Dunstone, N., Eade, R., Fereday, D., Folland, C. K., Gordon, M., Hermanson, L., Knight, J. R., Lea, D. J., MacLachlan, C., Maidens, A., Martin, M., Peterson, A. K., Smith, D., Vellinga, M., Wallace, E., Waters, J., and Williams, A. (2014). Skillful long-range prediction of European and North American winters. *Geophysical Research Letters*, 41(7):2514–2519.

Scaife, A. A., Camp, J., Comer, R., Davis, P., Dunstone, N., Gordon, M., MacLachlan, C., Martin, N., Nie, Y., Ren, H. L., Roberts, M., Robinson, W., Smith, D., and Vidale, P. L. (2019). Does increased atmospheric resolution improve seasonal climate predictions? *Atmospheric Science Letters*, 20(8):e922.

Scaife, A. A. and Smith, D. (2018). A signal-to-noise paradox in climate science. *npj Climate and Atmospheric Science 2018 1:1*, 1(1):1–8.

Schiemann, R., Demory, M. E., Shaffrey, L. C., Strachana, J., Vidale, P. L., Mizielinski, M. S., Roberts, M. J., Matsueda, M., Wehner, M. F., Jung, T., and Jung, T. (2017). The Resolution Sensitivity of Northern Hemisphere Blocking in Four 25-km Atmospheric Global Circulation Models. *Journal of Climate*, 30(1):337–358.

Schneider, E. and Fan, M. (2012). Observed Decadal North Atlantic Tripole SST Variability. Part II: Diagnosis of Mechanisms. *Journal of the Atmospheric Sciences*, 69(1):51–64.

Schneider, N., Miller, A., and Pierce, D. (2002). Anatomy of North Pacific Decadal Variability. *Journal of Climate*, 15(6):586–605.

Schoonover, J., Dewar, W., Wienders, N., and Deremble, B. (2017). Local sensitivities of the Gulf Stream separation. *Journal of Physical Oceanography*, 47(2):353–373.

Seager, R., Kushnir, Y., Naik, N. H., Cane, M. A., and Miller, J. (2001). Wind-driven shifts in the latitude of the Kuroshio-Oyashio extension and generation of SST anomalies on decadal timescales. *Journal of Climate*, 14(22):4249–4265.

Seo, H., Kwon, Y.-O., Joyce, T., and Ummenhofer, C. (2017). On the Predominant Nonlinear Response of the Extratropical Atmosphere to Meridional Shifts of the Gulf Stream. *Journal of Climate*, 30(23):9679–9702.

Shaman, J., Samelson, R., and Skyllingstad, E. (2010). Air-sea fluxes over the gulf stream region: Atmospheric controls and trends. *Journal of Climate*, 23(10):2651–2670.

Shaw, T. A., Baldwin, M., Barnes, E. A., Caballero, R., Garfinkel, C. I., Hwang, Y. T., Li, C., O'Gorman, P. A., Rivière, G., Simpson, I. R., and Voigt, A. (2016). Storm track processes and the opposing influences of climate change. *Nature Geoscience 2016 9:9*, 9(9):656–664.

Sheldon, L., Czaja, A., Vanniere, B., Morcrette, C., Sohet, B., Casado, M., and Smith, D. (2017). A 'warm path' for Gulf Stream–troposphere interactions. *Tellus A: Dynamic Meteorology and Oceanography*, 69(1):1299397.

Shevchenko, I. and Berloff, P. (2016). Eddy backscatter and counter-rotating gyre anomalies of midlatitude ocean dynamics. *Fluids*, 28(1):16.

Shevchenko, I., Berloff, P., Guerrero-López, D., and Roman, J. (2016). On low-frequency variability of the midlatitude ocean gyres. *J. Fluid Mech*, 795:423–442.

Simpson, I. R., Deser, C., McKinnon, K. A., and Barnes, E. A. (2018). Modeled and Observed Multidecadal Variability in the North Atlantic Jet Stream and Its Connection to Sea Surface Temperatures. *Journal of Climate*, 31(20):8313–8338.

Siqueira, L. and Kirtman, B. P. (2016). Atlantic near-term climate variability and the role of a resolved Gulf Stream. *Geophysical Research Letters*, 43(8):3964–3972.

Skamarock, W. C. (2004). Evaluating Mesoscale NWP Models Using Kinetic Energy Spectra. *Monthly Weather Review*, 132(12):3019–3032.

Skamarock, W. C., Park, S. H., Klemp, J. B., and Snyder, C. (2014). Atmospheric Kinetic Energy Spectra from Global High-Resolution Nonhydrostatic Simulations. *Journal of the Atmospheric Sciences*, 71(11):4369–4381.

Small, R., Tomas, R., and Bryan, F. (2014). Storm track response to ocean fronts in a global high-resolution climate model. *Climate Dynamics*, 43:805–828.

Small, R. J., Msadek, R., Kwon, Y. O., Booth, J. F., and Zarzycki, C. (2019). Atmosphere surface storm track response to resolved ocean mesoscale in two sets of global climate model experiments. *Climate Dynamics*, 52(3-4):2067–2089.

Smirnov, D., Newman, M., and Alexander, M. (2014). Investigating the Role of Ocean–Atmosphere Coupling in the North Pacific Ocean. *Journal of Climate*, 27(2):592–606.

Smirnov, D., Newman, M., Alexander, M. A., Kwon, Y. O., and Frankignoul, C. (2015). Investigating the Local Atmospheric Response to a Realistic Shift in the Oyashio Sea Surface Temperature Front. *Journal of Climate*, 28(3):1126–1147.

Smith, D. M., Eade, R., Scaife, A. A., Caron, L. P., Danabasoglu, G., DelSole, T. M., Delworth, T., Doblas-Reyes, F. J., Dunstone, N. J., Hermanson, L., Kharin, V., Kimoto, M., Merryfield, W. J., Mochizuki, T., Müller, W. A., Pohlmann, H., Yeager, S., and Yang, X. (2019). Robust skill of decadal climate predictions. *npj Climate and Atmospheric Science 2019 2:1*, 2(1):1–10.

Smith, D. M., Scaife, A. A., Eade, R., Athanasiadis, P., Bellucci, A., Bethke, I., Bilbao, R., Borchert, L. F., Caron, L. P., Counillon, F., Danabasoglu, G., Delworth, T., Doblas-Reyes, F. J., Dunstone, N. J., Estella-Perez, V., Flavoni, S., Hermanson, L., Keenlyside, N., Kharin, V., Kimoto, M., Merryfield, W. J., Mignot, J., Mochizuki, T., Modali, K., Monerie, P. A., Müller, W. A., Nicolí, D., Ortega, P., Pankatz, K., Pohlmann, H., Robson, J., Ruggieri, P., Sospedra-Alfonso, R., Swingedouw, D., Wang, Y., Wild, S., Yeager, S., Yang, X., and Zhang, L. (2020). North Atlantic climate far more predictable than models imply. *Nature 2020 583:7818*, 583(7818):796–800.

Smith, R., Maltrud, M., Bryan, F., and Hecht, M. (2000). Numerical simulation of the North Atlantic Ocean at 1/10°. *Journal of Physical Oceanography*, 30:1532–1561.

Spall, M. (2014). Some influences of remote topography on western boundary currents. *Journal of Marine Research*, 72(2):73–94.

Stern, M. (1998). Separation of a density current from the bottom of a continental slope. *Journal of Physical Oceanography*, 28(10):2040–2049.

Strommen, K. and Palmer, T. N. (2019). Signal and noise in regime systems: A hypothesis on the

predictability of the North Atlantic Oscillation. *Quarterly Journal of the Royal Meteorological Society*, 145(718):147–163.

Taguchi, B., Nakamura, H., Nonaka, M., Komori, N., Kuwano-Yoshida, A., Takaya, K., and Goto, A. (2012). Seasonal Evolutions of Atmospheric Response to Decadal SST Anomalies in the North Pacific Subarctic Frontal Zone: Observations and a Coupled Model Simulation. *Journal of Climate*, 25(1):111–139.

Taguchi, B., Xie, S. P., Mitsudera, H., and Kubokawa, A. (2005). Response of the Kuroshio Extension to Rossby Waves Associated with the 1970s Climate Regime Shift in a High-Resolution Ocean Model. *Journal of Climate*, 18(15):2979–2995.

Taguchi, B., Xie, S.-P., Schneider, N., Nonaka, M., Sasaki, H., and Sasai, Y. (2007). Decadal variability of the Kuroshio Extension: Observations and an eddy-resolving model hindcast. *Journal of Climate*, 20(11):2357–2377.

Tanimoto, Y. (2003). An active role of extratropical sea surface temperature anomalies in determining anomalous turbulent heat flux. *Journal of Geophysical Research*, 108(C10):3304.

Tommasi, D., Stock, C. A., Hobday, A. J., Methot, R., Kaplan, I. C., Eveson, J. P., Holsman, K., Miller, T. J., Gaichas, S., Gehlen, M., Pershing, A., Vecchi, G. A., Msadek, R., Delworth, T., Eakin, C. M., Haltuch, M. A., Séférian, R., Spillman, C. M., Hartog, J. R., Siedlecki, S., Samhouri, J. F., Muhling, B., Asch, R. G., Pinsky, M. L., Saba, V. S., Kapnick, S. B., Gaitan, C. F., Rykaczewski, R. R., Alexander, M. A., Xue, Y., Pegion, K. V., Lynch, P., Payne, M. R., Kristiansen, T., Lehodey, P., and Werner, F. E. (2017). Managing living marine resources in a dynamic environment: The role of seasonal to decadal climate forecasts. *Progress in Oceanography*, 152:15–49.

Veronis, G. (1966a). Wind-driven ocean circulation-Part 1. Linear theory and perturbation analysis. *Deep-Sea Research*, 13:29.

Veronis, G. (1966b). Wind-driven ocean circulation-Part 2. Numerical solutions of the non-linear problem. *Deep-Sea Research and Oceanographic Abstracts*, 13(1):31–55.

von Storch, H. and Zwiers, F. (1999). *Statistical analysis in climate research*. Cambridge University Press, 1 edition.

Wills, R. C., Battisti, D. S., Proistosescu, C., Thompson, L. A., Hartmann, D. L., and Armour, K. C. (2019). Ocean circulation signatures of North Pacific decadal variability. *Geophysical Research Letters*, 46(3):1690–1701.

Woollings, T., Gregory, J. M., Pinto, J. G., Reyers, M., and Brayshaw, D. J. (2012). Response of the North Atlantic storm track to climate change shaped by ocean–atmosphere coupling. *Nature Geoscience 2012 5:5*, 5(5):313–317.

Wu, L., Cai, W., Zhang, L., Nakamura, H., Timmermann, A., Joyce, T., McPhaden, M. J., Alexander, M., Qiu, B., Visbeck, M., Chang, P., and Giese, B. (2012). Enhanced warming over the global subtropical western boundary currents. *Nature Climate Change 2012 2:3*, 2(3):161–166.

Yang, H. (1996). The subtropical/subpolar gyre exchange in the presence of annually migrating wind and a meandering jet: Water mass exchange. *Journal of Physical Oceanography*, 26(1):115–130.

Yang, H., Lohmann, G., Wei, W., Dima, M., Ionita, M., and Liu, J. (2016). Intensification and poleward shift of subtropical western boundary currents in a warming climate. *Journal of Geophysical Research: Oceans*, 121(7):4298–4945.

Yin, J. (2005). A consistent poleward shift of the storm tracks in simulations of 21st century climate. *Geophysical Research Letters*, 32(18):1–4.

Ypma, S., van Sebille, E., Kiss, A., and Spence, P. (2016). The separation of the East Australian Current: a Lagrangian approach to potential vorticity and upstream control. *Journal of Geophysical Research: Oceans*, 121(1):758–774.

Zhang, C., Liu, H., Xie, J., Lin, P., Li, C., Yang, Q., and Song, J. (2020). North Pacific storm track response to the mesoscale SST in a global high-resolution atmospheric model. *Climate Dynamics*, 55(5-6):1597–1611.

Zhang, W. and Kirtman, B. (2019). Understanding the Signal-to-Noise Paradox with a Simple Markov Model. *Geophysical Research Letters*, 46(22):13308–13317.

Zhang, W., Kirtman, B., Siqueira, L., Clement, A., and Xia, J. (2021). Understanding the signal-to-noise paradox in decadal climate predictability from CMIP5 and an eddying global coupled model. *Climate Dynamics*, 56(9):2895–2913.